IMPLEMENTATION AND PERFORMANCE ANALYSIS OF VARIOUS TECHNIQUES FOR SNOW COVER MONITORING IN WESTERN HIMALAYAS

A

THESIS SUBMITTED

FOR THE DEGREE OF

DOCTOR OF PHILOSOPHY

BY

JAGJIT KUMAR SHARMA

Regn. No. 90706501

Supervisor:
Dr Rajesh Khanna
Prof. & Head
Department of ECE
Thapar University
Patiala

Supervisor:
Dr V D Mishra
Scientist 'E'
Snow and Avalanche Study
Establishment (DRDO)
Chandigarh, UT

Electronics and Communication Engineering Department
Thapar University
Patiala(147004)
June-2013

CERTIFICATE

Certified that the work presented in this thesis entitled "**Implementation and Performance Analysis of Various Techniques for Snow Cover Monitoring in Western Himalayas**" is an account of own work carried out by Mr. Jagjit Kumar Sharma under our supervision from Jan, 2008.

The matter presented in this thesis does not incorporate without acknowledgement any material previously published or written by any other person except where due reference is made in the text.

Registration No: 90706501

Date: 21/6/13

Supervisor:
Dr Rajesh Khanna
Prof. & Head
Department of ECE
Thapar University, Patiala
Punjab

Supervisor:
Dr V D Mishra
Scientist 'E'
Snow and Avalanche Study
Establishment (DRDO)
Chandigarh (UT)

ACKNOWLEDGEMENTS

I would like to place on record my deep sense of gratitude to my supervisor Dr Rajesh Khanna, Professor and Head ECE Department, Thapar University Patiala for his valuable guidance and constant encouragement during the course of this study.

With a sense of deep regards and profound gratitude, I express my sincere thanks to my supervisor Dr V D Mishra, Scientist F, Snow and Avalanche Study Establishment (SASE) Chandigarh for his, constant guidance, motivation and encouragement, lengthy discussions and valuable suggestions throughout the complete course of this investigative study and preparation of thesis work.

I am thankful to Dr R N Sarwade, erstwhile Director Snow and Avalanche Study Establishment for permitting Dr V D Mishra to guide this study and allowing me to use the facilities of SASE Chandigarh. I am also thankful to Mr Ashvagosh Ganju, Director, Snow and Avalanche Study Establishment for allowing me to continue and complete my PhD Study. I am also thankful to Mr Gurvinder Singh Bahra, Chairman Rayat-Bahra Group to permit me to do this study work.

I would also like to express my sincere thanks to Mr Snehmani, Mr H S Negi, Mr N K Thakur, Mr Arun Chaudhry, Scientists Remote Sensing Group, SASE, for their valuable help in collection and compilation of image data from the SASE Archives as well as fruitful discussions and suggestions.

I am highly thankful to Prof A K Chatterji, Dr Kulbir Singh, and Dr Maneek Kumar from Thapar University for their critical evaluation and regular reviews during the course of this study.

No words are adequate and sufficient to express my heartfelt thanks to my wife Savita and my daughter Manisha as without their consistent moral support and encouragement; it would not have been possible to complete this work.

Chandigarh

17, June 2013

(JAGJIT KUMAR SHARMA)

CONTENTS

PREFACE

Himalayan region has very high concentration of mountain glaciers and it is completely covered by snowfall during winter period between November and April. Very few studies on monitoring of snow cover have been reported in this region. However, the demand for snow cover monitoring in this region has gained importance in order to find the solution to some of the related issues such as global warming, lack of water supply, electrification in rural areas and hazard forecasting etc. The availability of moderate resolution image data almost on day today basis from sensors such as MODIS and AWiFS has provided great opportunity for regular mapping and monitoring of snow in this region.

The present thesis entitled "Implementation and Performance Analysis of Various Techniques for Snow Cover Monitoring in Western Himalayas" deals with evaluating the performance of various topographic correction techniques on the snow spectral characteristics obtained from MODIS and AWiFS data and suggesting the most suitable technique for this region. It also deals with the monitoring of snow using per pixel and sub-pixel techniques and a new statistical linear regressive relationship has been developed between normalized difference snow index (NDSI) and fraction of snow covered image obtained by Linear Mixture Modeling and Fuzzy c- mean Clustering in the Beas region of Western Himalaya. The study also been carried out to evaluate the effect of topographic corrections on the accuracy of results obtained using Improved Change Vector Analysis.

Chapter 1 as 'Introduction' provides brief description about snow, snow cover, importance of snow cover monitoring in general and in the Himalayan terrain in particular. Basic principles of satellite based remote sensing and spectral reflectance characteristics of various land covers are also briefly explained. The layout of the thesis has been given at the end of the chapter.

Chapter 2 covers a comprehensive literature survey of various models and methods of snow cover monitoring, influence of topography on snow spectral characteristics, the change detection techniques in snow cover area and the impact of topography on the accuracy of detected changes, the implementation of sub pixel techniques for improving the classification accuracy in the imagery obtained from satellites providing higher temporal resolution but medium to moderate spatial resolution, thereby, providing the motivation for this work. It also covers the problem formulation and methodology for the present work.

In chapter 3, the brief overview of the 'study area and data used' is given. The topography of Himalaya in general and western Himalaya in particular has been described. The importance of the study area is explained. The data used for the analysis i.e. satellite imagery, map sheets, digital Elevation Model (DEM) and data pertaining to field observation used for validation is also described.

Chapter 4 is devoted to the qualitative and quantitative comparative analysis of different topographic models for Himalayan terrain. The main objective of the research in this area is (i) to implement all topographic models for qualitative and quantitative assessment for comparative analysis of snow reflectance estimation using medium resolution satellite imageries forming of a part of Western Himalaya obtained from AWiFS sensors on-board IRS-P6 (ii) visual analysis (iii) validation of terrain corrected satellite estimated reflectance by all these methods with field measurements (iv) testing of topographically corrected results for snow samples on the south and north aspect (v) graphical analysis after topographic corrections and (vi) to find the best suitable method for topographic corrections for Western Himalaya.

Chapter 5 deals with the models and methods of snow cover monitoring. Two sub-pixel classification algorithms such as Fuzzy C-Means Clustering (FCM), Linear Mixture Modeling (LMM), in soft form are used for the precise estimation of various classes in the moderate resolution MODIS images. Thereafter, a new Statistical relationship is developed between the *NDSI* from *MODIS* observations and the fraction of snow-cover at 500-meter grid resolution obtained by LMM and FCM for use as a universal relationship applicable for the entire study area..

Chapter 6 considers the effect of topographic corrections on accuracy of change detection in Himalaya terrain. The main focus of the work here is to analyse the effect of topography on improved CVA and carry out accuracy assessment as compared to conventional CVA.

Chapter 7 covers the summary of conclusions drawn in all the three objective areas. In this thesis work it has been concluded that the effect of topography plays a major role in the accuracy of results obtained from various snow cover monitoring techniques in the rugged mountainous terrain of Himalayas. It is also concluded that none of the present satellite sensors is exclusively suitable for accurate snow cover monitoring in the Himalayan region. Therefore sub pixel analysis is required to be carried out based on the empirical results. At the end future scope of the work has been proposed.

The final chapter 8 ‘List of References’ provides the details of all the references used and referred in this study and thesis work.

The ‘Appendix-A’ gives a brief about the author

LIST OF FIGURES

LIST OF TABLES

CHAPTER 1

Introduction

Chapter 1

INTRODUCTION

1.1 Snow and Snow Cover

Snow is a complex medium consisting of ice, air and water vapor. Snow is formed from crystallization of ice particles in the atmosphere during precipitation. Snow is a very porous medium. By visual examination, snow can be classified as crystalline, powdery, granular, pellet and mixtures. As per the grain size, it can be classified as fine, medium and coarse whereas as per moisture content, it may be classified as dry and wet. Freshly deposited snow consists of dendrites, needles and columns which continuously change in their shape and size. The process which results in the morphological changes in snow structure is called metamorphism (Colbeck, 1982). In order to attain a state of thermodynamic equilibrium, the snow particles tend to form larger clusters thereby minimizing the surface area-to-volume ratio. Other processes that can alter the shape and size of snow particles are temperature gradients brought about by solar radiation, compaction due to pressure, and repeated melt-freeze cycles. Wind speed near the snow surface also affects the snow particle packing and snow surface roughness. When the interconnecting masses between the snow grains are sealed off, it turns in to glacier ice.

In general, a layer of snow on ground surface is called snow cover. Snow remains on the ground until it melts or sublimes. Snow cover is a stratification of the snow pack formed by successive accumulation of number of snowfalls, each occurring with different meteorological conditions. Snow cover commonly occurs at high latitudes and altitudes because the prevailing temperatures facilitate the occurrence of snowfall at increased frequency and reduce the probability of snowmelt.

Snow covers more than 30 % of the Earth's land surface during Northern Hemisphere winter (Robinson and Kukla, 1985). In terms of spatial extent, seasonal snow cover is the largest single component of the cryosphere and has a mean winter maximum areal extent of 47 million square kilometres, about 98 percent of which is located in the Northern Hemisphere.

The snow cover is, therefore, one of the most important of the earth's surface characteristics that influence surface radiation, energy balance, and hydrologic budgets (Foster and Chang, 1993). It is also one of the key factors to consider in the atmospheric circulation, runoff modeling, numerical weather forecasting, and climate change studies (Romanov *et al*., 2000). Changes in snow cover and glacier cover influence the discharge and flow of perennial rivers (Anup Prasad and Romesh P Singh, 2007).

Surface temperature is highly dependent on the presence or absence of snow cover, and temperature trends have been linked to changes in snow cover (Groisman *et al.*, 1994). Snow cover is an important climate change variable because of its influence on energy and moisture budgets. Snow cover accounts for the large differences between summer and winter land surface albedo, both annually and inter-annually. Snow may reflect as much as 80 to 90 percent of the incoming solar energy, whereas a snow-free surface such as soil or vegetation may reflect only 10 to 20 percent. A warming trend results in decreased snow cover. With the resulting decrease in reflected energy, absorption of solar radiation increases, adding heat to the system, thereby causing even more snow to melt. In the last few years, melting of glaciers has been a cause of concern the world over highlighting the importance of regular and accurate and snow cover monitoring.

1.2 Snow Cover in Western Himalaya

The word Himalaya comes from the ancient Indian language Sanskrit and means "abode of snow". Here hima means "snow", and alaya means "abode". The rivers of the Indus, the Ganga and the Brahmaputra originate from Himalaya. These river systems, which have flown throughout the year over the centuries, have the potential to irrigate millions of hectares of agricultural land in more than half of India and generate millions of kilowatts of power, besides supplying drinking water to the large population (Ramamoorthi *et al.*, 1991). The Himalayan region is gifted with abundant snowfields and in the winter most of the high-altitude region experiences heavy snowfall. During summer, snowmelt becomes useful as water resource for electricity, irrigation and fresh water supply for the rivers originating from the Himalaya. The extent of snow cover especially in North Western Himalayas exerts an influence on hydropower generation system, water management, strategic planning and many other developmental activities, which contribute to Indian national economy (Singh *et al.*, 2002). However, snow also turns into a natural hazard in the form of avalanches, a catastrophe which strongly affects the safety of human lives and property. The forecasting of

avalanches has always been of prime importance in view of the inhabitants of the area and for the troops operating in snowbound regions of Jammu and Kashmir and Himachal Pradesh. Therefore, mapping of snow covered areas is an important parameter not only for hydrological and climatological, but also for snow-hazard applications.

Sharma and Ganju (2000) characterized the Western Himalaya in three zones, on the basis of snow climatic conditions, i.e. lower, Middle and Upper Himalayan zone. The Lower Himalayan zone is characterized by moderate temperature receives high precipitation and significant changes in the snow characteristics observe due to moderate temperature. The average altitude of this zone is between 2000–4000m and generally it covers the vegetation below 3000 m. The Middle Himalayan zone is characterized by cold temperatures, mostly glaciated and altitude varies from 3500 to 5300 m. Generally there is no vegetation. The Upper Himalayan zone is extremely cold, receives dry snow and highly glaciated which is somewhat close to continental snow conditions, and altitude is normally more than 5000 m.

In North-West Himalayas, the snow cover area significantly increases with the onset of winter during November and subsequently recedes from April onwards. With this major seasonal variation, different pockets of Himalayas experience different snow covers variation patterns. This localized snow cover variation extends from different ranges of Himalayas to different river basins. This variation in the snow cover extent controls the surface heat exchange system, soil thermal regimes, and melts runoff discharge and hydro-power generation capacity of an area. Snow also turns into a natural hazard in the form of avalanches, a catastrophe which strongly affects the safety of human lives and property. Not only this, the snow cover variation also influences tourist movement and extent of the cropping season on which socio-economic condition and other development activities of a region depends. Therefore knowledge of the dynamic snow cover changes is of major importance in Himalayas.

1.3 Monitoring and evaluation of Snow cover

For snow cover monitoring, it is necessary to accurately estimate the area covered under snow. In order to investigate the large scale distribution of snow covered areas using in-situ data, snow surveys need to be conducted in short time, which at times are not feasible and are also uneconomical. Furthermore, the in-situ data are collected at point locations during snow surveys provide mostly isolated information on snow characteristics such as

grain size, grain shape, free water content or surface roughness (Buhler *et al*.,2009). Large parts of the Himalayas remain covered throughout the year and is often inaccessible which makes manual snow cover monitoring very tedious and expensive task due to ruggedness of terrain and lack of infrastructure and limited regional information. For such snow covered inaccessible places, accurate data collection by ground based and conventional methods is very difficult, thus inputs received from manned observatories, automatic weather stations (AWS) and other conventional techniques are insufficient to provide entire regional information as they are point specific.

Alternatively, remote sensing data acquired from sensors fitted on aerial platforms or on-board a number of Earth Observation Satellites appears, attractive for monitoring snow-covered areas spatially. Satellite remote sensing in particular has emerged as a very useful tool for collecting real time, year round and large spatial coverage over vast, rugged and remote areas (Konig *et al.,* 2001). Satellites are also well suited to the measurement of snow cover because the high albedo of snow presents a good contrast with most other natural surfaces except clouds. Remote sensing data acquired from sensors on- board a number of satellites became attractive for monitoring snow-covered areas spatially. Satellites are also well suited to the measurement of snow cover because the high albedo of snow presents a good contrast with most other natural surfaces except clouds. The interest in the usage of satellite remote sensing data for snow cover geared up rapidly in the 1970s with the launch of Landsat series of satellites. Snow cover has been monitored on weekly basis in the Northern Hemisphere since 1966 using a variety of sensors, including the Scanning Radiometer (SR), Very High Resolution Radiometer (VHRR) and the Advanced Very High Resolution Radiometer (AVHRR) (Matson et al., 1986; Matson, 1991). The launch of Moderate Resolution Imaging Spectrometer (MODIS) on-board Terra Satellite in1999 and later on Aqua Satellite in 2002 has provided hyperspectral image data for producing reasonably accurate snow maps globally. Medium resolution optical imagers are particularly useful for this task because of frequent repeat observations and good radiometric capabilities.

1.4 Satellite based Remote Sensing

Remote sensing can be broadly defined as the collection and interpretation of information about an object or area without being in physical contact with the object. Man’s

remote sensing of the earth, using instruments other than the naked eye, began in 1859 with Gaspard Tournachon's photograph from a balloon of a village near Paris, France. Today we are using images taken from sensors throughout the Electromagnetic Spectrum extending from the ultraviolet to microwaves (Goetz *et al.*, 1985). The retrieval of information in remote sensing applications is by the use of electromagnetic energy sensors that are currently operated from airborne and space borne platforms to assist in inventorying, mapping and monitoring earth resources. These sensors acquire data the way various earth surface features emit and reflect energy, and this data is analyzed to provide information about the resources investigated (Lillesand *et al.*, 1999).

1.4.1 Electromagnetic spectrum

The electromagnetic (EM) spectrum is the continuous range of electromagnetic radiation, extending from gamma rays (highest frequency and shortest wavelength) to radio waves (lowest frequency and longest wavelength) and including visible light. The EM spectrum can be divided into seven different regions: gamma rays, X-rays, ultraviolet, visible light, infrared, microwaves and radio waves having as shown in Figure 1.1 (Campbell, 1987).

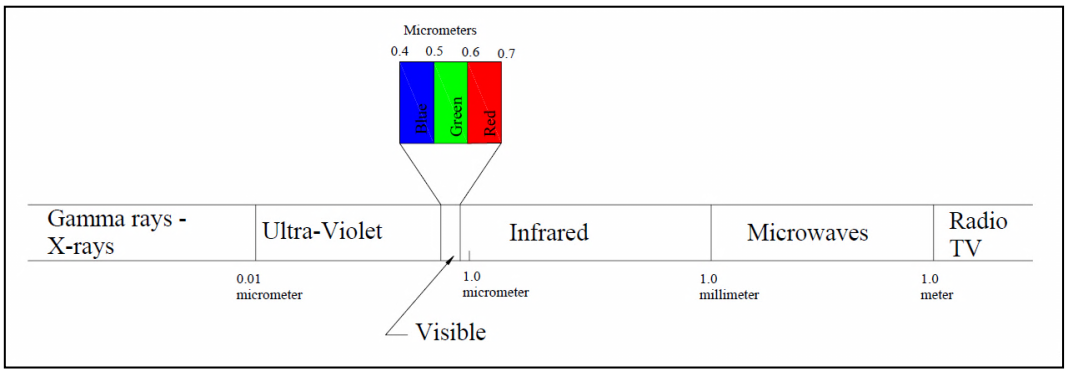

Figure 1.1 Electromagnetic Spectrum

The earth's atmosphere absorbs energy in the gamma rays, X rays and most of the ultra violet region, therefore these regions are not used for remote sensing applications. The major regions of interest in satellite remote sensing are visible light, reflected and emitted infrared, and the microwave regions. Collection of information over a large numbers of wavelength bands is referred to as multispectral or hyperspectral data.

1.4.2 Classification of Remote Sensing systems

Remote Sensing systems are broadly classified into two broad categories based on source EM energy interacting with the target object: -

a) **Active Remote Sensing**: - These systems use their own source of EM energy which directed towards the object and return energy is detected and measured by the sensors. The source of energy is a part of the sensor system. RADAR and LIDAR are the examples of active systems.

b) **Passive Remote Sensing**: - These use sun as a source of EM energy and record the energy that is naturally radiated or reflected from the objects. The other source of energy is the Earth and its atmosphere.

1.4.3 Spectral Signatures

Spectral signature can be defined as set of values of reflectance of an object, which lead to the identification of the object/phenomena or its condition. Inherent characteristics of radiation, spectral, spatial, temporal, and polarization variations help in identifying an object (Navalgund *et al.*, 2007.). Spectral variations are the variations in the reflectance of objects as a function of wavelength. The shape, size, texture of objects provides spatial variations. Temporal variations are the changes of reflectivity or emissivity with time. They can be diurnal and/or seasonal. Polarization variations relate to the changes in the polarization of the radiation, reflected or emitted by an object. The degree of polarization can help in identifying an object, particularly in microwave region. Signatures are statistical, not deterministic as reported (Jensen, 2003). The spectral response of elements of the Earth surface is explained in the next section.

1.4.4 Spectral Reflectance Characteristics of Snow and other Earth's Surface Features

a) **Vegetation**- Large area of the earth's surface is covered by vegetation and one of the most important natural resource. (Irving *et al.*, 1968). The leaf pigments, internal cellular structure and water content govern the spectrum in visible, near IR and middle IR wavelengths, respectively. Chlorophyll absorbs at 0.45 and 0.65 μm and reflects the 'green' part of spectrum and thus vegetation look green to us. Reflectance curve of green and dry vegetation is shown in Figure 1.2.

b) **Soil**- Generally, soil shows increasing reflectance with wavelength in visible and infrared region (Irving *et al.*, 1968). The soil moisture, organic matter, relative

concentration of sand, silt, clay, iron oxide and roughness of soil surface affect `the spectral response. Reflectance curve of soil is shown in Figure 1.2.

c) **Snow and Cloud**- Snow has very high reflectance in visible and near IR region and then reduces in middle and IR regions. (O'Brian *et al.*, 1975). Cloud appears bright in 0.3-3 μm to distinguish cloud and snow. Reflectance curve of snow is shown in Figure 1.3. The regions 1.55-1.75 and 2.11-2.35 μm are useful for snow cloud discrimination.

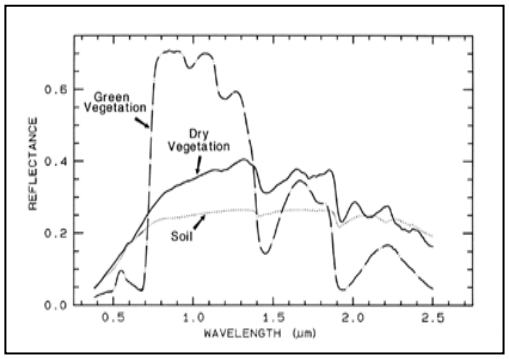

Figure 1.2: Reflectance curve of Soil and vegetation

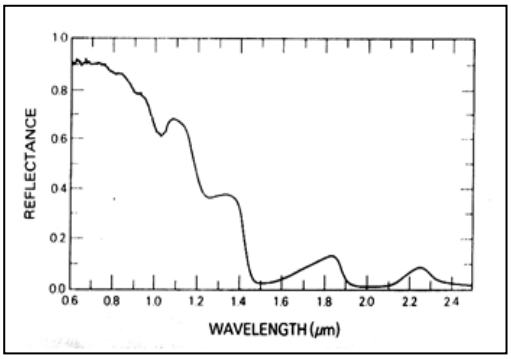

Figure 1.3: Reflectance curve of Snow

1.4.5 Remote Sensing Satellites and Sensors

Unlike airborne platforms, the satellites in space are very less affected by atmospheric drag; hence their orbits can be very well defined. Therefore, the entire earth or any designated portion can be covered at specified intervals synoptically. Polar orbiting satellites are generally used for remote sensing applications. These revolve around the earth in low Earth Orbits (LEO) having altitude between 300 to 1500 Km. The Remote Sensing (RS) satellites are designed to follow sun-synchronous orbits defined by fixed inclination angle from the earth's N-S axis. The orbital plane rotates to maintain precise pace with the sun's westwards progress as the earth around the sun. The position in reference to the sun being fixed, the satellite crosses the equator precisely at the same local time. The RS Sensor is a device that gathers electromagnetic energy, converts it into a signal and presents it in a form suitable for obtaining information about the target under investigation.

1.4.6 Characteristics of RS Sensors

(a) Scanning Mechanism: The two main scanning techniques employed for recording the incoming EM energy are (i) Opto-Mechanical Scanners used in earlier satellites had a fixed

sized mirror rotating along an axis. The energy received from the ground is focused on a spectrometer or grating for dispersion into designed spectral bands. The reflected radiation is then focused on an array of photovoltaic cells. The energy sensed in different bands is then calibrated. (ii) CCD Scanners do not have any moving parts. The energy coming from the earth is directed on to an array of CCDs for calibration and conversion to digital Numbers (DN). Majority of the current satellites employ this technique in view of better quality of signal.

(b) Sensor Resolution: Four different types resolutions are used in satellite remote sensing applications:

i. **Spatial Resolution.** Spatial resolution is a measure of the linear dimension on the ground represented by each pixel in the image. Higher the resolution the smaller the area/ objects on the surface of the earth which can be identified. Landsat, SPOT, IRS satellites sensors have 20m to 30m resolution. The new satellites like IKONOS, Orbview have even sub-meter resolution. The wide coverage sensors AWiFS and MODIS have 56 and 180 m resolution.

ii. **Spectral Resolution.** The width of the electromagnetic spectrum that is devoted to a particular sensor band is called spectral resolution. High resolution sensors can discriminate very fine differences in spectral reflectance. Multispectral sensors generally have spectral resolution of the order of 0.1 μm where as it is 0.01 μm for hyperspectral sensors.

iii. **Radiometric Resolution.** It refers to the number of available brightness values (BV) in each band of data, and is determined by the number of bits into which the recorded energy is divided. It describes the sensitivity of the sensor to variations in brightness. In 8-bit data, the brightness values can range from 0 to 255 for each pixel (256 total possible values). In 10-bit data, the values range from 0 to 1028.

iv. **Temporal Resolution.** It means as to how often a sensor can obtain imagery of a particular area of interest, determined by the repeat cycle of its orbit. For example, the Landsat satellite revisits an area every 16 days as it orbits the Earth, whereas IRS has 24 days repeat cycle for LISS III and 5 days for AWiFS.

(c) Swath. It is the overall linear ground distance covered by a sensor in a single satellite pass. The higher satellites having lower repeat cycles have higher swath. IRS-P6 sensor LISS

III sensor covers 141 Km , LISS IV sensor covers 70 Km and AWiFS covers 737 Km in one pass whereas MODIS has a swath of 2350 Km.

1.5 Application and Limitations of Satellite based Remote Sensing techniques of Snow Cover over Western Himalayas

The advent of satellite observations has opened up a new avenue for monitoring and assessment of snow cover. The areas which are remote and inaccessible like high mountainous terrain can be surveyed easily because of satellite's synoptic and repetitive capability. However, adequate resolution for a given area under study is an important aspect to obtain the accuracy of measurements. Himalayan region has very high concentration of mountain glaciers and it is completely covered by snowfall during winter period between November and April. Very few studies on the use of IRS satellite sensor data have also been reported in the Himalayan region (Kulkarni 1986, Kulkarni and Dhanju 1987). Snow cover monitoring using visible and near infrared images sometimes becomes difficult due to presence of cloud cover and due to long mountain shadows. The demand of snow cover monitoring in this region has gained importance in order to find the solution to some of the related issues such as global warming, lack of water supply, electrification in rural areas and hazard forecasting etc. (Ramamoorthi and Haefner 1991).

The mapping of snow cover in Himalayas is affected by a number of factors. This region is very frequently covered by clouds which are one of the most important factors responsible for inaccuracy in snow cover mapping. Therefore, one has to devise and employ the snow and cloud discrimination techniques. Higher resolution sensors which have inherently low repeat cycles cannot be used for high frequency monitoring. Mapping of snow in areas with large forests is another problem. It may be difficult, even with field measurements and high resolution air photos, to determine the percentage of snow covered area. In steep mountainous terrains, especially with low sun angle in mid winter, the mountain shadow causes problems determining the snowline or the snow extent. Some of the major factors affecting the snow cover monitoring in Western Himalayas are as under:

1.5.1 Effect of Topography

Mountain topography has a significant influence on the qualitative and quantitative estimation of snow and other land cover characteristics (Dozier and Marks, 1987). The

variations of the topographic parameters affect the variations in the brightness of the satellite images having different spectral and spatial resolution. The topographic corrections or topographic normalization refers (Riano *et al.*, 2003) to the compensation of differential solar illumination due to rugged shape of the mountainous terrain. Differential illumination results in considerable variation in the spectral characteristics of similar snow and other land covers. Sun-facing illuminated slopes (south aspect) show more than expected spectral radiance or reflectance, whereas the effect is opposite in shaded relief area (north aspect) (Riano *et al.*, 2003). These differential illumination effects in satellite imagery suppress the maximum information on the north-facing slopes, thereby adversely affecting the results of various quantitative methods of snow cover monitoring namely classification, sub pixel information, temporal change analysis and other hazard related information. The direct solar irradiance on any inclined pixel is different as compared to flat surface on the satellite images. Therefore, effective removal or minimization of terrain effects is essential for snow cover monitoring.

A wide range of commonly used topographic correction methods are reported in the literature (Minneart, 1941; Smith *et al*., 1980; Teillet *et al.*, 1982; Dozier, 1984; Hall *et al.*, 1988; Leprieur *et al.*, 1988; Civco, 1989; Colby, 1991; Tokola *et al.*, 2001). Generally, these methods have been used for qualitative analysis and mapping of vegetation types and forest cover. In very few cases, some of these topographic correction methods (Dozier, 1984; Hall *et al*., 1988, Civco, 1989) have been used for snow applications in Himalayan terrain but the results are not validated with in-situ observations. Therefore there is a need to compare the main important topographic correction methods such as C-correction Minneart corrections, two-stage normalization and slope matching technique on snow covered areas of Himalaya terrain and propose the best suitable method for this region.

1.5.2 Performance of snow cover monitoring algorithms

Until recently snow cover mapping and monitoring was being carried out based on data acquired from satellite sensors such as LANDSAT MSS and TM, IRS LISS III etc. which unfortunately were saturated for snow due to its high reflectance in most of their spectral regions. Moreover, the mapping process was also largely based on the conventional techniques such as manual delineation of snow/glacier cover boundaries, segmentation of ratio images and hard or crisp classification algorithms such as Maximum Likelihood Classifier (MLC). The main assumption in using these methods is that the classes are discrete

and mutually exclusive, and therefore each pixel is treated as pure consisting of one and only one class.

MODIS (Moderate Resolution Imaging Spectrometer) on-board Aqua and Terra satellites and AVHRR (Advance Very High Resolution Radiometer) on-board NOAA satellites and AWiFS (Advanced Wide Field Sensor) on-board Indian Remote Sensing Satellite (IRS) P6 'Resourcesat-1' are not saturated for snow applications. These satellites have also facilitated the effective monitoring of large snow covered areas as a result of high temporal resolution and wide swath coverage. However, the data provided from these sensors are at medium to moderate spatial resolution ranging from 56 m of AWiFs to 250 m, 500 m and 1000 m of MODIS, which brings the problem of mixed pixels (i.e., pixels containing more than one class). To overcome this problem, a number of techniques for mapping the land cover at sub-pixel level have been developed. These include maximum likelyhood classifier (MLC), linear mixture modeling (LMM) (Nolin *et al*. 1993; Rosenthal and dozier, 1996; Painter *et al*. 1998, 2003; Vikhamar and Solberg, 2002, 2003; Foppa *et al.* 2004), artificial neural network (ANN) (Foody and Arora, 1997; Gopal et al 1996), decision tree classification (Friedl and Brodley, 1997; Ghose *et al* 2010), object-based classification methods (Forster *et al.*) etc. However, not all these techniques have yet been explored for snow-cover sub-pixel mapping (Foody and Arora, 1996, 1997; Tiwari *et al*. 1999; Arora, 1999). The literature suggests the use of empirical relationships (Kaufman *et al*. 2002, Barton, 2002; Salomonson and Appel, 2004, 2006), LMM (Nolin *et al*., 1993; Rosenthal and dozier, 1996; Painter *et al*. 2003; Foppa *et al*.2004) Vikhamar and Solberg, 2002, 2003; Foppa *et al*. 2004) and ANN (Simpson and McIntire, 2001), for snow cover mapping at sub-pixel level. The application of these models has yet not been explored for Himalayan snow cover as complex topography influences the results and inability to map snow in mountain shadows.

1.5.3 Change Detection analysis of Snow Cover

The Western Himalaya is covered with snow mainly due to elevated mountain ranges. In addition, large areas of Himalaya receive significant snow fall during winters which start ablating with the onset of spring. It is necessary to accurately measure the extant of this snow cover on repetitive basis for efficient strategic planning, water management and avalanche forecasting. Change detection based on satellite data acquired on regular intervals has emerged as the most viable and cost effective method

for mapping of areal extant and reflectance of snow cover (Kulkarni *et al.*, 2002a) since it is possible to acquire two different date data approximately at the same time, to reduce the diurnal sun angle effects that cause unusual differences in the reflectance properties of the satellite data. There are number of way to discriminate the changes between two dates of images such as Image Differencing, Image Ratioing, Principal Component Analysis (PCA) and Change Vector Analysis (CVA) etc. (Jensen, 1996). A synoptic review of large number of change detection techniques used by various researchers using remote sensing images are summarized or classified from different viewpoints (Coppin *et al.*, 2004; Lu *et al.*, 2004). It has generally been agreed that change detection is a complicated and integrated process. No existing approach is optimal and universally applicable to all cases. Standard change vector analysis (CVA) is cited as an effective change detection tool (Warner 2005) that characterizes movement in spectral space over time in terms of magnitude and direction. Improved/modified CVA has been proposed to overcome the problem of reasonably determining thresholds of change magnitude and change direction. The analysis has been mostly restricted out in plain or low altitude areas. There is a need to analyse the impact of topography on the accuracy on these change detection techniques.

1.6 Objectives of the Study

Based upon the limited application and performance evaluation of remote sensing techniques and algorithms in the rugged Himalayan terrain and various identified gaps, the objectives of the research work were formulated in 2007 which are as follows:

1. Evaluation of influence of topography on snow spectral characteristics in Western Himalayan region using various techniques.
2. Performance analysis of snow covers monitoring algorithms.
3. Evaluation of the influence of topography on change detection in snow covered areas of Western Himalaya.

1.7 Organization of Thesis

This thesis work has been organized in eight chapters as follows:

Chapter 1 as ‘Introduction’ provides brief description about snow, snow cover, importance of snow cover monitoring in general and in the Himalayan terrain in particular.

Basic principles of Satellite based remote sensing and spectral reflectance characteristics of various land covers are also briefly explained. The layout of the thesis has been given at the end of the chapter.

Chapter 2 covers a comprehensive literature survey of various models and methods of snow cover monitoring, influence of topography on snow spectral characteristics, the change detection techniques in snow cover area and the impact of topography on the accuracy of detected changes, the implementation of sub pixel techniques for improving the classification accuracy in the imagery obtained from satellites providing higher temporal resolution but coarse spatial resolution thereby providing the motivation for this work. It also covers the problem formulation and methodology for the present work.

In **chapter 3**, the brief overview of the study area and data used is given. The topography of Himalaya in general and western Himalaya in particular has been described. The importance of the study area is explained. The data used for the analysis i.e. satellite imagery, criterion for the selection of image scenes and data pertaining to field observation used for validation is also described.

Chapter 4 is devoted to the Qualitative and Quantitative comparative analysis of different topographic models for Himalayan terrain. The main objective of the research in this area is (i) to implement all topographic models for qualitative and quantitative assessment for comparative analysis of snow reflectance estimation using medium resolution satellite imageries forming of a part of Western Himalaya obtained from AWiFS and MODIS (ii) visual analysis (iii) validation of terrain corrected satellite estimated reflectance by all these methods with field measurements (iv) testing of topographically corrected results for snow samples on the south and north aspect (v) graphical analysis after topographic corrections and (vi) to find the best suitable method for topographic corrections for Western Himalaya.

Chapter 5 deals with the models and methods of snow cover monitoring. Some sub-pixel classification algorithms such as Fuzzy c-Means Clustering (FCM), Linear Mixture Modeling (LMM), in soft form are used for the precise estimation of various classes in the moderate resolution MODIS images. Thereafter, a new Statistical relationship is developed between the *NDSI* from *MODIS* observations and the fraction of snow-cover at 500-meter grid resolution.

Chapter 6 considers the effect of topographic corrections on accuracy of change detection in Himalaya terrain. The main focus of the work here is to analyse the effect of topography on improved CVA and carry out accuracy assessment as compared to conventional CVA.

Chapter 7 covers the summary of conclusions drawn in all the three objective areas. In this thesis work it has been concluded that the effect of topography plays a major role in the accuracy of results obtained from various snow cover monitoring techniques in the rugged mountainous terrain of Himalayas. It is also concluded that none of the present satellite sensors are exclusively suitable for accurate snow cover monitoring in the Himalayan region. Therefore sub pixel analysis is required to be carried out based on the empirical results. The future scope of the work has also been recommended

The final **chapter 8** on 'List of References' provides the details of all the references used and referred in this study and thesis work.

The **'Appendix-A'** gives a brief about the author.

CHAPTER 2

Review of Literature

Chapter 2

REVIEW OF LITERATURE

2.1 Spectral Properties of snow

Reflectance of snow is higher in the near ultra-violet and visible portion of Electromagnetic Spectrum (EMS) (0.3-0.7μm) whereas it decreases rapidly in near- infrared (NIR) and mid-infrared (MIR) regions of EMS (0.8-1.5μm) and remains low for subsequent wavelengths as compared to other surfaces as shown in Figure 2.1. The local maxima of the reflectance occur at 1.1 μm, 1.3 μm, 1.8 μm and 2.2 μm corresponding to local minima in the absorption coefficient of ice (O'Brain and munis, 1975; Wiscombe and Warren, 1980; Bolsenga and Kistler, 1982). Reflectance of snow can vary considerably, depending on several factors such as metamorphism, grain size , moisture content, contamination, clouds and sensors and solar geometry (Wiscombe and Warren, 1980; Dozier,1989; Winther 1993). As the snow ages, the reflectance generally decreases. In NIR and MIR regions, the decrease is mainly due to grain size growth, while in visible region it is mostly due to a higher concentration of impurities in the snow pack (Hinkler *et al*. 2002) as shown in Figure 2.2. Thus, the clean, deep snow appears bright and white in visible region of the EMS, irrespective

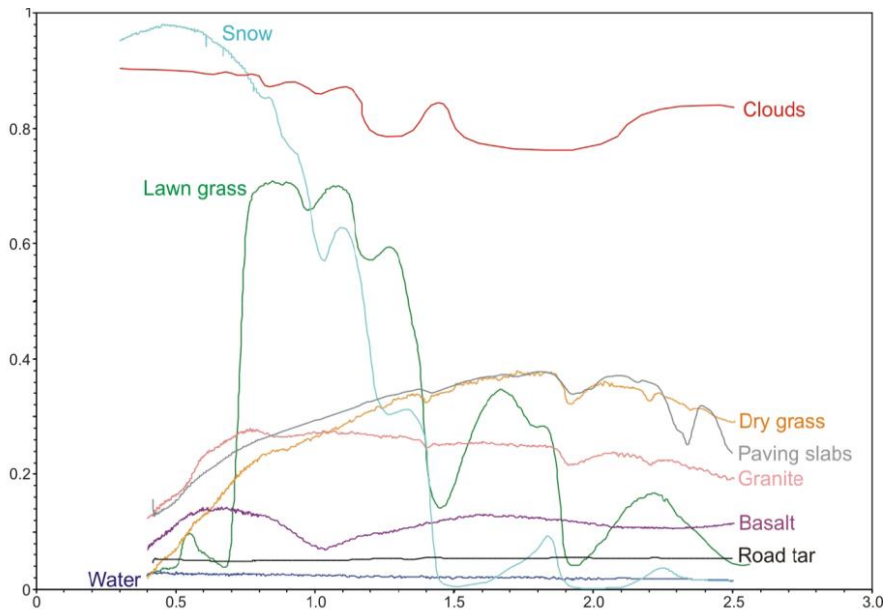

Figure 2.1 Spectral Reflectance curves of some common materials

(Source www.asdi.com/Spectral-Measurements)

of the grain size. However, in the NIR and MIR regions, freshly fallen snow usually has a fine grain size, but metamorphism throughout the winter and spring seasons increases the grain size and reduces reflectance in wavelengths beyond about 0.8 μm.

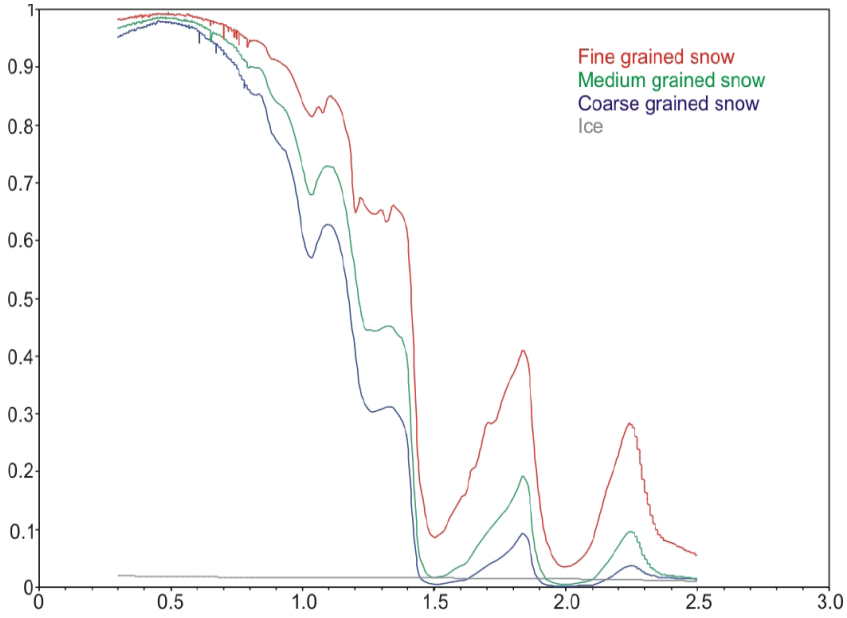

Figure 2.2 Spectral Reflectance curves of different types of Snow

(Source www.asdi.com/Spectral-Measurements)

A surface is said to be perfectly smooth if the reflection from it obeys the Snell's Law, which states that is the angle of reflection is equal to the angle of incidence, when the incident ray, reflected ray and the normal to the plane of incident are in the same plane. The reflectance from the surface which follows Snell's Law is called specular reflection (Joseph, 2003). The reflection from the rough surfaces is called diffuse reflection. The angular distribution of the reflected ray varies with the surface property. If the emergent radiance is constant for all directions in a hemispherical solid angle then the surface is called Lambertian reflector since it obeys the Lambert's Law, which states:

$$I\ (\theta)\ =\ I_{o}\ Cos\ \theta \qquad (2.1)$$

where I (θ) is the intensity as a function of angle from the perpendicular to the surface, θ is the angle from the perpendicular, I_0 is the intensity at θ = 0. However, the surfaces encountered in real world are neither perfect Lambartian nor perfect specular.

There are three types of solid angles that can be considered to define reflectance values namely directional, hemispherical and conical (McCluney, 1994). The term directional

refers to infinitesimally small solid angle in a specified direction (θ, φ) from the point P of interest. The term Hemispherical refers to a full 2 Π steradian of the hemisphere. Conical refers to an intermediate size of solid angle. Depending upon the solid angle associated with the incident and emergent ray, nine possible definition of reflectance are possible (Joseph, 2003).

The direct albedo is called the directional-hemispherical reflectance and the diffuse albedo is called bihemispherical reflectance (Rencz and Ryerson, 1999). The reflectance property of the surface can be completely described by the bidirectional reflectance distribution function (BRDF), which gives the reflectance of a target surface as a function of the illumination geometry and view geometry, Figure 2.3. The BRDF depends on wavelength and is determined by the structural and optical properties of the surface, such as shadow-casting, multiple scattering, mutual shadowing, transmission, reflection, absorption and emission by surface elements, facet orientation distribution and facet density. The BRDF of a surface is the ratio of reflected radiance to incident irradiance at a particular wavelength as given by:

$$P(\theta_{i,}\, \varphi_{i,}\, \theta_{r,}\, \phi_r\, ;\, \lambda) = d\, L_r\, (\theta_{i,}\, \varphi_{i,}\, \theta_{r,}\, \phi_r\, ;\, \lambda\,)/(d\, E_i\, (\theta_{i,}\, \varphi_{i\,;}\, \lambda\,) \qquad (2.2)$$

where the subscripts i and r denote incident and reflected respectively, (θ, φ) is the direction of light

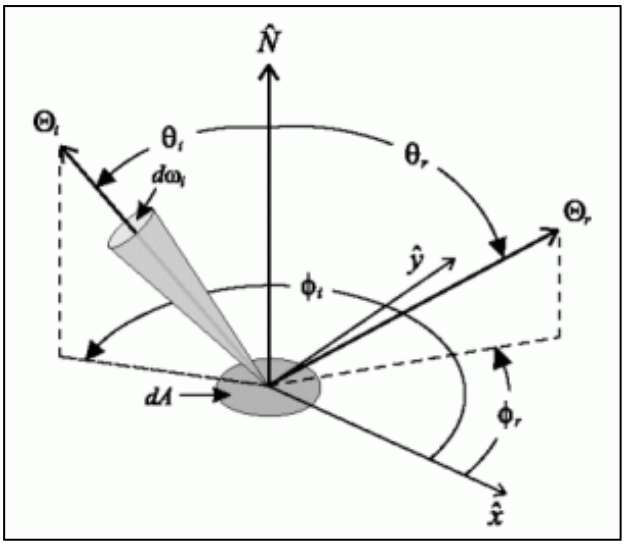

Figure 2.3 Light reflection geometry (Source math.nist.gov)

propagation, λ is the wavelength of light, L is radiance, and E is irradiance. BRDF measurements are given in sr^{-1} and for a Lambertian surface BRDF is 1/ Π.

2.2 Reflectance Modelling

The spectral region between 0.35 μm and 3.5 μm is called the reflective part of the electromagnetic spectrum. The reflectance varies strongly with the wavelength and the resulting reflectance curve is unique for each surface type. The spectral reflectance of snow also varies strongly with wavelength (Warren, 1982; Dozier, 1989). The extraction of different objects from remote sensing data is based on variation in reflected energy in various portions of the reflective portion of the electromagnetic spectrum.

The ratio of the spectral distribution of the flux incident at and reflected by the surface is proportional to the spectral reflectance $\rho(\lambda)$ of the surface. The wave length dependence can be mathematically represented as:

$$\rho(\lambda) = \pi L_\lambda / E_\lambda \qquad 2.3$$

Thus, the spectral distribution of the surface radiance L_λ depends both on the spectral reflectance of surface $\rho(\lambda)$ and the spectral distribution or the content of the incident irradiance E_λ (Markham and Barker, 1986, 1987).

On a satellite image, this reflected energy is normally represented as a decimal value known as digital number (DN) and depends on the calibration parameters and radiometric resolution of the sensor. The actual reflectance from an object depends on various parameters, such as, solar elevation, surface slope and its orientation, surface anisotropy, and atmospheric constituents (Srinivasulu J and A V Kulkarni, 2004). Therefore, accurate extraction of object/features requires data to be expressed in physical units, such as radiance or reflectance because raw digital numbers (DNs) derived from satellite optical systems cannot confidently be used for studied related to snow cover monitoring. Reflectance also forms an important input in estimating NDSI, which is useful for mapping the area as snow or non-snow, for discriminating snow from cloud cover and for identification of snow under the conditions of mountain shadow. It also a key parameter for mapping snow in the area covered with both snow and vegetation.

2.2.1 Satellite based reflectance

Estimation of spectral reflectance from various sensors on-board various satellites is the prime requirement for monitoring and mapping of snow cover. The total radiance signal at the satellite sensor consists of mainly three components as under:

(a) Path radiance (L1) consisting of photons scattered into sensor' instantaneous field of view, without having ground contact.

(b) Reflected radiation (L2) from a certain pixel which contains the direct and diffuse solar radiation incident on the pixel reflected from the surface.

(c) Radiation reflected from the neighborhood (L3) which is scattered by air volume into the instantaneous direction. This is called adjacency radiance.

The total radiance signal L_λ can be written as:

$$L_\lambda = L_{path} + L_{reflected} + L_{adjency} \quad (2.4)$$

Out of these three, only the radiation component L2 contains the information from the currently viewed pixel. The path radiance decreases with increasing wavelength. It is usually very small for wavelengths greater than 0.7 μm. The adjacency effect is caused by complicated multiple scattering in the atmosphere-land surface system. In particular, the pixels of high-resolution spatial images acquired over a heterogeneous landscape are affected by scattering component from their neighboring pixels. As a result, dark pixels look brighter and bright pixels look darker. The practical implication to remotely sensed data is that imagery typically looks hazy and lack contrast. As the spatial resolution increases, the adjacency problem represents between-pixel effects. The mixture problem has been extensively investigated, but the effects of adjacency are continued to be investigated.

Earlier studies on the adjacency effect can be grouped into two broad categories: (a) using the atmospheric point spread function (PSF) and (b) developing empirical formulae. Different methods have been explored to calculate the atmospheric PSF, including Monte-Carlo simulations and radiosity simulation. The adjacency effect can be corrected by using the Fourier-transform approach given the atmospheric PSF. Although efforts have been made to develop empirical function of the atmospheric modulation transfer function (MTF) that is the Fourier transform (FT) of the atmospheric PSF, most methods for calculating the atmospheric PSF/MTF are computationally expensive. A technique for correction of the atmospheric Point Spread Function was applied to the Landsat Thematic Mapper (TM) at 30 meters resolution up to a distance of 20 pixels around the viewed pixel in a reasonable processing time (Ouaidrari and Vermote, 1999). However, the influence of adjacency effect decreases with wavelength and can usually be neglected for spectral bands beyond 1.5 μm (Richtor, 2004).

2.2.2 Various corrections in the Reflectance model

Ideally, the radiant flux recorded by a remote sensing system in various bands is an accurate representation of the radiant flux actually leaving the feature of interest on the Earth's surface. Unfortunately, noise (errors) can enter the data collection system at several points. For example, radiometric error in remotely sensed data may be introduced by the sensor itself when the individual detectors do not function properly or are improperly calibrated (Tillet, 1986). Secondly, the intervening atmosphere between the terrain of interest and the remote sensing system can contribute to the noise (i.e. atmospheric attenuation) that the energy recorded by the sensor does not resemble that was reflected or emitted by the terrain. Thirdly the radiometric distortion called as topographic effect may occur due to variation in terrain parameters. The topographic effect results from the difference in illumination due to angle of the sun and the angle of terrain resulting in variations in the image brightness values.

2.2.2.1 Atmospheric Corrections

The effects of atmosphere upon the remotely sensed data are not considered errors, since they are part of the signal received by the sensing device. However, it is often important to remove the atmospheric effects, especially for scene matching and change detection analysis. The reflectance of the objects recorded by satellite sensors is generally affected by atmospheric absorption and scattering, sensor-target-illumination geometry, and sensor calibration (Teillet, 1986). These normally result in distortion of the actual reflectance of the objects that subsequently affects the extraction of information from images. There has been considerable research on the need to and the ways of correcting the satellite data for atmospheric effects (Song *et al*., 2001; Campbell *et al*., 1994; Chavez, 1988; Collett *et al*., 1997; Forster, 1984; Furby and Campbell, 2001; Hall *et al*., 1991; Milton, 1994; Schott *et al*., 1988; Yang *et al*., 2000; Yuan and Elvidge, 1996). Decision about the need to correct for atmospheric effects is often a critical first step that can affect subsequent steps in applications of satellite data. For instance, the need for atmospheric correction in change detection studies is generally related to the methods used. In linear methods of change detection such as simple image differencing, there is no need to correct the images as long as the stable classes in the differenced image have a zero mean (Song *et al*., 2001). They have also shown that atmospheric correction affects the results of ratio transformations such as Normalized Difference Vegetation Index (NDVI) and that image classification in the image analysis

procedure is least affected by correction. They have further stated this to be especially true when the training data and the image to be classified are at the same radiometric scale (i.e., both corrected or both non-corrected).

Over the years, a number of algorithms have been developed to correct for variations in atmospheric transmissions. Some of these are: Dark object subtraction (DOS), Radiance to reflectance conversion, Linear regression and Atmospheric modelling, etc. The dark object subtraction technique assumes that the pixel of lowest DN in each band such as deep clear water in the NIR region should really be zero. Thus its radiometric value is the result of atmosphere induced additive errors (Crane, 1971; Chavez *et al*., 1997). However it still is the most commonly used technique. Radiance to reflectance conversion requires knowledge of the true ground reflectance of at least two targets in the image. These can either be obtained from the ground reflectance measurements or may be referred from the reflectance tables of standard materials.

Two methods for radiometric corrections are absolute radiometric correction and relative radiometric correction (Thome *et al*. 1997). The absolute correction method converts digital numbers into surface reflectance or radiance by removing the effects caused by atmospheric attenuation, topographic condition and other parameters. The absolute radiometric correction methods are grouped into physically-based or image-based methods. Physically-based methods are the most complex and can be used in different atmospheric conditions including seasonal and geographic variations, atmospheric scattering, and absorption and can provide highly accurate surface reflectance of varying wavelengths. The commonly used physical-based methods include 5S (Tanre *et al*., 1990), 6S (Vermote *et al*., 1997), Moderate Resolution Atmospheric Radiance and Transmittance (MODTRAN) model and LOWTRAN model (Ritcher 1985, Palluconi *et al*. 1996). Tanre *et al*., (1997) developed an operational atmospheric algorithm for computing the surface reflectance in MODIS visible to middle-infrared bands. They used 6S code as the reference to verify the results from MODIS atmospheric correction algorithm developed. These methods require in situ atmospheric measurements and radiative transfer codes to correct for atmospheric effects. In practice, it is often impossible to collect the in situ atmospheric parameters for many applications. Hence, image-based methods have been developed. Inputs required to these methods are mainly based on image digital numbers and the metadata, such as image acquisition date, sun elevation angle, gain and bias etc., as available in image header file, which provides some important information. The most straightforward method is the

apparent reflectance model (Chavez 1989, Hill 1991), which converts apparent or at-satellite radiance to surface reflectance by correcting sensor gain, offset, solar irradiance and solar zenith angle, but ignoring the correction of atmospheric scattering and absorption. The relative radiometric correction methods focus on relative calibration and are based on histogram matching and regression equation models.

2.2.2.2 Anisotropic reflectance Corrections

Anisotropic reflectance correction describes a condition where materials imaged within a scene exhibit different radiometric values when sensed from different view directions, because their reflectance varies as a function of view and solar angle. Snow like all other natural surfaces, is an anisotropic reflector (Salomonson and Marlatt, 1968; Steffen, 1987). The reflectance from snow is greatest in the forward direction and is generally specular. Measurements of snow BRDF show that the anisotropic reflection of snow is generally characterized by strong forward scattering (Dozier et al., 1988; Hall and Foster 1993; Nolin and Dozier, 1993; Winther, 1993; Winther *et al*., 1999; Winther, 1994). The degree of anisotropy increases with increasing solar zenith angels and increasing snow grain sizes. The freshly fallen snow is generally approximated as a Lambertian reflecting surface. However, as the snow metamorphoses the specular component characteristic of forward scattering increases. (Dirmhirn and Eaton, 1975; Steffen, 1987). For smooth snow surface the forward scattering is by the grains and the peak accounts for a greater fraction of the reflectance in the near-infrared wavelengths where the snow is more absorptive because of the light emerging from the snowpack is likely to have undergone fewer scattering events (Mishchenko *et al*., 1999; Leroux *et al*., 1999; Nolin and Liang, 2000). However, in the case where the snow surface is rough, the reflectance peak may be in the backward direction because of shadowing by large rough features (Warren *et al*., 1998). Since the energy reflected from the snow surface is unevenly distributed among various reflection angles, the knowledge of actual angular distribution of this reflected energy is required to correctly account for anisotropic scattering effects. BRDF functions for snow surfaces can determined by two methods; first approach is to measure BRDF directly from the field or satellite observations and the second approach employs radiative transfer models to simulate BRDF. This model requires snow pack optical thickness, single scattering albedo, and description of the scattering phase function.

A large number of studies have been carried out for the measurement of bi-directional reflectance measurements from the snow and ice surface (Leshkevieh *et al*., 1990; Steffen, 1996; Greuell and de Wildt, 1999; Knap *et al*., 1999). The importance of surface roughness for snow was recognized and study was carried out to assess its effect on BRDF (Khun, 1974, 1985). Snow surface can exhibit many different forms of surface roughness including suncups and penitents but the most important by far is sustrugi which covers vast areas of Polar Regions. However, (Warren *et al*., 1998) found the effect of sastrugi negligible for near-nadir views. They also found that sastrugi have little effect on BRDF for viewing zenith angles less than 50 degrees at 0.09 μm wavelength and 67 degree solar zenith angle. This effect would be even smaller at lower zenith angles.

2.2.2.3 Topographic Corrections

The sensor onboard the satellite views the earth as a plain surface. However, in mountain regions like the Himalayas, the terrain has a variety of undulations and orientations. Hence, the satellite-obtained spectral radiances may not represent true values over inclined surfaces because of terrain effects. The optical remote sensing data in mountainous terrain is affected due to sharp variations in the topographic parameters such as altitude, slope and aspect. This, in turn, has a significant influence on estimation of snow and other land cover characteristics. The variations of the topographic parameters affect the variations in the brightness of the satellite images having different spectral and spatial resolutions. A wide range of commonly used topographic correction methods have been reported in the literature review. These methods may be grouped into two categories: those based on band ratios and those requiring information from digital elevation models (DEM) as inputs. The topographic correction models based on band ratios are simpler, wherein the reflectance is assumed to increase or decrease proportionally in the two bands of the ratio. Therefore, the quotient between them compensates for topographic effects (Colby, 1991). The second group of topographic correction methods is based on the illumination conditions and requires DEM of the area as input (Civco, 1989). Once illumination is computed for the whole image, the reflectance for flat surface is normalized using different methods.

2.2.2.4 Influence of topography on snow spectral characteristics

In mountainous terrain, slope and aspect vary significantly over short distances. Therefore, optical satellite imagery in such areas is affected due to strong variations of the topographic parameters. It has a significant influence on the qualitative and quantitative

estimation of snow and other land cover characteristics. These variations of the topographic parameters affect the variations in the brightness on the satellite imageries of different spectral and spatial resolution. The topographic corrections or topographic normalization refers (Riano *et al.*, 2003) to the compensation of different solar illuminations due to the irregular shape of the terrain. Differential illumination causes a high variation in the reflectance response for similar snow and other land covers: shadow areas (north facing slopes) show less than expected radiance and reflectance, whereas effect is opposite (Riano *et al.*, 2003) in sunny areas (south facing slopes). Differential illumination effects in satellite imagery suppress the maximum information on the north facing slopes and have serious consequences for quantitative methods for snow applications including classification, temporal change analysis and other related hazard information. The direct solar irradiance on any inclined pixel is different as compared to flat surface on the satellite images. Therefore, effective removal or minimization of terrain effects is essential for snow applications e.g. corrected spectral reflectance (Xin *et al.*, 2002), estimation and mapping broad band albedo (Duguay and LeDrew, 1991; Song and Gao, 1999), spectral mixing (Romanov *et al.*, 2003; Haertel and Shimabukuro, 2005), energy balance and melt processes (Brun *et al.*, 1989; Duguay, 1993; Upadhyay, 1995; Mukkoth, 2004), automatic classification of avalanches in satellite or aerial imagery (Treichier *et al*. 2009), temporal and spectral changes (Davis *et al*., 1993) and spatial patterns of temperature (Deems, 2001) in mountainous area. A wide range of different commonly used previous methods have been reported in the literature. These can be divided in to three broad categories.

(i) Lambertian methods which assume that phenomena on the surface of the earth reflect incident radiations in all directions equally. The radiation of a Lambertian surface is given by (Smith et al., 1980).

$$(\lambda, e) = Ln(\lambda)cosi \qquad 2.5$$

where, L = radiance, λ = spectral wavelength, *e* = existence angle = slope,

Ln = radiance when i = e = 0, i = incident angle.

Various Lambartian methods are Cosine (Teillet, 1982), (Civco, 1989), Cosine-C (Teillet *et al.*, 1982), C-correction (Teillet et al., 1982), SCS (Gu *et al.*, 1998), SCS+C (Seonen, 2005), Smooth C (Raino *et al.*, 2003). To overcome the limitation of overcorrection in the conventional cosine correction method, Teillet *et al.*, (1982) developed

a semi-empirical method called c-correction method based on a modified variant of the cosine correction, by incorporating in its formulation a semi-empirical parameter 'c' derived from the satellite metadata. Meyer *et al*., (1993) noted that the incorporation of c in the formulation tends to significantly reduce the overcorrection of data that occurs especially towards the smaller cos i values (slopes facing away from the source of illumination), as compared to the traditional cosine correction approaches. Liang, (2004) modified the original Teillet *et al*., (1982) c-correction equation to its equivalent expression for at-sensor observed spectral radiance. Gu and Gillespie, (1998) observed that the widely used cosine correction and c-correction methods may not appropriately take into account the canopy contribution and hence they developed sun-canopy-sensor (SCS) correction method. Seonen *et al*., (2005) later combined the SCS correction and c-correction techniques (Meyer *et al*., 1993) into the so-called SCS + *c* correction method. To account for the atmospheric effects along with the topographic effects, Riano *et al*., (2003) proposed a variant of the c-correction method, which they called the smooth c-correction method. Generally these methods have been used for qualitative analysis and mapping of vegetation types and forest cover. In very few cases, some of these methods (Hall *et al*., 1988; Civco, 1989) have been used for snow applications but the results are not validated with in-situ observations.

(ii) Non-Lambartian methods: Non-Lamrartian model assumes that incident radiation is scattered according to the bidirectional reflection distribution function (BRDF) of illuminated phenomena (Estes, 1983) which is related to surface roughness (Smith *et al*., 1980). The BRDF can be described by Minnaert constant k, which was first applied by Minnaert (1941) in photometric analysis of lunar surfaces. Minneart's Method is very effective in slightly rugged terrain (Eyton, 1989; Colby, 1991). The effectiveness of utilizing the Minnaert constant in the topographic normalization process is a function of numerous variables, many of which have not been quantified (Colby *et al*., 1998). Ekstrand, (1996) have investigated the application of detailed a priori knowledge of site characteristics to correct for anisotropic reflectance utilizing the Minnaert constant. Many authors have attempted to develop reliable image processing methods for reducing topographic effects, without detailed a prior knowledge of surface feature reflectance values (Estes 1983; Colby, 1991; Hodgsen and Shelley, 1994; Colby, 1995 and Colby et al., 1998).

(iii) Empirical methods incorporate an empirically determined calibration coefficient C. Some of these methods are Teillet-regression, two stage normalization (Civco, 1989), Slope matching (Nichol *et al*. 2006) the later providing most satisfactory results in

terms of visual effect (Law, 2005).These methods have mostly been used for qualitative analysis of mapping vegetation types and forest cover. In few cases topographic methods (Dozier, 1984; Hall et al., 1988, Civco, 1989) were used for snow applications in Himalayan terrain but are reported to give erroneous results. Snow cover analysis using all models is not explored extensively for rugged and complex Himalayan terrain. A more detailed examination of the effect of topography for snow cover monitoring in Himalayan region is covered in chapter 4.

2.3 Models and methods for Satellite based snow cover mapping and monitoring

Satellite snow mapping has been accomplished since 1966, initially using data from the reflective part of the electromagnetic spectrum and later employing data from the microwave part of the spectrum. Visible and near-inferred sensors provide excellent spatial information from satellites for detailed snow cover mapping. Passive microwave data has been used for global mapping of snow cover on a daily basis. However, the data from the passive microwave satellites is on a very poor spatial resolution ranging from 12.5 km to 25 km. which limits their use on higher reaches which have very little vegetation. Dense forest cover limits the use of both the techniques. The microwave synthetic aperture radar (SAR) data has not been used on a global scale for snow cover monitoring specially in the North-West Himalayas. Due to seasonal and inter-annual variations in climate, areal and spatial distribution of snow cover varies significantly over time. Therefore, there is a need for monitoring the area and spatial distribution of snow cover from landscape to global scales. A number of problems exist in mapping snow cover from remotely sensed data. Hence, many image information extraction techniques have been developed to solve those problems and keeping view the increasing demands for improved areal extent of snow for various applications.

Different methods and models have been implemented for snow cover monitoring namely visible band reflectance (Kazama and Sawamoto, 1995, Asaoka *et al.*, 2002), Normalized Difference Snow Index (NDSI) (Hall *et al.*, 1995, Salomoson and Appel 2004, 2006, Kulkarni et al., 2002a) and other methods using sub-pixel classifications based on linear and iterative methods. Until recently snow cover mapping and monitoring was being carried out based on data acquired from satellite sensors such as NOAA AVHRR, LANDSAT MSS and TM, IRS LISS and WiFS etc. which unfortunately have become saturated for snow due to its high reflectance in most of their spectral regions. Moreover, the

mapping process was also largely based on the conventional techniques such as manual delineation of snow/glacier cover boundaries, segmentation of ratio images and hard or crisp classification algorithms such as Maximum Likelihood Classifier (MLC). However, the main assumption in using these methods is that the classes are discrete and mutually exclusive, and therefore each pixel is treated as pure consisting of one and only one class. With the improvement in technology, new sensors have been developed which are not saturated for snow. MODIS (Moderate Resolution Imaging Spectroradiometer) on-board Aqua and Terra satellites and AVHRR (Advance Very High Resolution Radiometer) on-board NOAA satellites and AWiFS on-board Indian Satellite 'Resourcesat' are not saturated for snow applications. Availability of data from these sensors has not only helped us in overcoming the saturation problem due to their high radiometric resolution but has also facilitated the effective monitoring of large snow covered areas as a result of high temporal resolution and wide swath coverage. However, the data provided from these sensors are at medium to moderate spatial resolution ranging from 56m of AWiFs to 250m, 500m and 1000 m of MODIS. Various methods for snow cover monitoring can be described in the following categories.

2.5.1 Manual delineation of snow cover

It is simply the on-screen digitization of the satellite images and is based on the visual interpretation of snow covered areas using a set of image interpretation elements namely tone, texture, shape, size, association, pattern and shadow applied individually or in combination. It has been widely used for mapping of glacial ice and snow extents (Kulkarni *et al*., 2007). It is an effective method, but is very tedious and time consuming and may not be appropriate for mapping at operational level.

2.5.2 Snow mapping using digital image classification

Digital image classification is perhaps the major image processing task for extracting useful information from remote sensing data. The aim is to produce thematic maps where each pixel in the image is assigned a class (e.g., snow) on the basis of its spectral response to produce a classification. There are two approaches to classify an image, namely supervised and unsupervised classification techniques (Jenssen, 1996). In a supervised classification the identity and location of some of the land cover types such as urban, agriculture or wetland, are known as a priori information through the combination of fieldwork, analysis of aerial

photography, maps etc. These require the intervention of analyst to locate training sites to train the classification algorithm for eventual land cover mapping of the remainder of image. Every pixel both within and outside these training sites is then evaluated and assigned to the class of which it has highest likelihood of being a member. On the other hand unsupervised classification involves categorization of digital image data by computer processing based solely on the image statistics without availability of training samples or a prior knowledge of the area. The classification creates natural groupings in the image values, called spectral clusters or classes. In this fashion, values with similar gray levels are assumed to belong to the same land cover type. The analyst then decides the identity of these spectral clusters.

There are several techniques of image classification, which are often categorised into per-pixel or hard classifiers and sub-pixel soft classification techniques.In per-pixel classification techniques, each pixel of remote sensing image is allocated to a single class. Hence, these techniques are based on the assumption that all the pixels in an image are pure. Wang and Li (2003) performed supervised classification of images from Landsat TM, Terra MODIS and NOAA-AVHRR to map three classes (old snow, fresh snow and firn) using minimum distance classifier and inter-compared with other snow and ice mapping techniques. An inventory of the entire Southern Patagonian Icefield (SPI) based on TM data of year 1986 was prepared by Aniya *et al*. (1996) using cluster analysis (ISODATA) with TM bands 1, 4 and 5 to produce three classes (snow, ice and rock). A parallelepiped classification was performed. A supervised MLC was applied to Landsat MSS and TM scenes by Gratton *et al*. (1990) to map seven classes. However, in that study, misclassification between clouds, shadows and water, particularly in debris covered glaciers, was observed due to which the maps had to be corrected manually. Blue-ice of different characters as well as snow of various degree of transformation was separated and possible to map using MLC. MLC was carried out on a TM image using principal components as input data (Bronge *et al*. 1999). However, misclassifications occurred for mixed pixels covered with clouds and shadows. The other per pixel techniques employed for the classification of snow are based on thresholding of ratio images and empirical indices.

2.3.3 Snow cover monitoring using Snow Indices

A method using visible band reflectance (mostly red) has traditionally been regarded as the most generic and simplest of techniques for identifying snow covered areas from remotely sensed data. The use of visible band is very effective for investigating large scale

distribution of snow covered areas. The accuracy of this method was improved by using a threshold of the existence of snow from ground data (Kazama and Sawamoto, 1995, Asaoka *et al*., 2002). However, in many studies, the calculated values depend on the properties of each sensor or the radiative conditions of each image since the calculations are based on DNs and nor reflectance. In order to remove some of the radiometric errors and random changes in scene irradiance due to atmospheric and topographical changes, the use of ratioing visible (VIS) and near-infrared (NIR) or shortwave Infrared (SWIR) is documented (Valovcin, 1976, 1978 and Kyle *et al*., 1978). Later, automated methods that relied on the VIS/'NIR ratio were refined substantially using satellite data, by Crane and Anderson (1984), Dozier (1989), and Rosenthal and Dozier (1996) for regional scales.

2.3.3.1 Normalized Difference Snow Index (NDSI)

NDSI has been very useful for the identification of snow and ice in the satellite imagery. Its popularity stems from the fact that it allows the differentiation of snow from clouds and other non-snow covered conditions. Furthermore NDSI is insensitive to a wide range of illumination conditions, is partially normalised for atmospheric effects and does not depend on reflectance in a single band. NDSI essentially takes advantage of the fact that snow reflectance is high in the visible wavelengths and has low reflectance in the shortwave infrared wavelengths (Nolin & Liang, 2000) to enable discrimination of snow and clouds since the reflectance of clouds is high in SWIR band. .

Originally proposed for snow mapping from Landsat (Hall *et al*., 1995) the NDSI is defined as the difference of reflectance observed in a visible band and a short-wave infrared band divided by the sum of these two reflectance values:

$$NDSI = \frac{R_{\text{vis}} - R_{\text{SWIR}}}{R_{\text{vis}} + R_{\text{SWIR}}} \qquad 2.6$$

where, R_{VIS} is the reflectance of the visible band (0.52-0.60 μm) and R_{SWIR} is the reflectance of the shortwave infrared band (1.55-1.75 μm). A specific threshold value for NDSI of 0.40 is defined to allow identification of snow covered areas from images produced by different sensors (Xiao *et al.*, 2001). In case of Terra MODIS band 4 (0.545-0.565 μm) and band 6 (1.628-1.652 μm) are used for NDSI calculations. In case Aqua MODIS a large number of detectors became nonfunctional and therefore band 7 (2.105-2.155 μm) was validated for use (Salomonson and Appel, 2006) in place of band 6. In the field of snow

cover monitoring, another problem exists involving the pixels consisting of both snow and vegetation as their spectral characteristics differ from each other. The identification of snow covered areas using NDSI, therefore, does not produce accurate results where snow covered areas are mixed with vegetation (Hall *et al.* 1998). In such cases it is necessary to change the threshold value by referring to the Normalized Difference Vegetation Index (NDVI). The NDVI normalizes between the near-infrared reflectance, where vegetation is bright, with visible reflectance, where vegetation is dark.

$$NDVI = \frac{R_{\text{NIR}} - R_{\text{VIS}}}{R_{\text{NIR}} + R_{\text{VIS}}} \qquad 2.7$$

To account for the influence of vegetation on the NDSI signal, (Klein *et al*., 1998) combined a snow reflectance model with a canopy reflectance model to identify snow covered forested area when NDSI is < 0.4 but NDVI is > 0.1. MODIS band 1 (0.620-0.670 μm) and band 2 (0.841-0.876 μm) are used to calculate NDVI (Hall *et al*., 1998). When snow and vegetation are mixed, the threshold value of NDSI is reduced to 0.10 (Klein *et al.* , 1998).

2.3.3.2 Normalized Difference Snow/Ice Index (NDSII)

This is a slightly improved version of the NDSI and was developed by Xiao *et al*., (2001). In this index the visible band has been changed from 'green' to more extensively used 'red' band as shown in the following equation

$$NDSII = \frac{R_{\text{red}} - R_{\text{SWIR}}}{R_{\text{red}} + R_{\text{SWIR}}} \qquad (2.8)$$

where, 'R_{red}' is the reflectance of visible (red) band and R_{SWIR} is the reflectance of shortwave infrared band. The empirically obtained threshold was also 0.40. Keshri *et al.* (2009) have indicated the potential of this is index for the ASTER data for discrimination of snow and ice as the spectral slopes for these are different between the green and near infrared bands.

2.3.3.3 Normalized difference glacier Index (NDGI)

This index has also been proposed based on the ASTER bands. It has been seen (Keshri *et al.* , 2009) that the spectral slope of snow/ice between green and red bands is different from that of ice mixed debris in the supraglacial terrain. Thus these bands can potentially help to distinguish these materials they have proposed NDGI

$$NDGI = \frac{R_{\text{green}} - R_{\text{red}}}{R_{\text{green}} + R_{\text{red}}} \quad (2.9)$$

2.3.3.4 S3 Index

This index was developed independently using ground measurements of spectral reflectance of miniature fir trees on snow (Saito and Yamazaki, 1999). S3 is defined as:

$$S3 = \frac{(NIR)R_{\text{red}} - R_{\text{SWIR}}}{(R_{\text{NIR}} + R_{\text{red}})(R_{\text{NIR}} + R_{\text{SWIR}})} \quad (2.10)$$

where, NIR, red and SWIR are the reflectance of the near near-infrared (0.78-0.90 μm), visible (red, 0.63-0.69 μm) and shortwave infrared bands. The S3 index was evaluated in one of the snowiest regions of Japan (Shimamura *et al*., 2006) and was found to improve the accuracy of identification of snow covered area under vegetation. This index was designed and developed for the Global imager (GLI) sensor of the Advanced Observing Satellite II (ADEOS II), which was launched in December 2002. Unfortunately it stopped working in October 2003 and hence only a few studies tested its ability to accurately identify snow covered areas (Motoya, 2003; Shimamura *et al*., 2006).

The efficacy of NDSI and S3 was evaluated by comparing the results of these indices with maps created by snow surveys which were exactly synchronized with the pass of Landsat-7 (Shimamura *et al*., 2006). They concluded that both NDSI and S3 can identify snow covered areas under vegetation. However, S3 can identify snow covered areas without any reference data, while NDSI needs vegetation data such as NDVI for identifying snow covered areas under denser vegetation. S3 can be regarded as a combination of both NDSI and NDVI.

2.3.4 Snow Cover Monitoring at Sub-pixel Level

When frequent mapping is required, which is the usual case during the snowmelt season, only the medium resolution sensors such as AWiFs and MODIS and coarse resolution sensors such as NOOA AVHRR are available. Classification of pixels into snow and no-snow may be sufficient for large scale applications, such as global snow-cover monitoring for environmental applications. However, for medium and small scale applications, like mapping catchments for hydropower production, or high-precision large scale mapping more exact

information about the actual snow coverage inside a pixel is needed (Solberg, 2000). Per-pixel classification techniques have limitations in classifying images dominated by mixed pixels. Mixed pixel is the one that do not represent one particular land cover class (e.g. snow cover) but contains two or more land cover classes in a single pixel area. A mixed pixel displays a composite spectral response that may be dissimilar to the spectral response of each of its component land cover classes. Therefore, pixel may not be allocated to any of its component land cover classes. Hence, error is likely to occur in the classification of image, thereby decreasing the classification accuracy of the image contaminated by mixed pixels. Sub-pixel classification overcomes this mixed pixel problem by predicting the proportional membership of each pixel to each class (Tiwari *et al*., 1999). The output of sub-pixel classification is not a single classified image but a number of images known as fraction images are obtained as classified outputs. Some sub-pixel classification techniques include maximum likelyhood classifier (MLC), linear mixture modeling (LMM) (Nolin *et al*., 1993; Rosenthal and dozier, 1996; Painter *et al*. 1998, 2003; Vikhamar and Solberg, 2002, 2003; Foppa *et al*., 2004), artificial neural network (ANN) (Foody and Arora, 1997; Gopal *et al*., 1996), decision tree classification (Friedl and Brodley, 1997; Ghose *et al*., 2010), object-based classification methods (Forster *et al.*,) etc. However, not all these techniques have yet been explored for snow-cover sub-pixel mapping (Foody and Arora, 1996, 1997; Tiwari *et al*., 1999; Arora, 1999). The literature suggests the use of empirical relationships (Kaufman *et al*., 2002, Barton, 2002; Salomonson and Appel, 2004, 2006), LMM (Nolin *et al*., 1993; Rosenthal and dozier, 1996; Painter *et al*., 2003; Foppa *et al*., 2004) Vikhamar and Solberg, 2002, 2003; Foppa *et al*. 2004) and ANN (Simpson and McIntire, 2001), for snow cover mapping at sub-pixel level. The application of these models has yet not been explored for Himalayan snow cover as complex topography influences the results and inability to map snow in mountain shadows.

Fuzzy Maximum Likelihood Classifier (MLC) is the most widely classification method in remote sensing applications. It is often treated as a benchmark to evaluate the performance of the new classifiers. In majority of the studies, MLC is used as a per-pixel classification technique that allocates the pixel to a class having the highest probability density. However, the output of a hard classifier may be softened to allow for the partial and multiple class membership for each pixel to be estimated. Thus, for example, the a-posterior probabilities from a MLC may reflect to some extent the land cover class (e.g. snow) composition mixed pixel (Wang, 1990 and Foody *et al*., 1992).

Linear Mixture Modelling (LMM) is widely used for decomposition of the class proportions of mixed pixels (Settle and Drake, 1993). The basic assumption of LMM is that the spectral response (DN value) of a mixed pixel is a linear sum of the component classes, weighted by their corresponding proportional area on ground. Thus, it calculates the proportion of each class. Rosenthal and Dozier (1996) estimated fractional snow cover from Landsat TM imagery using LMM for only a few representative regions and found that the technique was able to accurately identify surfaces without topographic correction. Vikhamar and Solberg (2002) implemented LMM for estimation of snow under forests in parts of South Norway using Landsat TM image, aerial photographs and *in situ* reflectance measurements. The main end-members included snow, bare-ground and tree classes. An operational form of this algorithm was later applied to two Terra MODIS images for mapping snow under forests with different snow conditions covering a forested area in southern Norway (Vikhamar and Solberg, 2003). Estimated snow-cover fractions were compared with snow-cover fraction reference maps derived from two Landsat Enhanced Thematic Mapper Plus (ETM+) images acquired on the same days as the MODIS images. The classification accuracy showed that 96% of the pixels were classified with less than 20% error for 7 May 2001 image whereas for the corresponding image of 4 May 2000, 88% of the pixels were classified with less than 20% error.

Recently, Sirguey *et al.*, (2009) have presented a method for production of snow cover maps with improved spatial resolution of 250 m, using MODIS data, at sub-pixel level in which a constrained LMM has been applied on radiometrically corrected MODIS images. The overall RMSE and mean absolute error (MAE) showed an improvement of 25% when the MODIS images with improved spatial resolution were used. It appears to be the most effective and widely used technique for sub-pixel mapping of snow cover, as can be seen from a number of studies (e.g., Rosenthal and Dozier, 1996; Vikhamar and Solberg, 2002; Vikhamar and Solberg, 2003; Sirguey *et al.*, 2009). However, the effectiveness of the technique has not yet been reported for Himalaya region.

For an operational snow-cover mapping algorithm, the two basic requirements of are that it should be computationally simple and fast. Keeping this in mind, techniques based on empirical relationships have been developed mainly for sensors which have been planned for operational snow-cover mapping. The empirical relationship based techniques of snow cover mapping establish a relationship between snow cover and some other property such as reflectance, NDSI etc. to calculate the percentage of snow cover in a pixel. (Anderson, 1982)

developed a fractional snow cover mapping algorithm for NOAA-AVHRR data based on an empirical 'reflectance to snow-cover' relationship. The model was developed by considering two points on the reflectance function: maximum reflectance for 0% snow cover and lower reflectance for 100% snow cover. (Barton *et al.* 2001) developed an algorithm by establishing a polynomial regression relationship between NDSI and snow cover fraction estimated using LMM for Landsat TM image of Sierra Nevada near Mono Lake, California. The algorithm was tested in other areas using Landsat TM data, and for North America using MODIS data. They concluded that the error is much less at low percentages of snow cover and higher in areas of greater percentages of snow cover. (Kaufman *et al*., 2002) devised an empirical technique for estimation of fractional snow cover based on the concept that reflectance of snow is dark at 2.1 μm and much brighter at 0.66 μm. A relationship between reflectance of non-snow cover areas (vegetation and soil) at 0.66 μm and 2.1 μm was used to predict the reflectance at 0.66 μm in absence of snow using the developed empirical relationship. The snow cover fractions estimated by them were compared with the snow cover fractions measured using LMM (Rosenthal and Dozier, 1996). Differences of only 1-2% were observed between the snow cover fractions estimated using the two techniques.

Salomonson and Appel (2004) conducted a study with the aim to evaluate the utility of NDSI in estimating the fractional snow cover within a 500 m MODIS pixel. The data from Landsat ETM+ scenes was acquired as ground truth. All the Landsat scenes were classified as snow or non-snow using the SNOWMAP algorithm of MODIS. An ordinary least squares regression approach was then applied to derive linear relationships between the snow fraction (FRA) and NDSI corresponding to the 500 m grid cells. Salomonson and Appel (2006) used Aqua MODIS data (except band 6) and deduced a similar relationship between fractional snow cover and NDSI (computed using band 7). They also refined the existing relationship for Terra MODIS using new criterion and found that the new criterion yielded improved results. Similar study for developing a statistical relationship for use in the Western Himalayan region has yet not been found reported.

2.4 Limitation of optical sensors for snow monitoring in forested areas

The optical sensors MODIS, Landsat TM and MSS, IRS LISS and AWiFS observe the projected snow covered areas. The tree canopies obscure the view of the ground, thus the projected view will miss snow beneath the trees. Some correction strategies have been validated (Rittger et *al*., 2012) over thickly forest covered areas by adding the vegetation

covered portion of the pixel to the snow cover. However the underlying assumption that the distribution of snow under trees is the same as the distribution in the gaps could not be tested with observation from optical sensors that cannot see through canopy. It was also found (Rittger *et al.,* 2012) that the Himalayan region had the greatest errors in snow cover mapping compared to North American regions which have been attributed to tougher topography and the larger solar zenith angles of the data used in the analysis. Furthermore the deeper and more prevalent shadows in Himalayas cause all methods to miss the snow under thick canopy.

2.5 Influence of topography on Change Detection Analysis in snow covered areas

Change detection is the identification and location of changes in the state of an object or phenomena through the examination of the changes in radiance values between sets of multi-temporal satellite images (Wang, 1993). Satellite based remote sensing technology has been successfully used in the past to accurately detect, monitor and display changes over large areas (Gong and Xu 2003). The basic premises of digital change detection are that changes in land cover result in changes in radiance values and that change in radiance values from land cover changes are large when compared to radiance changes caused by other factors (Mas, 1999). Ideally, change detection procedures should involve data acquired by the same sensor, having the same spatial resolution, viewing geometry, spectral bands, radiometric resolution, and acquired at the same time of day (Lillesand and Kiefer, 1999). It is also desirable to use anniversary date images in order to limit the differences associated with sun angle and seasonal variations.

A variety of change detection techniques are available for monitoring landuse/land cover changes. These techniques can be grouped into two main categories (Singh, 1989; Jensen, 1996; Coppin and Bauer, 1996; Ding *et al*., 1998; Johnson and Kasischke, 1998). These are (1) those based on spectral classification of the input data such as post-classification comparison (e.g., Mas, 1999) and direct two-date classification (e.g., Li and Yeh, 1998); and (2) those based on radiometric change between different acquisition dates, including (a) image algebra methods such as band differencing (Weismiller *et al.,* 1977), ratioing (Howarth and Wickware, 1981; Dale *et al*.,1996; Bruzzone,2000); write function memory insertion (Price *et al*.,1992; Jensen *et al*., 1993), and vegetation indices (Nelson, 1983); (b) regression analysis (Singh, 1986); (c) principal component analysis (Byrne *et al*., 1980; Gong, 1993) and (d) change-vector analysis comparison techniques and (CVA)

(Malila, 1980). Some hybrid approaches based on a mix of classification radiometric change information have been proposed (Colwell and Weber, 1981). It has also been seen that any change detection technique has its own set of advantages and disadvantages and no single approach can be considered optimal or applicable in all cases. In order to evolve a suitable change detection strategy a number of factors such as information requirements, spectral coverage, data availability and quality, image processing resources, analysis skill and experience, phenomenological knowledge, time and cost constraints and the importance of labelling the changes that are detected (Johnson and Kasischke, 1998). Among those radiometric change-based approaches, change-vector analysis is a useful method for land-use/land-cover change detection because it not only can avoid the shortcomings of those type (1) approaches, such as cumulative error in image classification of an individual date, but also it can find changed pixels using more, even all, the bands and provide "from-to" type of change information (Chen *et al.*, 2003).

Most of these methods have been used for environmental monitoring (Chavez 1994), agricultural surveys (Bruzzone and Serpico, 1997), urban studies (Merril and Jiajun, 1998) and forest monitoring (Hame *et al*.,. 1998), monitoring vegetation regeneration (Kristopher *et al*., 2005) etc. Very few studies have been reported on detection of changes in snow cover in the Himalayan region. Negi *et al*., 2005 has carried out qualitative changes using image algebra band difference method and applied post classification change detection along with change matrix for quantitative change analysis. Some authors have studied changes in the glacier extent. Most of these studies related to monitoring the glacier retreat in Himalayas (Bhutiyani 1999; Kulkarni et al. 2002b, 2005; Kulkarni 2007; Bhutiyani *et al*., 2008; Hasnain 2008; Bahuguna *et al*., 2007; Kumar *et al*., 2008; Nainwal *et al*., 2008). However, the investigations regarding the influence of topography on the change detection of snow cover in the Western Himalaya has not been reported.

CHAPTER 3

Study Area and Data used

Chapter 3

Study Area and Data Used

3.1 Study Area

The objective of this study is the 'Implementation and Performance Analysis of various techniques for snow cover monitoring in Western Himalaya. The Indian Himalaya stretches from east to west for about 2500 km across 72° E to 96° E longitude and 26°N to 37°N latitude as shown in Figure 3.1. Based on the climatic conditions and geographic distribution, Himalaya is broadly divided into three mountainous regions- Western Himalaya, Central Himalaya and Eastern Himalaya. The Western Himalaya region has been further delineated into three principal zones: Lower, Middle and Upper Himalaya (Sharma and Ganju, 2000) as shown in Figure 3.2. The snow covered areas located in Lower Zone are Pir Panjal ranges in Jammu and Kashmir and lower altitudes of Himachal Pradesh as shown in Figure 3. This zone is characterized by moderate temperature having mean minimum temperature -1.6^{0}C, the lowest minimum -120^{0}C and mean maximum 7.7^{0}C and has high

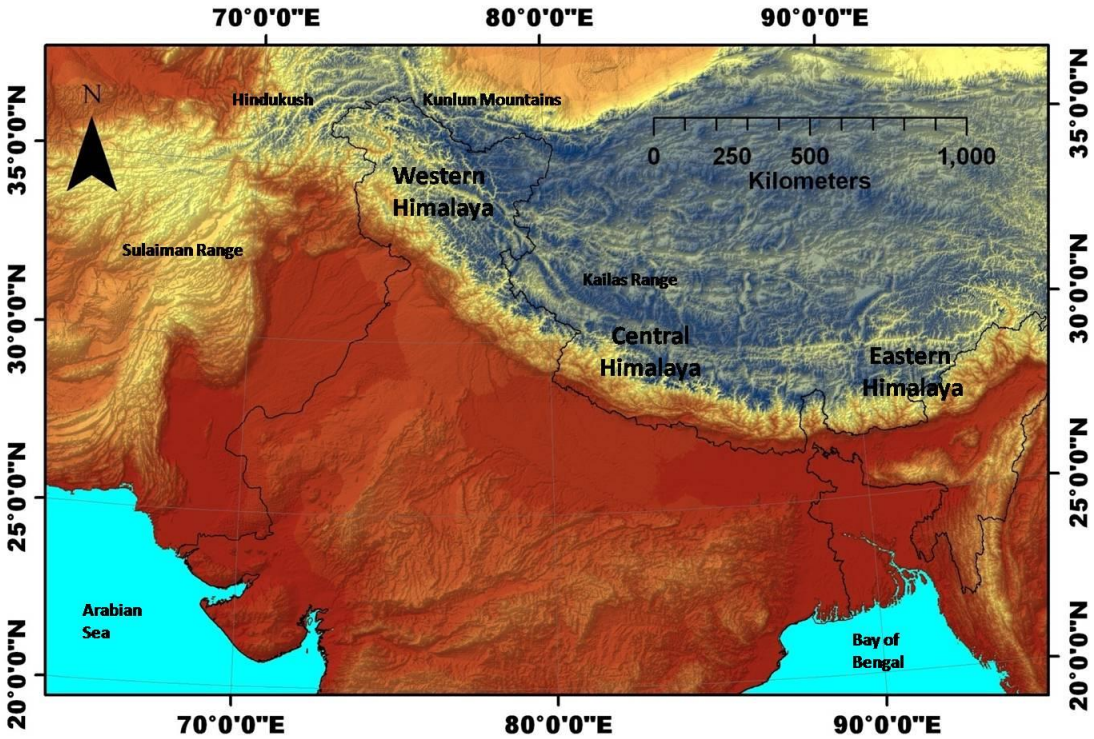

Figure 3.1 Layout of Broad Himalayan Regions(P P Karan)

precipitation with mean standing snow 165 cm and mean cumulative snowfall 363 cm in the month of January (Singh and Gangu, 2006). Due to moderate temperatures, the winter remains short and the snow cover changes into 0^0C isothermal. The average altitude of this zone is between 2000m and 4000m. The Middle Zone includes Great Himalayan range in Jammu and Kashmir and Pir Panjal range in Himachal Pradesh. This zone is characterized by cold temperature and mostly glaciated. It receives dry snow between December and end of January. The general rise in temperature from mid February onwards moistens fresh snowfall, and after March, the fresh snowfall is often accompanied with wet snowfall or light rain. Altitude of this zone varies from 3500m to 5300m. The Upper Himalayan zone mainly comprise of Zanskar range and Karakoram range. This zone is extremely cold, receives dry snow and is highly glaciated.

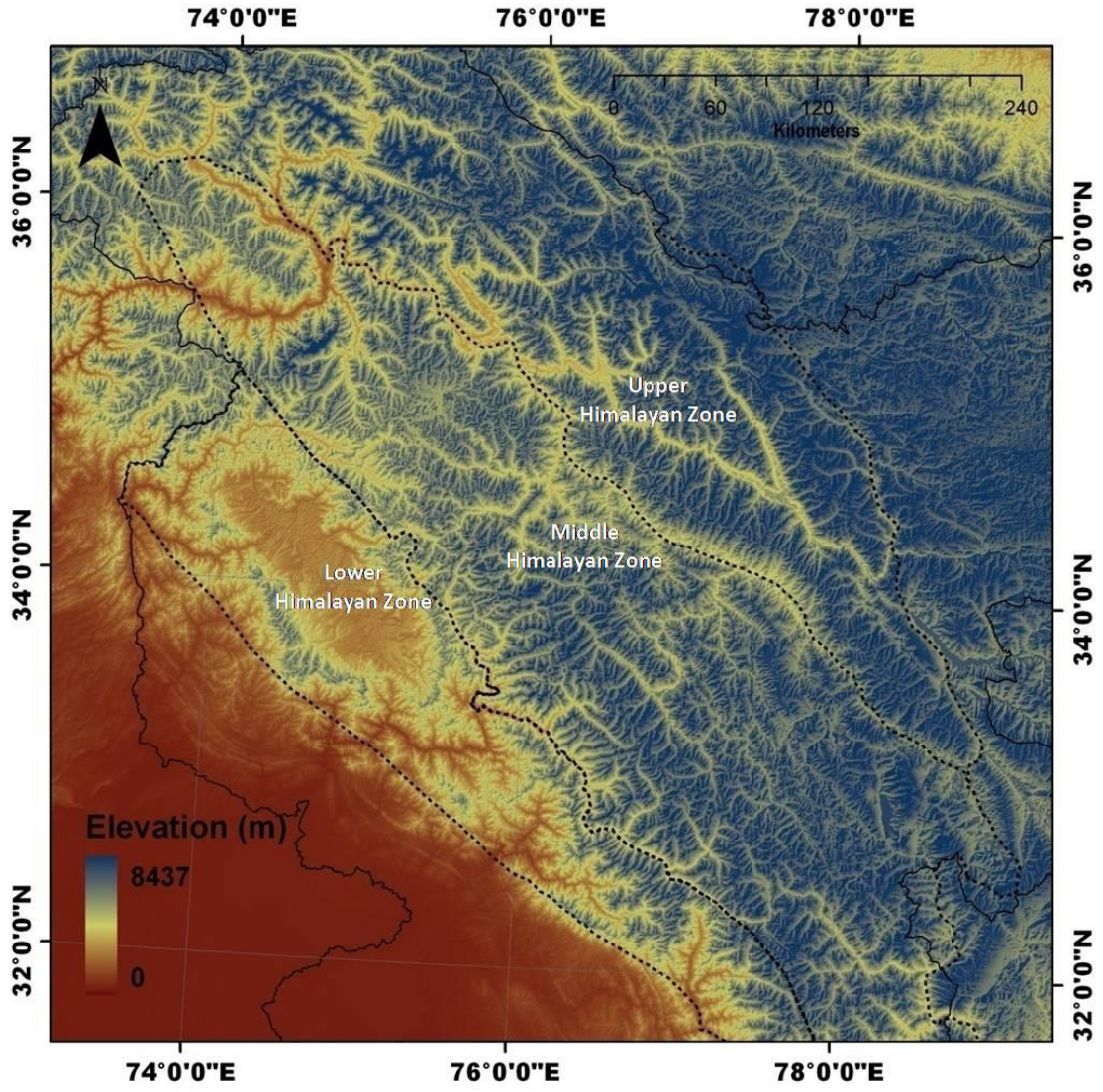

Figure 3.2 Various climate zone of western Himalaya (Sharma and Ganju,2000)

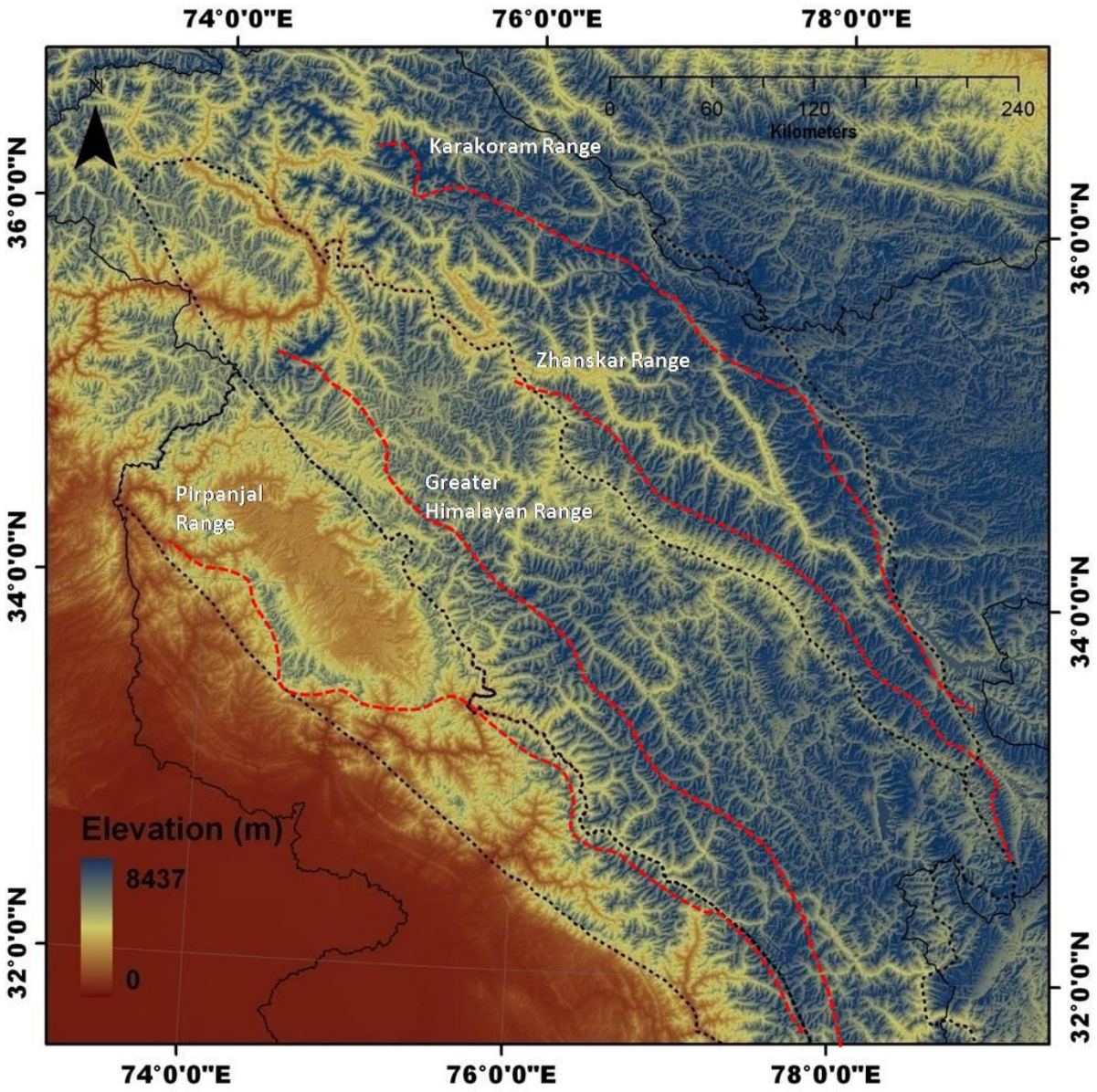

Figure 3.3 Mountain ranges of Western Himalaya (Sharma and Ganju,2000)

The climatic conditions are somewhat close to continental snow conditions. The altitude of this zone is more than 5000m.

3.2. Criterion for Selection of Satellite images

The main criteria formulated for selection of satellite images from the study area keeping in view the rugged Himalaya Terrain are as follows:

(a) Snow studies should be carried out on images of Early Winter (Nov-Dec), Late Winter (Feb-Mar), Early Summer (April-May) and Late Summer

(Aug-Sept). Early winter image helps the analysis of the snow characteristics of first snowfall. In late winter images, most of the areas are covered by snow. The

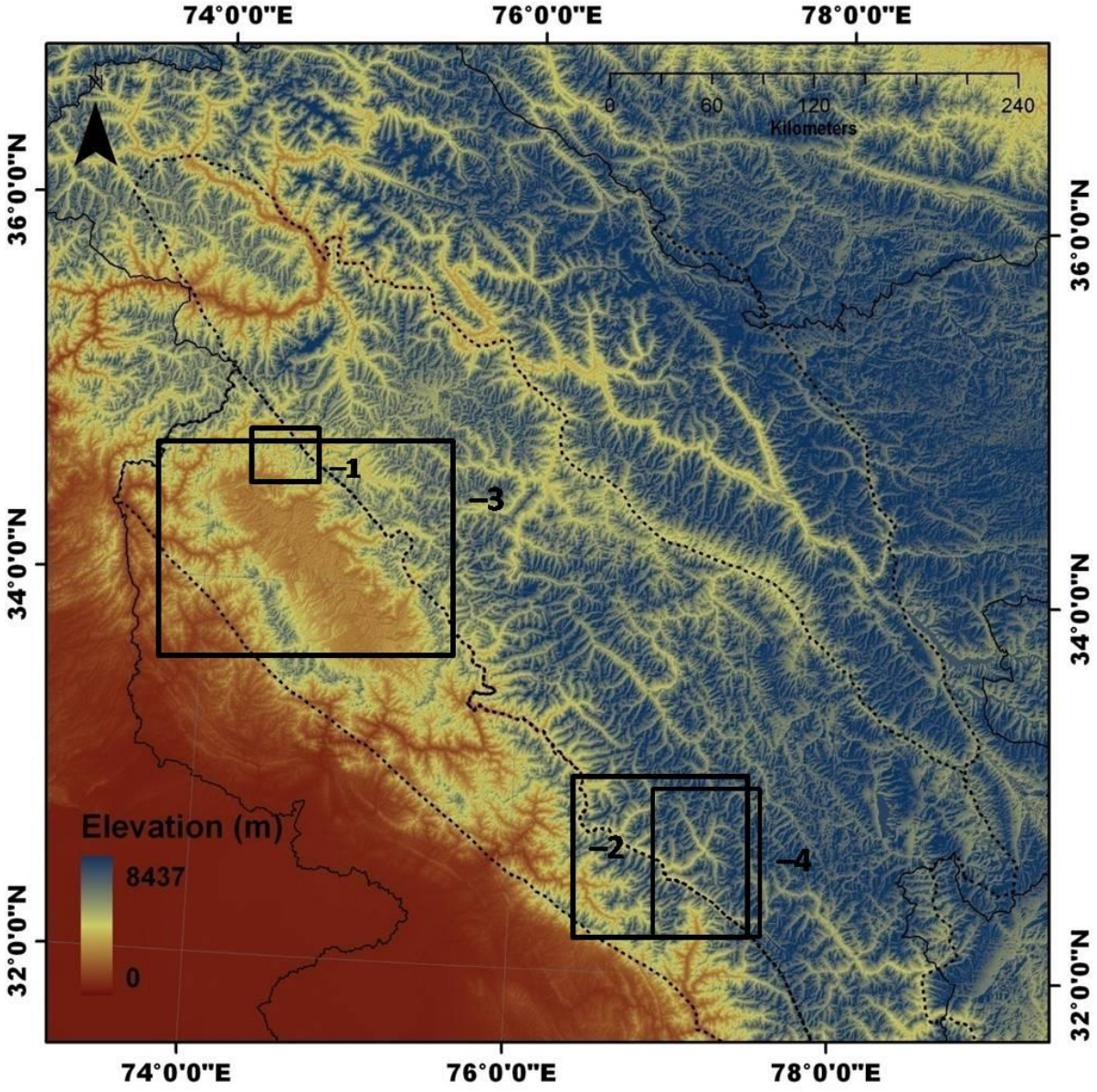

Figure 3.4 Study area pertaining to different published paper shown by rectangles. Numerical digits shows paper number in chronological order and respective study area

images of this season give the overall extent of snow and the change in the behavior of snow characteristics in broad scale. The different types of snow can be classified to carry out change detection in details for various applications, like avalanche forecasting and hydropower generation and water management.

(b) Image should be cloud free for better and accurate analysis. Even a thin layer of cloud can alter spectral signatures in satellite images enough to create the false impression of spectral change between two dates. Although zero percent cloud cover is preferred for satellite imagery but it is rarely available in the Himalaya especially in the time frame mentioned above. The clouds not only obscure terrain, but the cloud shadow also causes major image classification problems. Any area obscured by clouds or cloud shadow filters through the entire change detection process, severely limiting the utility of the overall image. Therefore the images having cloud cover more that 15%-20% have been avoided.

(c) The images should have been acquired at low solar elevation for proper analysis of the impact of topography.

(d) The field observation data pertaining to the selected imagery should be available for validation with satellite-estimated spectral reflectance in AWiFS and MODIS spectral bands after the application of different topographic corrections. Snow and Avalanche Study Establishment (SASE) have established a large network of observatories in the western Himalaya. In addition Scientists from SASE collect the field data from selective locations in the Himalayan region for validation of various snow and avalanche studies.

In this work, a number of cloud free images were selected for achieving different objectives for the period spanning from the year 2005 to 2009 both from AWiFS and MODIS data available in the SASE archives keeping in view the availability of field observations.

3.3 Data Used

3.3.1 Digital data

The other major considerations in the selection of satellite sensor for the snow cover studies is to have a judicious compromise in the four types of satellite image related resolutions required for analysis. The AWiFS (IRS P6) and MODIS (Terra and Aqua) satellite sensors are considered suitable for regular monitoring of snow cover due to their high radiometric resolution, greater swath, higher revisit period and medium spatial resolution. The spatial resolution of AWiFS is 56m compared to 250 to 500m of MODIS in the spectral bands of interest. However, the MODIS sensor imagery is available almost on daily basis compared to AWiFS 5 day repeat cycle. The radiometric resolution of both the sensors is such that they do

not saturate over snow. The features of AWiFS and MODIS sensors are given at Table 3.1 and 3.2 respectively.

3.3.2 Ground Data and Field Observations

Snow and avalanche Study Establishment has a large network of observatories in the western Himalayan region. The SASEs scientists also regularly visit these observatories for the collection of ground data for use in snow avalanche studies. The ground data required for validation purposes has been taken from the archives. Efforts have been made to select those dates on which the ground and satellite data is

Table 3.1 Salient specification of AWiFS Sensor

Spectral Bands (nm)	Spatial Resolution At Nadir (m)	Quantiz -ation (bit)	Minimum Radiance (mW cm^{-2} Sr^{-1} μm^{-1})	Maximum Radiance (mW cm^{-2} Sr^{-1} μm^{-1})	Mean Solar Exo-atmospheric Spectral Irradiance (mW cm^{-2} μm^{-1})
B2 (520-590)	56	10	0	52.34	185.3218
B3 (620-680)	56	10	0	40.75	158.042
B4 (770-860)	56	10	0	28.425	108.357
B5 (1550-1700)	56	10	0	4.645	23.786

available. The spectral reflectance was collected using a portable field spectroradiometer, Field Spec Pro FR Model 1999 acquired from Analytical Spectral Devices. It operates in the wavelength range 350 to 2500 nm. Inside the instrument, the light is projected from the fiber optics on to a holographic diffraction grating where the wavelength components are separated and reflected for independent measurements by detectors. Each detector converts incident photons into electrons and the photoelectric current for each detector is converted to a voltage and digitized

Table 3.2 Salient specifications of MODIS sensor

Spectral Bands (nm)	Spatial Resolution At Nadir (m)	Quantiz-ation (bit)	Radiance_Scale ($W\ m^{-2}\ Sr^{-1}\ \mu m^{-1}$)	Radiance_Offset	Mean Solar Exo-atmospheric Spectral Irradiance ($W\ m^{-2}\ \mu m^{-1}$)
B3 (459-479)	500	16	0.0208077	0	2090.71
B4 (545-565)	500	16	0.0182441	0	1863.97
B5 (1230-1250)	500	16	0.00525777	0	475.6
B6 (1628-1652)	500	16	0.00254259	0	237.66
B7 (2105-2155)	500	16	0.000777289	0	86.41

Table 3.3 Specifications of ASD FR Field Spec Spectroradiometer (www.asdi.com)

Parameter	Value
Spectral Range	350-2500nm
Spectral resolution	3nm (350<=λ<=1000nm) 10nm (1000<=λ<=2500nm)
Spectrum sampling rate	10 Spectra/S
Spectrum recording rate	1 Spectrum/S (max rate)
Weight	9.2 Kg
Optic cable length	2.5 m
Fiber optics	$1^0.3^0,8^0,25^0$
Noise equivalent change in reflectance (NEΔL)	3.7×10^{-10} $W/cm^2/nm/sr$@700nm

by a 16 bit A/D converter. The digital data is then transferred directly to controlling computer. The ASD-FR has a 512 element Silicon photodiode array to cover the wavelength range 350-1000 nm, and two separate thermo-electrically cooled, graded index In-GaAs photodiodes to cover the wavelength range 1000-2500nm. The specifications for the ASD-FR spectroradiometer are given in table 3.3. The instrument has high spectral resolution (3-10nm) and the rapid spectrum acquisition (10 spectra/s and an average spectrum automatically recorded at 1 Hz)

CHAPTER 4

Influence of topography on snow spectral characteristics

Chapter 4

Evaluation of influence of topography on snow spectral characteristics in Western Himalayan region using various techniques

4.1 Effect of Topography

The topographic effects caused due to terrain illuminations in optical satellite imagery have serious consequences for qualitative and quantitative analysis for snow applications, including classification and physical parameters. The relief effect due to topography is neither eliminated during system corrections nor during the normal geometric correction and has great significance in mountainous region. Therefore, effective removal or minimization of topographic effects is necessary for satellite image applications in mountainous region. Different methods for topographic corrections reported (Riano *et al*., 2003; Nichol *et al*., 2006) have been assessed in the context of snow reflectance, such as (i) C-correction (ii) Minneart corrections (including slope) (iii) two stage normalization and (iv) slope matching method. However, these methods have not been explored extensively for snow cover applications in Himalayan terrain. Most research was focused exclusively on vegetation analysis (Riano *et al.*, 2003; Nichol *et al.*, 2006). All the satellite imageries of AWiFS (Advance Wide Field Sensor on Resourcesat-I) and MODIS (Moderate Resolution Imaging Spectroradiometer on Terra) of different regions of Himalaya are geometrically and atmospherically corrected first before computation of spectral reflectance. In this chapter, we have performed an extensive comparative analysis of different topographic normalization methods for snow cover applications in rugged Himalayan terrain. The main objectives in the present chapter are (i) Qualitative performance analysis (ii) Quantitative analysis of snow reflectance after topographic corrections (iii) Validation of the spectral reflectance with in-situ observations and (iv) graphical analysis in order to explore best suitable model for Himalaya. Image based atmospheric corrections (Chavez, 1989; Song *et al.*, 2001) for path radiance and Rayleigh scattering is performed first using combination of DOS1 and DOS3 (dark Object Subtraction Model) for initial estimation of spectral reflectance without considering topographic influences.

4.2 Topographically uncorrected surface reflectance

Raw digital number (DN) derived from satellite optical systems cannot confidently be used for geophysical measurements and multi-temporal studies, since they include effects derived from sensor calibration, as well as atmospheric and topographic interferences (Riano *et al*., 2003). The conversion of digital numbers (DN) to radiance values can be obtained using calibration values provided with satellite data in image header file and it requires only compensating for atmospheric and topographic corrections (Riano *et al*., 2003). First of all, image based atmospherically corrected true spectral reflectance on the tilted surface, $R_{\lambda T}$, from sensor radiance, $L_{sat\lambda,}$ is obtained using the following model (Song *et al*., 2001**,** Pandya *et al* 2002).

$$R_\lambda = \frac{\pi\left(L_{sat\lambda} - L_p\right) d^2}{t_v\left(E_0 \cos\theta_z\, t_z + E_d\right)} \quad 4.1$$

Where L_p is the path radiance, d is the earth sun distance in astronomical units and calculated using the approach of Van (1996). E_0 is bandpass exoatmospheric spectral irradiance, E_d is downwelling spectral irradiance at the surface due to scattered solar flux in the atmosphere, θ_z is the solar zenith angle and calculated (Kasten, 1962) for each pixel of the study area, t_v is atmospheric transmittance along the path from ground surface to sensor and t_z is atmospheric transmittance along the path from sun to ground.

4.2.1 Image based atmospheric corrections

The atmospheric correction (path radiance) is an important step in the process of land surface reflectance. Therefore, image based atmospheric correction was carried out first, otherwise spectral radiances and reflectance of snow are overestimated in certain areas. The combinations of dark object subtraction models (DOS1 and DOS3) are used for atmospheric corrections (Song *et al*., 2001). Since the AWiFS and MODIS bands used in the present work lie in visible, near infrared and short wave infrared wavelength regions, DOS1 model assumes no atmospheric transmittance loss and no diffuse downward radiation at the surface (Chavez, 1989). DOS3 computes upwelling and downwelling radiation transmittance of atmosphere to correct the image for path radiance resulted from the interaction of the electromagnetic radiance with the atmospheric components (molecules and aerosols) as shown in Table 4.1.

Table 4.1: Parameter settings for the DOS approaches

Methods	t_v (atmospheric transmittance from ground to sensor)	t_z (atmospheric transmittance from sun to ground)	E_d (downwelling diffused irradiance)
DOS 1	1.0	1.0	0.0
DOS3	$\exp(-\tau_v/\cos\theta_v)$	$\exp(-\tau_z/\cos\theta_z)$	Rayleigh (6S)

The model assumes Rayleigh scattering only, that is, no aerosols. The optical thickness for Rayleigh scattering, τ_r, which is generally quite stable, depends mainly on the surface elevation and pressure and is estimated by using the following equation (Russell *et al*., 1993).

$$\tau_r = P/P_0[0.00864+6.5x10^{-6}Z]\ \lambda^{-(3.916+0.074\lambda+(0.005/\lambda))} \qquad 4.2$$

Where P_0 is standard atmospheric pressure and P is pressure in study area which is used from SASE field observatory in mountainous regions. Z is height in Km above sea level and used from digital elevation model (DEM) and λ is central wavelength of AWiFS and MODIS spectral bands. The upwelling (t_v) and downwelling (t_z) transmissivity are calculated using the equations given in the Table 4.1. The estimated values of transmittance (upwelling and downwelling) using Rayleigh scattering for AWiFS and MODIS spectral band are given in the Table 4.2. Due to atmospheric scattering effects, the dark object (shadow, deep clean water) is not absolutely dark (Chavez 1988) assuming 1% surface reflectance for the dark objects, the path radiance, L_p, is estimated using the proposed model (Chavez, 1989, 1996; Moran *et al*., 1992) and corrected for spectral radiance of AWiFS and MODIS images.

$$L_p = L_{min} - 0.01[E_0\cos\theta_z\, t_z + E_d]t_v/\pi \qquad 4.3$$

where L_{min} is the minimum radiance in different spectral bands of AWiFS and MODIS.

4.2.2 Effect of topography on snow reflectance

The operational use of remote sensing techniques is often obstructed by problems originating from topographic effects on the sensor response. The topographic effects on satellite imagery generally refer to the influence from the apparent intensity of surface reflectivity, which is

caused by the solar incidence, terrain slope and viewing angle. Such influences may be augmented when the terrain slope is steeper, especially for

Table 4.2: Atmospheric transmissivity in different spectral bands of AWiFS and MODIS

AWiFS Bands (nm)	Upwelling atmospheric transmissivity t_v	Downwelling atmospheric transmissivity t_z	MODIS Bands (nm)	Upwelling atmospheric transmissivity t_v	Downwelling atmospheric transmissivity t_z
B2 (520-590)	0.935	0.911	B3 (459-479)	0.879	0.822
B3 (620-680)	0.965	0.952	B4 (545-565)	0.937	0.906
B4 (770-860)	0.986	0.980	B5 (1230-1250)	0.997	0.996
B5 (1550-1700)	0.999	0.998	B6 (1628-1652)	0.999	0.998
			B7 (2105-2155)	0.999	0.999

mountainous regions. Due to atmospheric scattering, the sun elevation is also of importance. A surface perpendicular to the sun at a low sun elevation will receive less radiation than a surface perpendicular to the sun at a high solar elevation (Ekstrand, 1996). In other words, sun-facing illuminated slopes (south aspect) show slightly more reflectance value, whereas the effect is opposite in shaded area (north aspect) which show less reflectance values (Raino *et al.*, 2003). These differential illumination effects in satellite imagery will suppress the maximum information on the north-facing slopes, thereby adversely affecting the results of various quantitative methods of snow cover monitoring namely classification, temporal change analysis and other hazard related techniques. The direct solar irradiance on any inclined pixel will be different as compared to flat surface in the satellite images. Differential illumination results in considerable variation in the spectral characteristics of similar snow and other land covers. Therefore, different topographic correction methods are evaluated in Himalayan context to eliminate or at least reduce the terrain influence. In this thesis work, some of the widely used topographic correction methods as explained below have been implemented on snow cover areas in Himalayan terrain.

4.3 Topographic correction models

4.3.1 Cosine correction

This is most widely used method which is based on trigonometric approach and assumes Lambertian reflectance of the earth objects including snow, i.e. a perfect diffuse reflector having same reflectance in all viewing directions (Law and Nichol 2004). Lambertian correction function attempts to correct only for differential illumination caused due to orientation of the surfaces with respect to solar geometry (Law and Nichol, 2004). The cosine method for the Lambertian assumption (Teillet *et al*., 1982, Dozier 1984) which was later modified by Civco (1989) is given as:

$$R_{\lambda H} = R_{\lambda T} (\cos \theta_z / \cos i) \quad (4.4)$$

Where $R_{\lambda H}$ is the spectral reflectance for horizontal surface, $R_{\lambda T}$ is spectral reflectance observed over the inclined terrain; cos i is illumination (IL) and calculated using equation proposed by (Civco, 1989, Kawata *et al.*, 1995**,** Riano *et al*., 2003):

$$IL = \cos i = \cos (\theta_p) \cos(\theta_z) + \sin(\theta_p) \sin(\theta_z) \cos(\Phi_a - \Phi_0) \quad (4.5)$$

Where i is local incidence angle and can be defined as the angle between the direct solar rays and normal to the surface, θ_p is slope of the surface, Φ_a and Φ_0 are aspect of the surface and solar azimuth angles respectively.

4.3.2 C-correction

This correction is based on non-Lambertian assumption of the surface with modification of cosine correction developed by Teillet *et al*. (1982). A quantity, c_k, is introduced into the above equation (4.4) defined as:

$$R_{\lambda H} = R_{\lambda T} (\cos \theta_z + c_k / \cos i + c_k) \quad (4.6)$$

Where $c_k = b_k/m_k$, for $R_{\lambda T} = b_k + m_k \cos i$. Therefore, it is based on the empirical-statistical approach. The parameter c_k in band, k, is the quotient between the gradient (b_k) and intercept (m_k) of the regression equation, $R_{\lambda T}$ versus cos i.

4.3.3 Minneart correction

The Lambertian assumption is very convenient to simplify procedures but is unrealistic, since most of the land covers are rugged in mountain terrain, having a non-Lambertian behavior (Riano *et al*., 2003). For semi-Lambertian surfaces, the main methods are based on the ideas of Minneart (1941), who first proposed a semi-empirical equation to assess the roughness of the moon's surface (Riano *et al*., 2003). The function has been used for photometric analysis of lunar surfaces (Holben and Justice, 1980) and implemented for topographic corrections as given below:

$$R_{\lambda H} = R_{\lambda T} (\cos \theta_z / \cos i)^{k(\lambda)} \quad (4.7)$$

where, k(λ) is Minneart constant and depends on the type of surface and spectral wavelength bands. It varies from 0 (ideally non-Lambertian surface) to 1 (perfect Lambertian surface). The value of k (λ) can be determined by linearizing the equation (4.7), which then becomes as:

$$\ln(R_{\lambda T}) = \ln(R_{\lambda H}) + k(\lambda) * \ln(\cos i/\cos \theta_z) \quad (4.8)$$

The equation (4.7) was further modified by some author's Colby (1991) to include the slope of the terrain as follows:

$$R_{\lambda H} = R_{\lambda T} \cos \theta_p (\cos \theta_z / \cos i \cos \theta_p)^{k(\lambda} \quad (4.9)$$

4.3.4 Single and two-stage normalization (mean illumination method)

Several authors have reported (Holben and justice, 1980; Duguay and Ledrew, 1992; Meyer *et al*., 1993) that cosine correction in equation (4.4) overcorrects the image, mainly in areas of low IL because cos I <=0. Initially, an improved version of equation (4.4) was proposed by Civco (1989). The model is wavelength dependent which considers the mean IL conditions and single stage normalization. The image reflectance values are normalized using the illumination model. The illumination values ranging from -1 to +1 are scaled to range of 0-255 (Nichol *et al*., 2006) and then single stage normalization is computed using equation (4.10) as:

$$R_{n\lambda ij} = R_{\lambda ij} + \frac{[R_{\lambda ij} (<\cos i> - \cos_{ij} i)]}{<\cos i>} \quad (4.10)$$

Where $R_{n\lambda ij}$ is the normalized reflectance value for image pixel ij in band λ; $R_{\lambda ij} = R_{\lambda T}$ is the uncorrected original reflectance on the tilted surface for image pixel ij in band λ; <cosi> is the mean value of scaled (0-255) IL of the entire image and cos_{ij} i is IL image for each pixel ij of the study area. It is reported by Nichol *et al.*, (2006) that Civco (1989) observed that the first stage normalization maintains the mean spectral response of the image data while reducing the variance; he noted that the topographic effect was not completely removed and shady slopes remained dark relative to sun facing slopes.

The remaining topographic effect was further removed from the satellite images in second stage normalization by introducing an empirically determined calibration coefficient, C. The coefficient C is computed from the results of the single stage correction. Spectral response from the all the samples on the slopes facing to and away from the sun are obtained by using satellite images (Nichol *et al.*, 2006). The correction coefficient is than determined using equation (4.11).

$$C_\lambda = [(\mu_\lambda - N_\lambda)/((\mu_\lambda - N_\lambda) - (\mu_\lambda - N'_\lambda))] + [(\mu_\lambda - S_\lambda)/((\mu_\lambda - S_\lambda) - (\mu_\lambda - S'_\lambda))] \quad (4.11)$$

where C_λ is the correction coefficient for band λ, μ_λ is mean original uncorrected reflectance of the entire image in different spectral bands λ, N_λ is the mean reflectance value on the slopes facing away from the sun (north aspect) in uncorrected image data, N_λ' is mean reflectance values on the slopes facing away from the sun after first stage normalization. S_λ is mean reflectance value on slopes facing to the sun (south aspect) in uncorrected image data and S_λ' is mean reflectance value on slopes facing the sun after single stage normalization.

The second stage normalization correction is then applied for the uncorrected original reflectance image using the following equation.

$$R_{n\lambda ij} = R_{\lambda ij} + \frac{[R_{\lambda ij} (<cosi> - cos_{ij}i)] \times C_\lambda}{<cosi>} \quad (4.12)$$

4.3.5 Slope matching technique

Nichol *et al.* (2006) observed that the equation (4.12) developed by Civco (1989) is inadequate for topographic corrections on the satellite images due to two reasons (i) it does not equalize the reflectance or radiances values between the south aspect (sun facing slopes)

and north aspect (shady slopes) and normalize the image with respect to overall mean illumination of an entire image and (ii) coefficient C_λ, does not determine the difference between south and north aspect because north aspect is not normalized with respect to main cover type of the south aspect. Nichol *et al.*, (2006) modified the equation (4.12) and suggested that it is more important to make the extent of corrections equal to the range of reflectance values ($R_{max} - R_{min}$) i.e. maximum difference between south and north aspect. Considering mean IL (<cosi>) of an entire image in equation (4.12) does not retrieve the information under mountain shadow. He normalizes the DN values to the maximum illumination levels of pixels on the south aspect as compared to mean IL values of an entire image. The analysis of Nichol *et al*., (2006) slope matching technique is for vegetation analysis only and implemented for very high resolution satellite images of IKONOS acquired for low sun elevation angle of 38-42 degrees. The application of this new method is not explored for medium and coarse resolution satellite data. The new slope matching method is necessary to be implemented and tested for medium resolution AWiFS images (56m spatial resolution) and moderate resolution MODIS (500 m spatial resolution) imagery of Himalaya for snow cover applications for varying solar elevation angles, solar azimuth and illumination. DN (0-255) image is used as an input in the reported slope matching method. We have considered reflectance image as an input in slope matching method because the same DN values on different AWiFS and MODIS scenes are likely to correspond to different reflectance (Hall *et al*., 1995). It is important to express the data in physical units, for example reflectance. The image normalization is also performed in two stages. The first stage of the two stage normalization by slope matching technique is adapted as follows:

The required equation for the first stage normalization is given as:

$$R_{n\lambda ij} = R_{\lambda ij} + (R_{max} - R_{min}) \times \frac{(\langle cosi \rangle_s - cos_{ij}i)}{\langle cosi \rangle_s} \qquad (4.13)$$

where notation is same as in equation (4.10) except that $\langle cosi \rangle_s$ is the mean value of the scaled illumination model for the sun facing slopes rather than the overall mean of an entire image. R_{max} and R_{min} is the maximum and minimum reflectance values of the land cover in uncorrected image. Therefore, the advantage of this method is that reflectance values are normalized to the illumination level of pixels on the sunny slopes rather than the mean illumination value of the entire image.

The correction coefficient C_λ, in this new method is also different from that of Civco (1989) adapted equation (4.12). C_λ in different wavelength band λ, is determined using the difference of reflectance values between sunlit and shady slopes with the uncorrected and first stage normalized image using the following equation :

$$C_\lambda = \frac{S_\lambda' - N_\lambda}{N_\lambda' - N_\lambda} \qquad (4.14)$$

Where S_λ' is mean reflectance value on sunlit slopes after first stage normalization, N_λ is mean reflectance value on shady slopes in uncorrected image, N_λ' is mean reflectance value on shady slope after first stage normalization

The resultant equation by slope matching method for topographic corrections can be expressed as:

$$R_{n\lambda ij} = R_{\lambda ij} + (R_{max} - R_{min}) \times \frac{[(\langle cosi \rangle_s - cos_{ij}i)] \times C_\lambda}{\langle cosi \rangle_s} \qquad (4.15)$$

4.4 Methodology adopted for application of topographic Models in Himalayan terrain

The flow chart of detailed methodology showing various processing steps are given in the Figure 4.1.

4.4.1 Study area and satellite dataset

Three different study areas are considered in the present work, (i) located between 34.6124 degree N latitude to 34.7593 degree N latitude and 74.3474 degree E longitude to 74.6250 degree E longitude in North - East tip of Samsabari range in Jammu and Kashmir (J&K) region of Western Himalaya as shown in the Figure 4.2(a). The maximum elevation is 4101 m with an average value of 3090 m. The slope of an area varies from 0.17 degree to 69 degree with an average value of 27 degrees (ii) Second study area is located between 32.2607 degree N latitude to 32.7734 degree N latitude and 77.0174 degree E longitude to 77.4829 degree E longitude and is part of Beas basin in Kullu district of Himachal Pradesh (HP) as shown in the Figure 4.2(b). The maximum altitude varies from 1900 m to 6500 m with an average elevation of 4570 m. The average slope of this area is about 30 degree. (iii) The third study area (Figure 4.2 c) is quite large and covers different Himalayan ranges namely Pir-panjal, Samsabari and Greater Himalayan

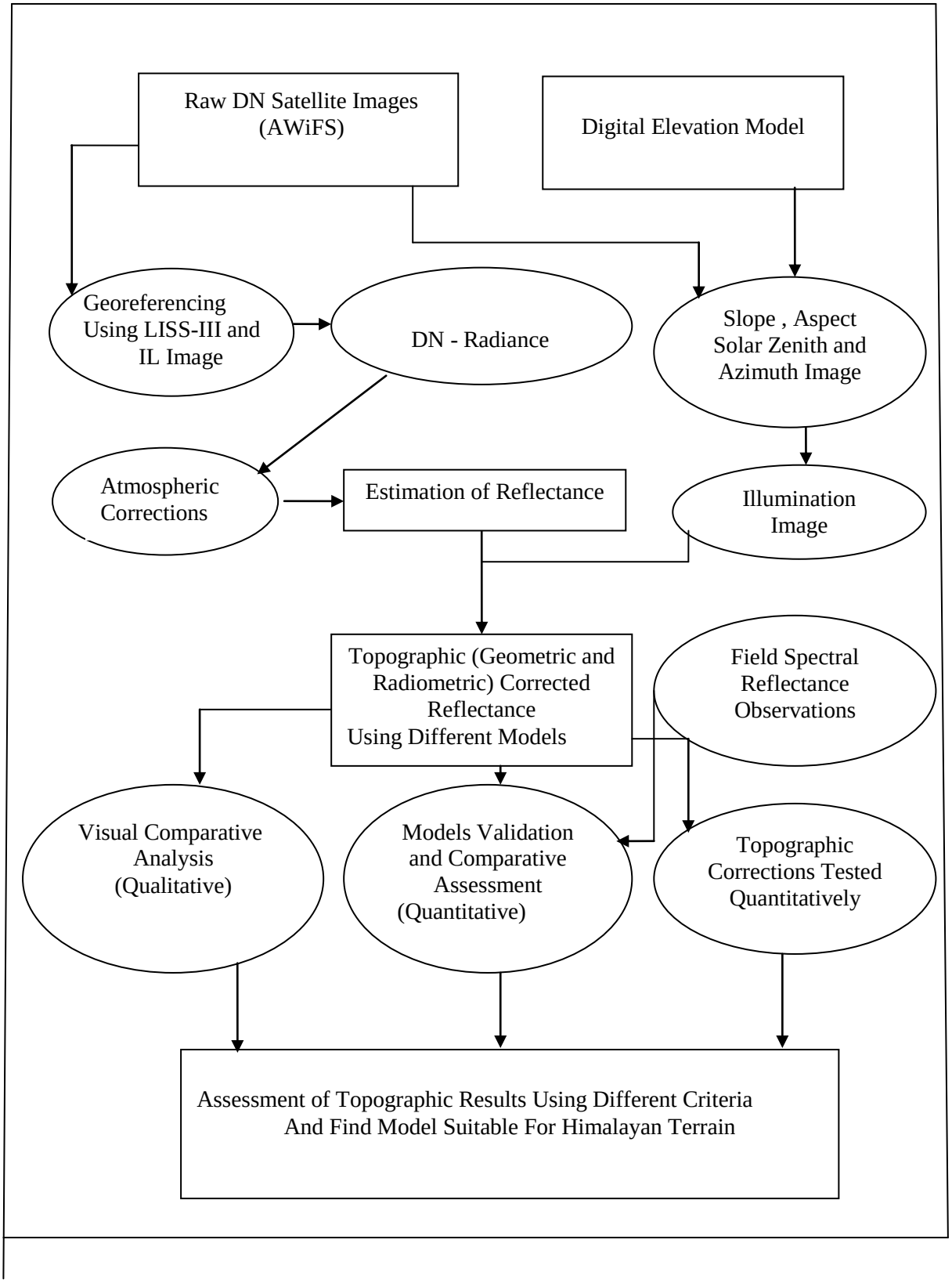

Figure 4.1 Flow chart showing processing steps for different topographic models

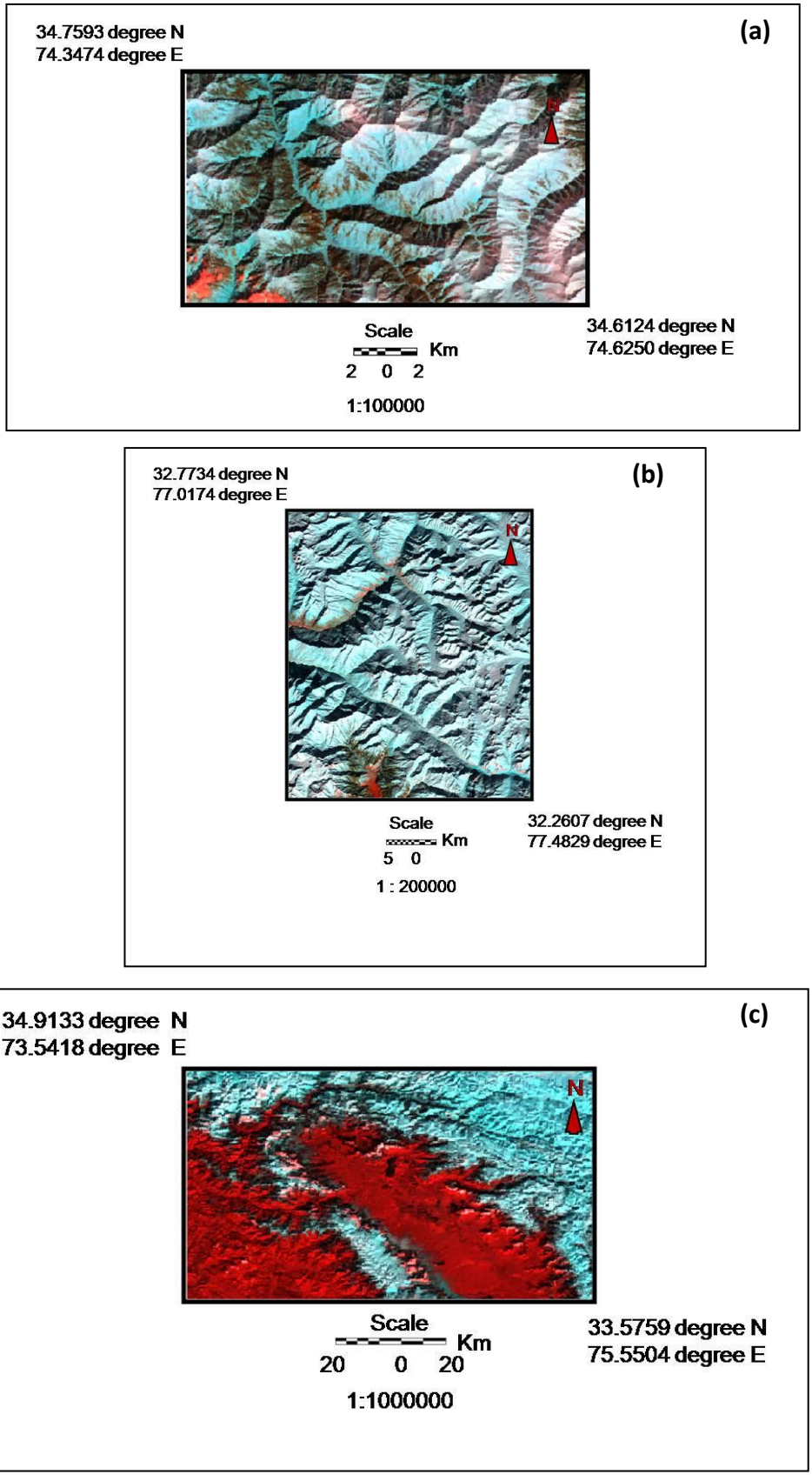

Figure 4.2 Three different study area on (a, b) AWiFS image and (c) MODIS image

range and is located between 33.5759 degree N latitude to 34.9133 degree N latitude and 73.5418 degree E longitude to 75.5504 degree E longitude. The maximum altitude is 5480 m and average value is 2482m. The average slope in this region is 23 degree. In general, the areas area densely forested in between 2400 to 3100 meters altitude. Beyond 3100 meters forest is scanty; however, below 2400 meters area is hebitated. These three areas are considered due to their different terrain features, geomorphology and also to understand the performance of different topographic models from one region to another for greater assurance of their successful implementation. Almost cloud free satellite images recorded by AWiFS sensor onboard IRS-P6 (RESOURCESAT-1) of different regions on 11 December 2005, 18 January 2005, 21 February 2005, 26 February 2005 and 8 January 2009 and MODIS- Terra of 19 January 2005 are used in the present analysis. The salient specifications of AWiFS and MODIS sensors are given in Table 4.3 and Table 4.4 respectively. The selection of these satellite images is mainly to facilitate

(a) Carrying out analysis of the topographic corrections for different solar zenith, azimuth angles and illumination.

(b) Validation of spectral reflectance with satellite estimated results as the field observations were recorded in near real time at the time of satellite pass during most of image acquisition.

4.4.2 Digital elevation model (DEM)

A digital elevation model (DEM) of the study area available with Snow & Avalanche Study Establishment (SASE) was used in the present work. DEM was generated using 1:50,000 toposheet at 40m contour interval for study area in Figure 4.2 (a-b). The non-linear interpolation function is used for 3-D surface generation. The grid resolution of the DEM being 6m was further re-sampled at 56m to bring it equal to the grid resolution of AWiFS satellite images. The Shuttle Radar Topography Mission (SRTM) data of the DEM at 90 m spatial resolution were also used for certain regions of the study area of MODIS images (Figure 4.3c). DEM was further used to generate terrain parameters for topographic models using ERDAS Imagine 8.7. The broad topographic details of the study area have already been given in chapter 3.

4.4.3 Geometric corrections

The master data was prepared first after rectifying high resolution images of LISS –III (Linear Imaging Self Scanning) sensor with spatial resolution of 23.5 m with the Survey

of India (SoI) maps of different study areas. Thereafter, AWiFS images were geo-referenced with LISS-III images. Similarly, moderate resolution (500m) MODIS data were rectified using medium resolution (56m) AWiFS image. The image rectification was finally refined further using illumination images (IL). This step is very necessary because the satellite images used for topographic corrections should match with topographical information generated using SoI maps otherwise it may lead to erroneous results. The nearest neighbor re-sampling method was used and the geo-location error of the model is about half a pixel.

4.5 Computation of solar zenith, solar azimuth, terrain slope and aspect and illumination

4.5.1 Solar zenith angle of the image

The Solar Zenith Angle (θ_z) is the angle between the Sun's rays and the Zenith direction. Its complementary angle (90-Z) is the Solar Altitude (or Elevation). The Solar Zenith Angle (Solar Elevation Angle) is determined from the following equation:

$$\cos\theta_z = (\cos\delta)(\cos\phi)(\cos\hbar) + (\sin\delta)(\sin\phi) \tag{4.16}$$

where δ = Solar Declination angle (+ is North, - is South, ϕ = Latitude of the Location (+ is North, - is South), $\hbar$ = Hour Angle. The mean solar zenith angle estimated for different sensor images are given in the Table 4.3

Table 4.3 Solar geometry of study area on different dates.

Date of satellite pass	Sensor	Mean solar zenith angle (Degree)	Mean Azimuth Angle (Degree)
11 December 2005	AWiFS	58.7	157.5
18 January 2005	AWiFS	55.7	158.6
19 January 2005	MODIS	56.5	160.2
21 February 2005	AWiFS	45	156.7
26 February 2005	AWiFS	46.4	154.6
8 January 2009	AWiFS	57.6	161.7

4.5.2 Solar declination angle

The day of the year is important in determining incoming solar radiation (insolation)

because this determines the Solar Declination. The following equation provides fairly accurate *Declination angle* for any day of the year:

$$\delta = -23.45\cos\left[\frac{360(t_j + 10)}{365}\right] \tag{4.17}$$

Where, t_j = Julian date (Jan 1st =1, Feb 1st =32 etc.), δ = Solar Declination angle (+ is North, - is South).

4.5.3 Solar azimuth angle of the image

The Solar Azimuth angle ($\emptyset_p$) is the angle between the projections onto the horizontal plane of the site of the Sun and the direction of true North. It is measured in clockwise

from north, which has an angular value of 0 to 360^o. The Solar Azimuth angle can be determined from the following equation:

$$\cos \emptyset_p = \frac{(\sin \delta)(\cos \phi) - \cos(\delta)\sin(\phi)\cos(\hbar)}{\sin \theta z} \tag{4.18}$$

where $\emptyset_p$= Solar Azimuth angle, δ = Solar Declination angle (+ is North, - is South), ϕ = Latitude of the Location (+ is North, - is South), $\hbar$ = Hour angle, θ_z= Solar Zenith angle. The mean solar azimuth angle does not vary significantly as given in table 4.3.

4.5.4 Slope and Aspect

Slope and Aspect have generated from Digital Elevation Model (DEM). Slopes and aspects for the study area of AWiFS and MODIS satellite image have shown in Figure 4.3. The Output Slope Image is in Degree meters. Slopes in all three study area vary from 0^0 to 85^0 with a mean value of 22.437^0 to 29.173^0.

The terrain aspect of the image is shown in Figure 4.4. The aspect varies from 0^0–360^0 having a southern trend with a mean value varying from 182.012^0 to 188.662^0.

4.5.5 Incidence angle for illumination

The IL image of the study area computed (Civco 1989; Kawata *et al.,* 1995; Riano *et al.,*

2003) using equation (4.5) is shown in Figure 4.5 (a-c). The IL vary from −1 (low illumination) to +1 (high illumination) which is rescaled to a range of 0–255 for the topographic models. The mean IL is estimated to be 176.8 (11 December 2005), 182.3 (18 January (2005), 177.5 (21 February 2005), 174.0 (26 February 2005), 178.2 (8 January 2009) and 181.5 (19 January 2005).

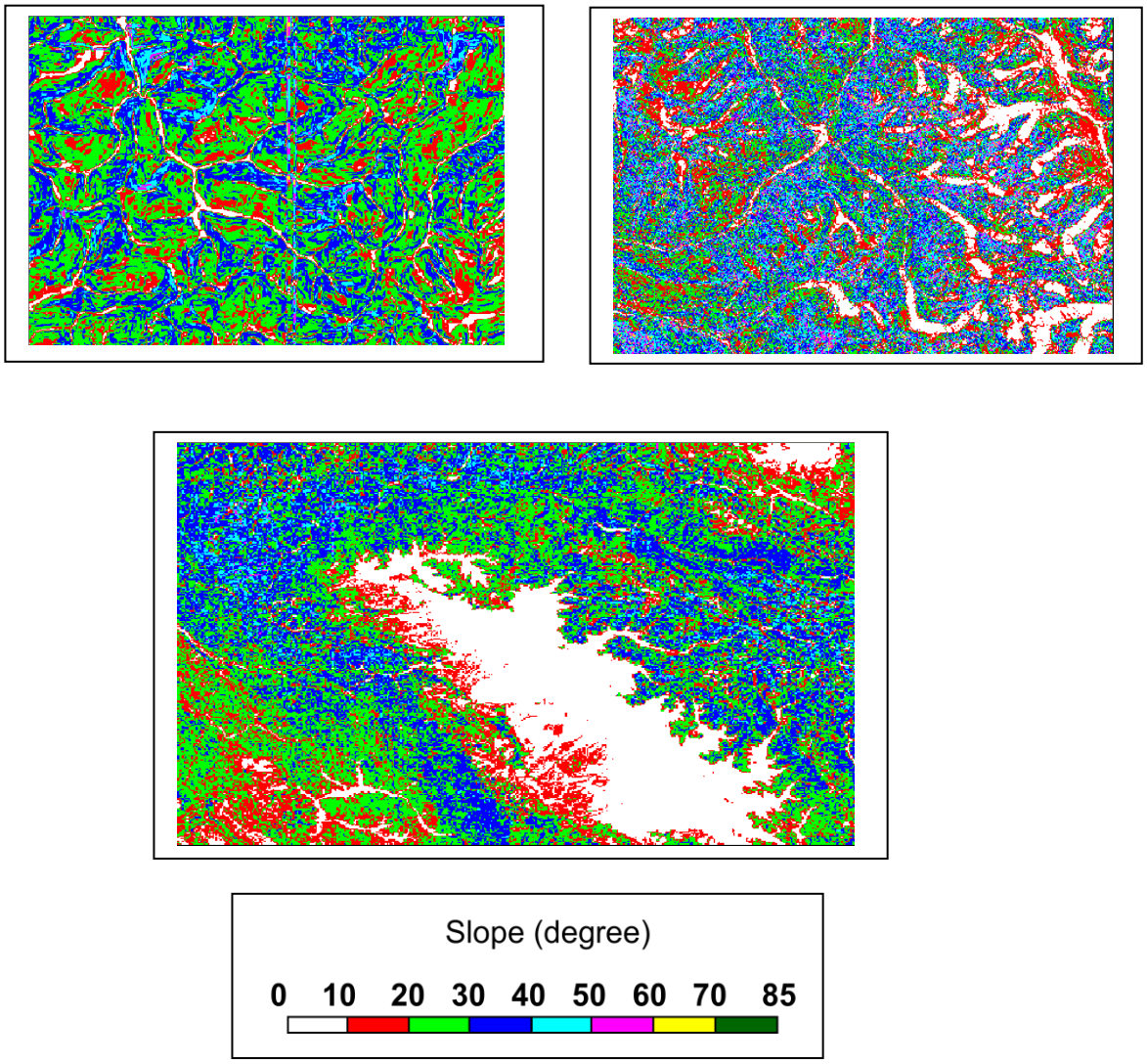

Figure 4.3 Slope variability in different study areas of Himalayan region.

4.5.6 Estimation of coefficients for different topographic correction methods

The results of different coefficient values (c_λ, k (λ) and C_λ) in equations (4.6), (4.7), (4.12) and (4.15) for AWiFS and MODIS images are shown in Table 4.4. It can be inferred that these coefficients are not same for different date images. These differences in the coefficients are attributed to different illumination condition, solar zenith and azimuth angle and temporal changes in snow surface physical properties. The results of Minneart constant show

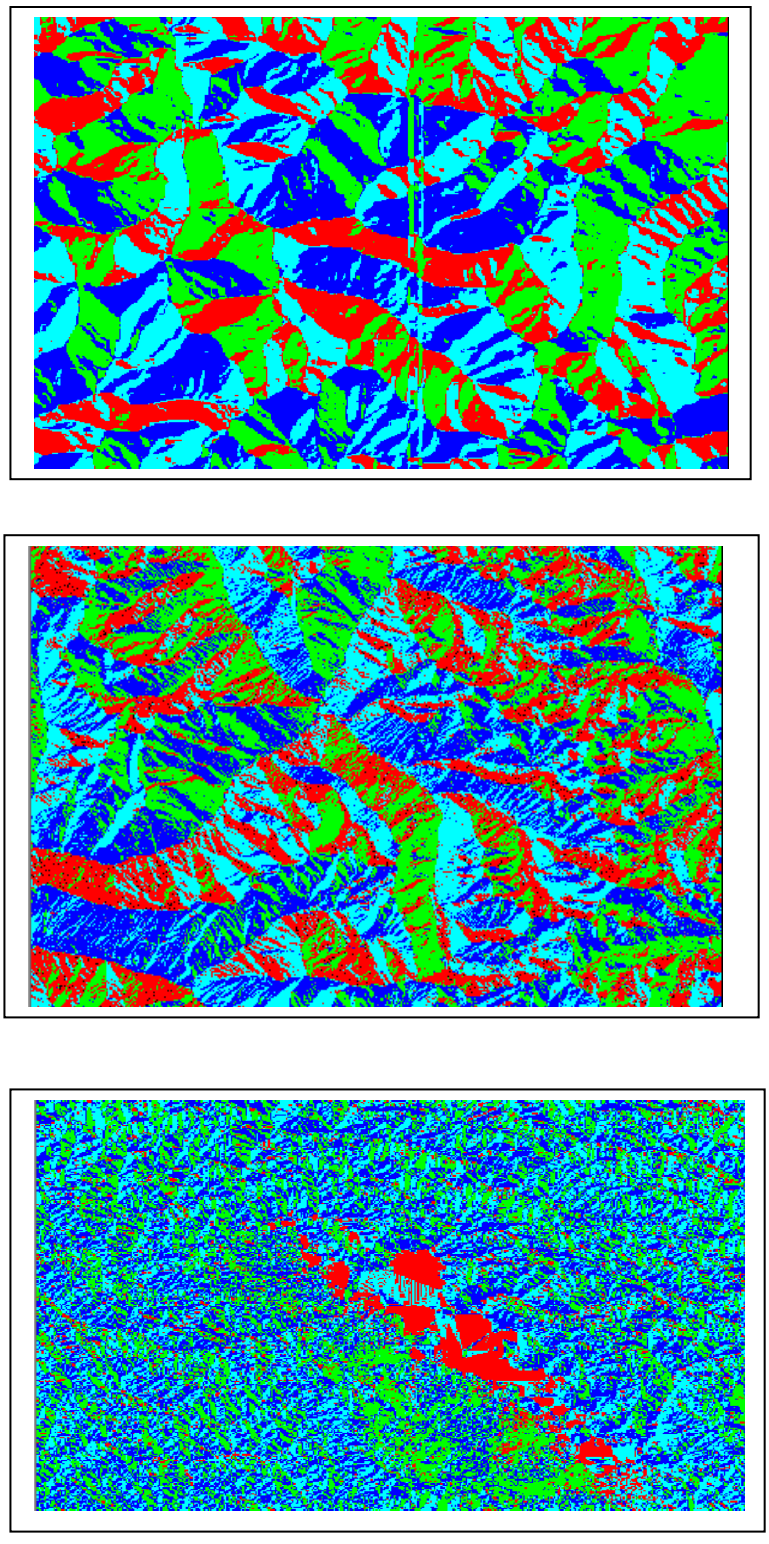

Figure 4.4 Aspect variability of different study areas of Himalaya region.

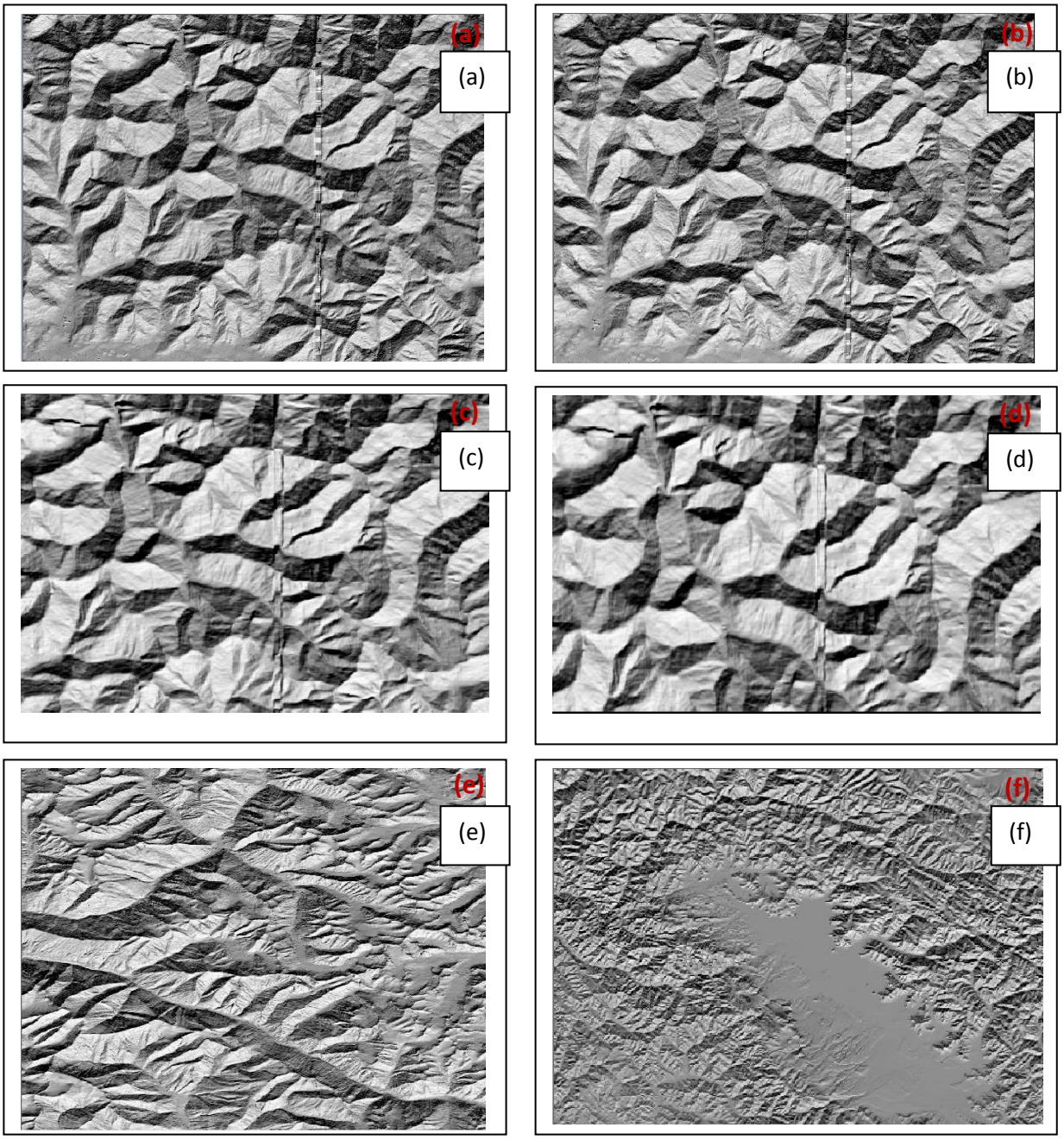

Figure 4.5 IL (illumination image) of (a) 11 Dec. 2005 (b) 18 Jan. 2005 (c) 21 Feb. 2005 (d) 26 Feb. 2005 (e) 8 Jan. 2009 and (f) 19 Jan. 2005.

significantly different values for all the images between zero and one depending on the type of surface (Lambertian or non-Lambertian). The present results are attributed to non-Lambertian surface as $k(\lambda)$ equal to one for perfect Lambertian surface and lies between zero and one for non-Lambertian surface. It can be inferred that Himalayan snow is non-Lambertian although most of the authors have assumed snow surface to be Lambertian in their reflectance model (Conese *et al.,* 1993; Richter, 1997; Xin *et al.,* 2002; Srinivasulu and Kulkarni, 2004).

Table 4.4: Coefficients for different topographic normalization models

Satellite Images	Coefficients			
	C- Correction	Minneart Constant	Two Stage Normalization (Mean Illumination)	Slope Match Method
AWiFS – 11Dec 2005	0.750 0.661 0.630 0.410	0.272 0.310 0.330 0.370	1.613 2.184 3.040 3.932	0.909 0.981 1.032 0.693
AWiFS- 18Jan. 2005	0.535 0.522 0.540 0.555	0.250 0.300 0.333 0.255	2.36 2.88 3.25 3.28	0.835 0.877 0.968 0.122
AWiFS – 21Feb. 2005	0.460 0.447 0.473 0.380	0.519 0.539 0.522 0.498	3.487 3.709 4.039 3.233	0.867 0.891 0.939 0.212
AWiFS – 26 Feb. 2005	0.224 0.284 0.300 0.651	0.54 0.54 0.54 0.35	-	0.87 0.872 0.852 0.119
AWiFS – 8 Jan. 2009	2.92 2.74 2.64 2.73	0.35 0.38 0.40 0.35	-	0.97 1 1 0.5
MODIS- 19 Jan. 2005	8.53 7.78 7.34 11.33 18.17	0.23 0.28 0.32 0.33 0.33	-	0.603 0.643 0.364 0.090 0.070

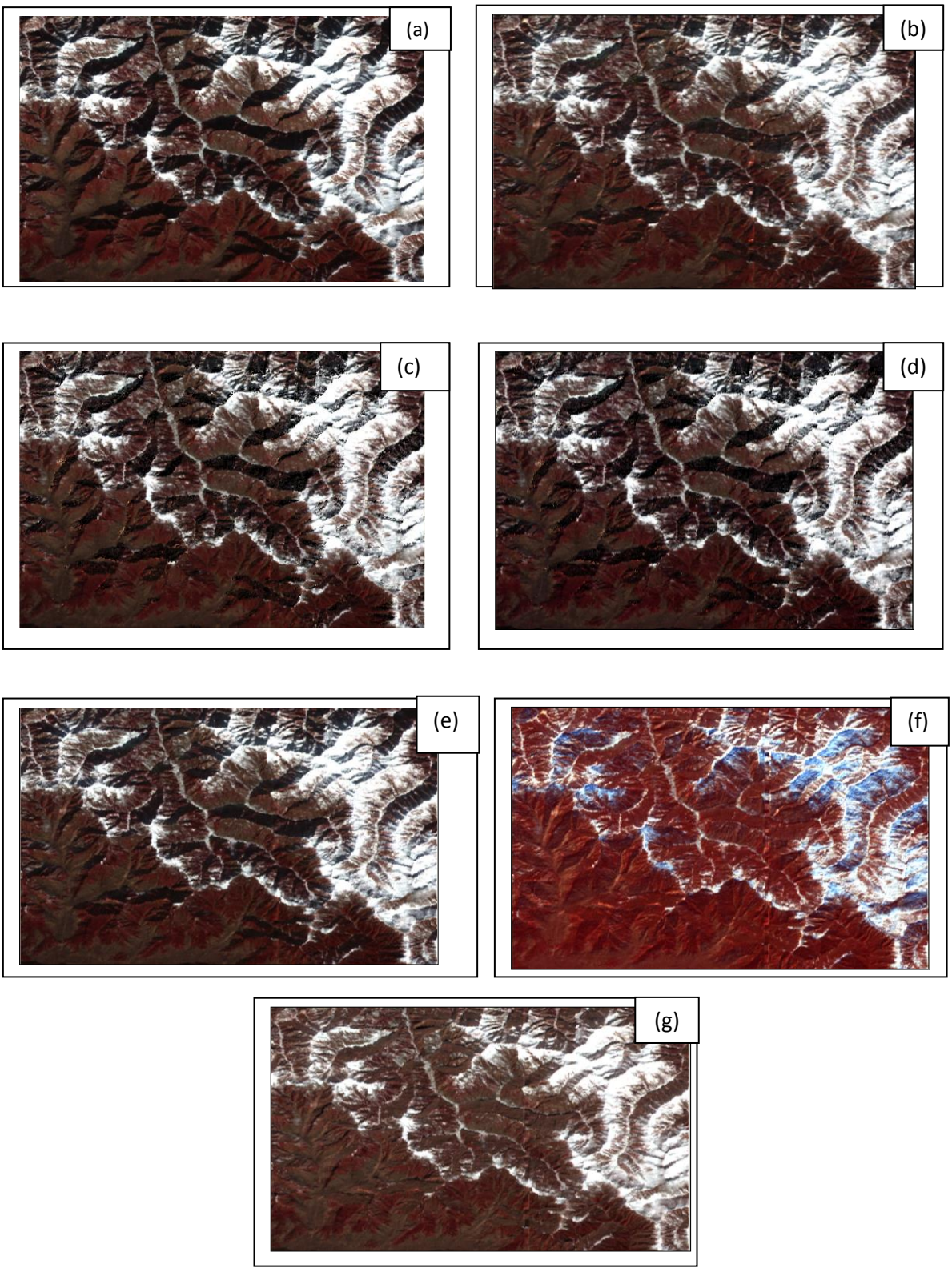

Figure 4.6: Topographically uncorrected and corrected FCC reflectance image in band 2, 3 and 4 of AWiFS – 11 December 2005. (a) Uncorrected (equation 4.1) (b) C-correction (equation 4.6) (c) Minneart method (equation 4.7) (d) Minneart method (equation 4.9) (e) Civco modified version of cosine correction (equation 4.10) (f) two-stage normalization (equation 4.12) and (g) slope match (equation 4.15)

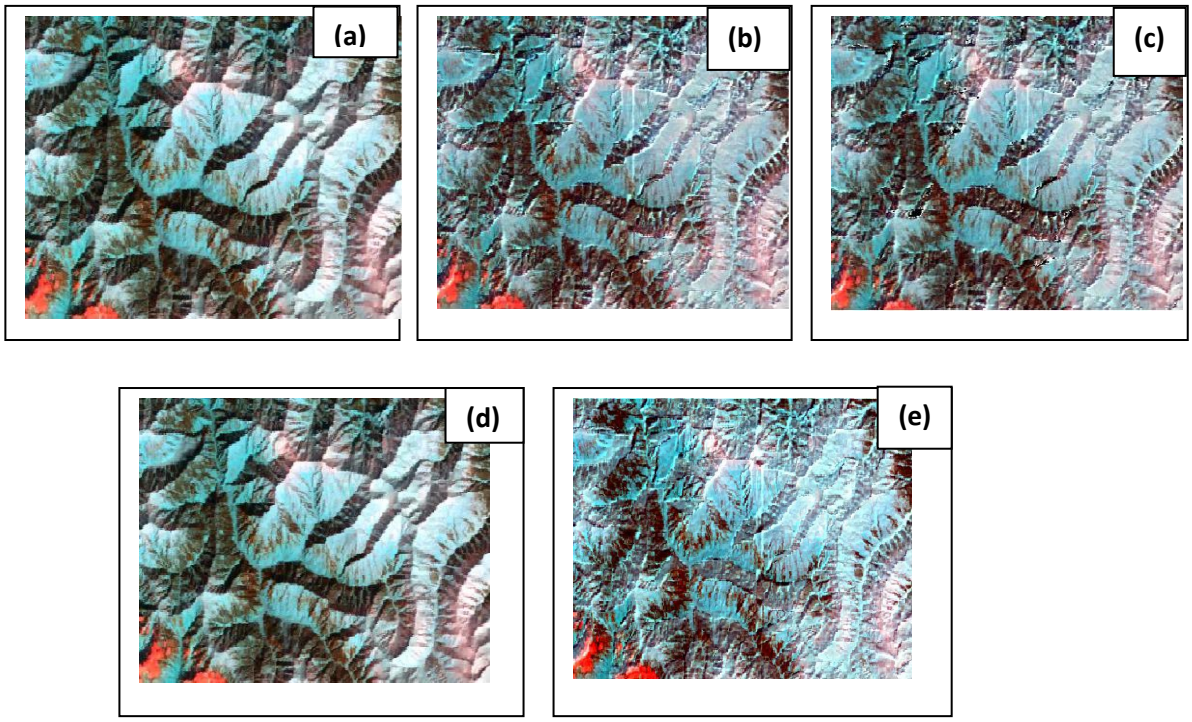

Figure 4.7 : Topographically uncorrected and corrected FCC reflectance image in band 2, 3 and 4 of AWiFS – 26 Feburary 2005 (a) Uncorrected (equation 4.1) (b) C-correction (equation 4.6) (c) Minneart method (equation 4.7) (d) Minneart method (equation 4.9) and (e) slope match (equation 4.15)

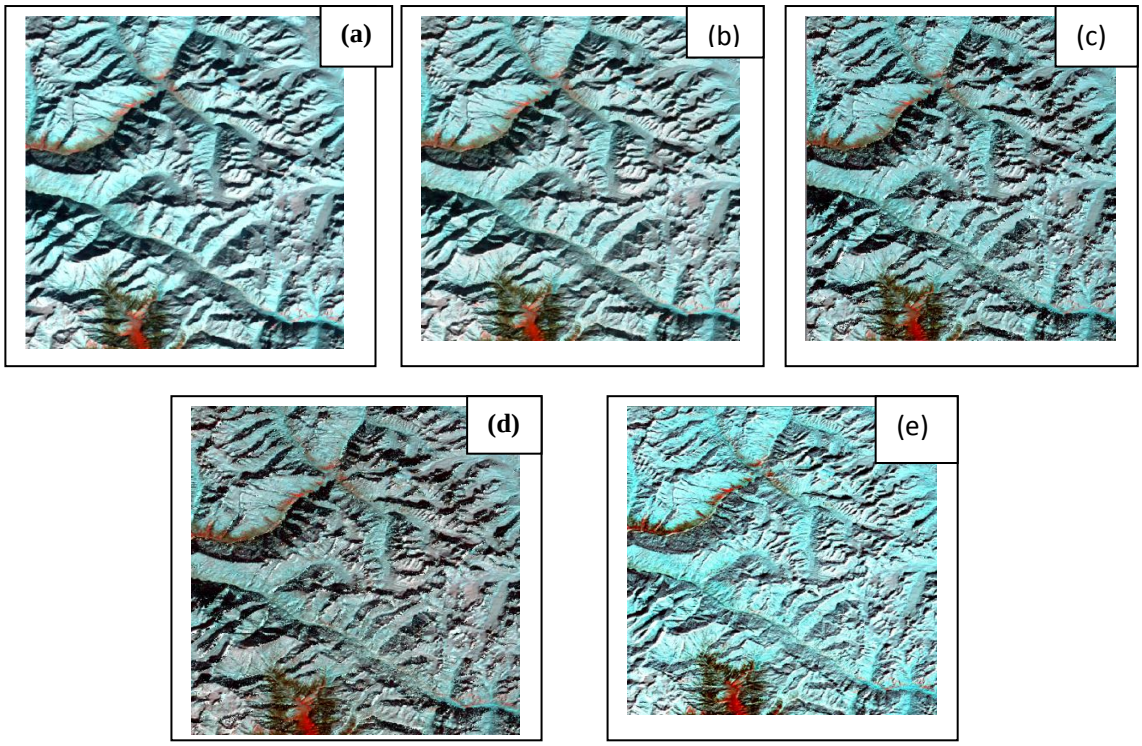

Figure 4.8 FCC images of high and different snow covered regions of AWiFS – 8 January 2009 (a) topographically uncorrected (equation 4.1) (b) C-correction (equation 4.6) (c) Minneart correction (equation 4.7) (d) Minneart correction (equation 4.9) and (e) slope match method (equation 4.15).

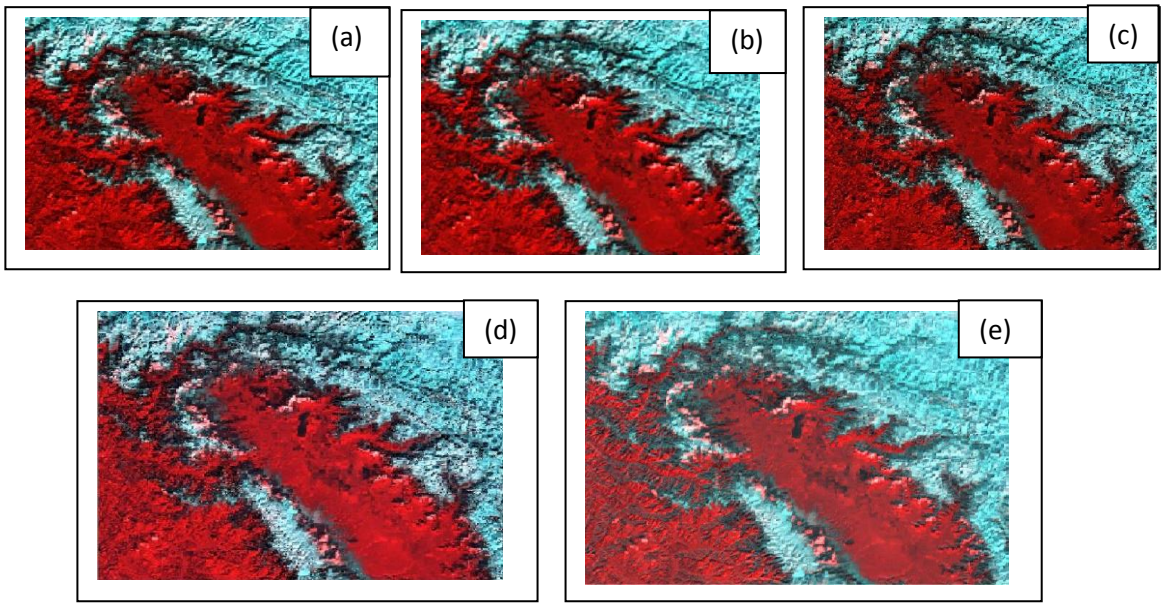

Figure 4.9 FCC images of high and different snow covered regions of MODIS – 19 January 2005 (a) topographically uncorrected (equation 4.1) (b) C-correction(equation 4.6) (c) Minneart correction (equation 4.7) (d) Minneart correction (equation 4.9) and (e) slope match method (equation 4.15).

4.6 Application of topographic models in the Himalayan terrain and field Results

Figures 4.6 represents the false colour composite AWiFS image (B2 = blue, B3 = green and B4 = red) of 11 December 2005 (a) original uncorrected reflectance image (equation 4.1), (b) C-correction (equation 4.6) (c, d) Minneart correction (equations 4.7 and 4.9) , (e) Civco's modified cosine corrections (equation 4.10), (f) Two stage normalization (equation 4.12) and (g) slope matching technique (equation 4.15). Figures 4.7, Figures 4.8 and Figures 4.9 show the results of topographic corrections by different methods on AWiFS and MODIS images of high snow covered area of different Himalayan regions. These additional results are shown in order to do robust analysis of different topographic models in different Himalayan ranges having varying terrain variability and solar geometry. The visual analysis of the topographic results is compared qualitatively with the normalized difference snow index (NDSI) also. The NDSI is calculated using the following equation (Hall *et al.*, 1995):

$$\mathrm{NDSI} = \frac{R_{\mathrm{green}} - R_{\mathrm{SWIR}}}{R_{\mathrm{green}} + R_{\mathrm{SWIR}}}, \tag{4.19}$$

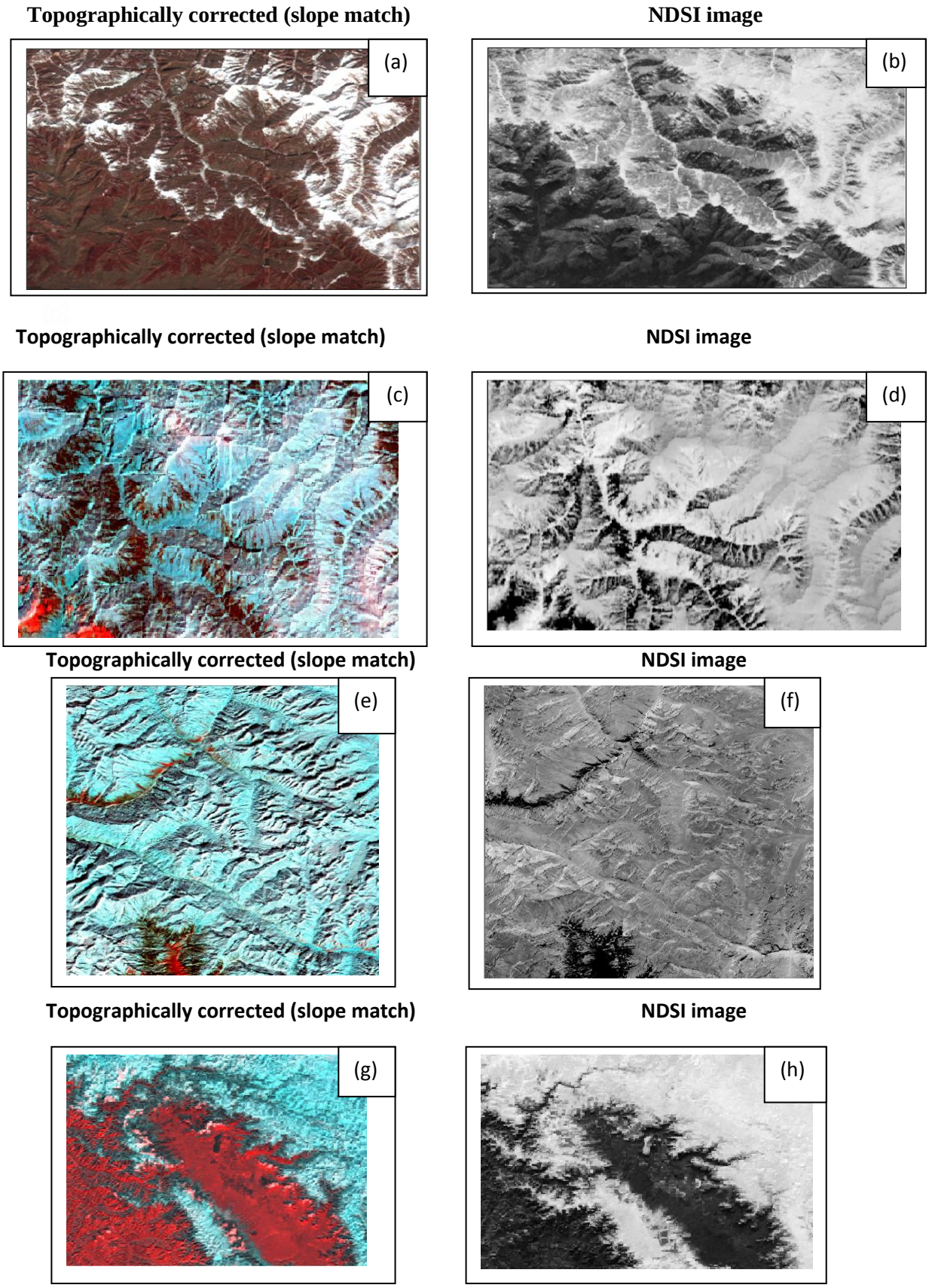

Figure 4.10 (a-h) Topographic corrected image of AWiFS (a,c,e) and MODIS (g) using slope match and their corresponding NDSI image (b,d,f) and (h).

Where R_{green} and R_{SWIR} are the reflectances in green (520–590 nm for AWiFS and 545 – 565 nm for MODIS) and short wave infrared (1550–1700 nm for AWiFS and 1628 – 1652 nm for MODIS) bands of AWiFS and MODIS respectively. The topographically corrected results by slope match method only for AWiFS and MODIS and their corresponding NDSI images are shown in the Figure 4.10.

4.7 Field Observations of the spectral response of snow in the study area

Figures 4.11 (a–b) and Figures 4.12 (a-c) show the *in-situ* results of spectral characteristics of reflectance (average of multiple observations on snow surfaces) of pure snow measured in the field in open area without any interference from the surroundings in near real-time for 18 January 2005, 21 February 2005, 26 February 2005, 8 January 2009 and 19 January 2005. The field observations were collected at SASE observatory at Dhundi and Z-Gali as shown in the Figure 4.13. The Field-Specification FR Spectroradiometer (Figure 4.14) obtained from M/S Analytical Spectral devices; USA in the wavelength range from 350 nm to 2500 nm was used to record the spectral reflectance of snow surface in field area. The sampling interval for the instrument is 1.4 nm for the region 350–1000 nm and 2 nm for the region 1000–2500 nm. The full width-half-maximum (FWHM) spectral resolution of the Spectroradiometer is 3 nm for the region 350–1000 nm and 10 nm for the region1000–2500 nm. These field observations are used to validate the satellite estimated reflectance results in the AWiFS and MODIS satellite bands using different topographic correction models. The quantitative results of satellite estimated reflectance values for AWiFS and MODIS spectral bands using different topographic model with field validation (using *in-situ* observations) are given in Table 4.7 and Table 4.8. The spectral reflectance of snow samples on the south and north aspects of few AWiFS and MODIS images of uncorrected and topographically corrected using slope matching method are shown in the Figures 4.15 to 4.19. The detailed quantitative analyses results of spectral reflectance for snow area in sunlit and shadow regions using different topographic models are given in Tables 4.9 to 4.14.

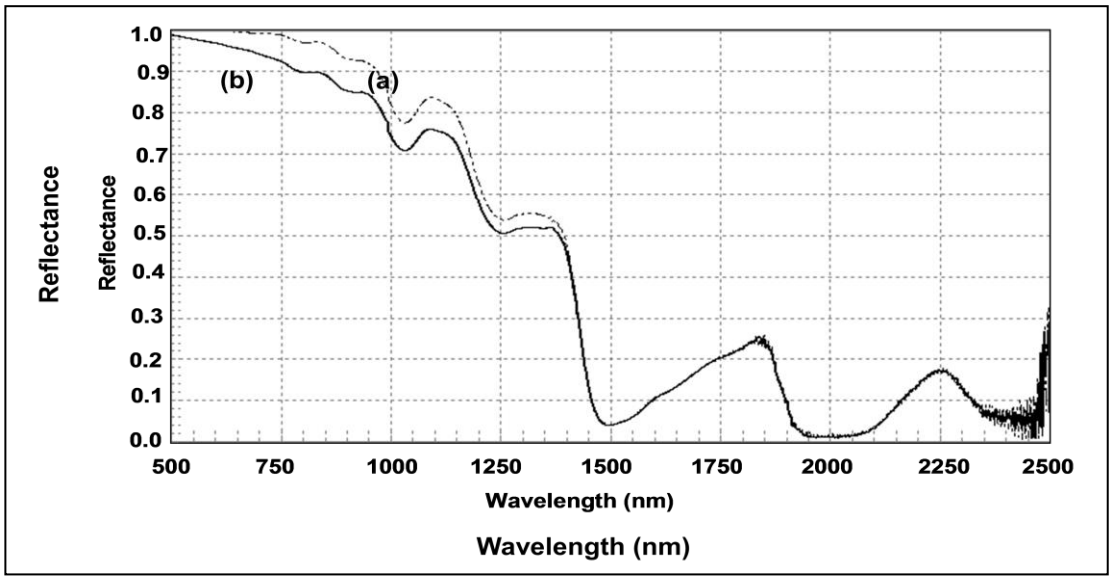

Figure 4.11 In- situ observations of spectral reflectance characteristics of pure snow (a) 18 January 2005 and (b) 21 February 2005.

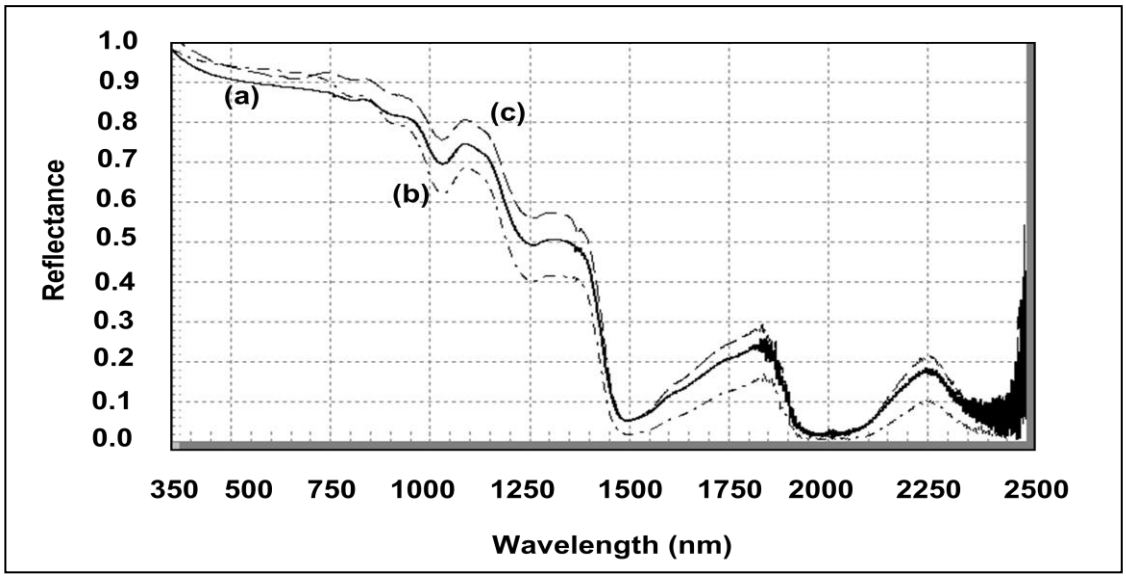

Figure. 4.12 In- situ observations of spectral reflectance characteristics of pure snow (a) 19 January 2005 (b) 26 February 2005 and (c) 8 January 2009

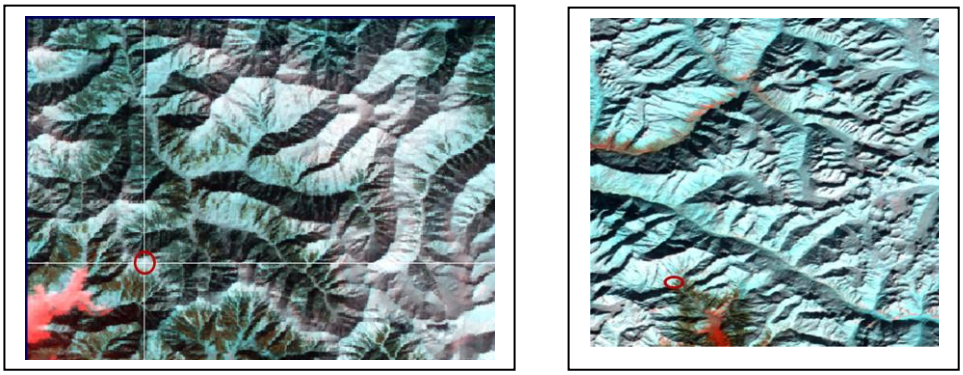

Figure 4.13 Field locations (red circle) for spectral reflectance characteristics using optical spectroradiomer (Left – Dhundi) and Right (Z-Gali).

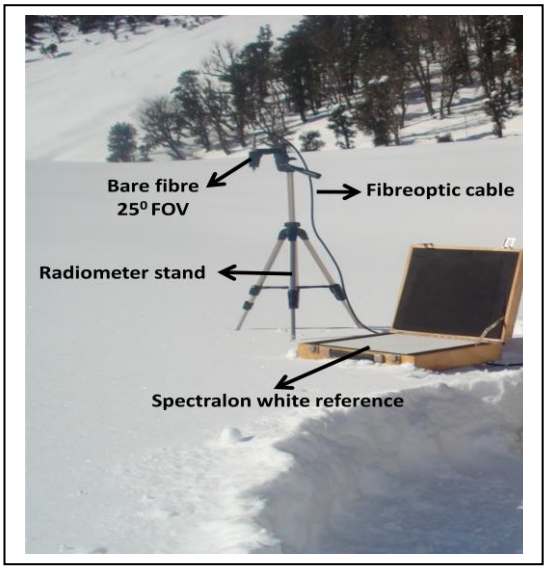

Figure. 4.14 Optical spectro-radiometer in snow field Dhundi location.

Table 4.5 : Validation of topographic normalization models with field results of spectral reflectance using spectro-radiometre.

AWiFS – Date : 18Jan. 2005, Pixel Location : Latitude (34.626) and Longitude (74.416) Slope : 9.4 degree and Aspect : South (180 degree)				
Topographic Models	Spectral Reflectances in AWiFS Bands			
	B2:520-590 nm	B3: 620-680 nm	B4: 770-860 nm	B5: 1550-1700 nm
Original Image	0.947	0.977	1	0.135
C-correction(eq.4.6)	0.841	0.854	0.874	0.120
Minneart (eq.4.7)	0.877	0.908	0.926	0.133
Minneart (eq.4.9)	0.865	0.893	0.914	0.124
Civco (eq.4.10)	0.761	0.786	0.804	0.109
Two Stage (eq.4.12)	0.426	0.322	0.243	0.032
SlopeMatch eq.4.15)	0.989	1	1	0.141
Field Results	1	1	0.96	0.132
AWiFS – Date : 21Feb. 2005, Pixel Location : Latitude (34.624) and Longitude (74.421) Slope : 11.3degree and (Aspect : South 165 degree)				
Original Image	0.974	0.958	0.948	0.126
C-correction(eq.4.6)	0.862	0.854	0.857	0.113
Minneart (eq.4.7)	0.891	0.874	0.866	0.116
Minneart (eq.4.9)	0.882	0.866	0.858	0.115
Civco (eq.4.10)	0.751	0.740	0.731	0.098
Two Stage (eq.4.12)	0.580	0.532	0.521	0.045
SlopeMatch(eq.4.15)	1	0.993	0.984	0.131
Field Results	0.978	0.957	0.90	0.135

Table 4.6 Validation of topographic normalization models with field results of spectral reflectance using spectro-radiometre.

AWiFS – Date : 26 Feb. 2005, Pixel Location : Latitude (34.6253) and Longitude (74.4146) Slope : 15.9 degree				
Topographic Models	Spectral Reflectances in AWiFS Bands			
	B2:520-590 nm	B3: 620-680 nm	B4: 770-860 nm	B5: 1550-1700 nm
Original Image	0.889	0.889	0.869	0.073
C-correction(eq.4.6)	0.778	0.778	0.763	0.066
Minneart (eq.4.7)	0.805	0.805	0.787	0.068
Minneart including slope(eq.4.9)	0.790	0.790	0.773	0.067
Slope Match (eq.4.15)	0.911	0.910	0.891	0.074
Field Results	0.933	0.926	0.88	0.06
AWiFS – Date : 08 Jan. 2009, Pixel Location : Latitude (32.3564) and Longitude (77.1252) Slope : 18.2degree				
Original Image	0.903	0.878	0.940	0.141
C-correction(eq.4.6)	0.849	0.823	0.879	0.141
Minneart (eq.4.7)	0.826	0.813	0.804	0.131
Minneart including slope(eq.4.9)	0.776	0.747	0.796	0.121
Slope Match (eq.4.15)	0.936	0.934	0.934	0.146
Field Results	0.937	0.919	0.912	0.145

MODIS – Date 19Jan.2005, Pixel Location : Latitude (34.6574) and Longitude (74.3983) Slope : 19.9 degree					
	B3	B4	B5	B6	B7
Original Image	0.969	0.989	0.704	0.186	0.075
C-correction(eq.4.6)	0.953	0.970	0.686	0.180	0.075
Minneart (eq.4.7)	0.907	0.912	0.657	0.169	0.070
Minneart including slope(eq.4.9)	0.885	0.892	0.629	0.165	0.067
Slope Match (eq.4.15)	0.948	0.865	0.703	0.187	0.096
Field Results	0.921	0.900	0.50	0.129	0.070

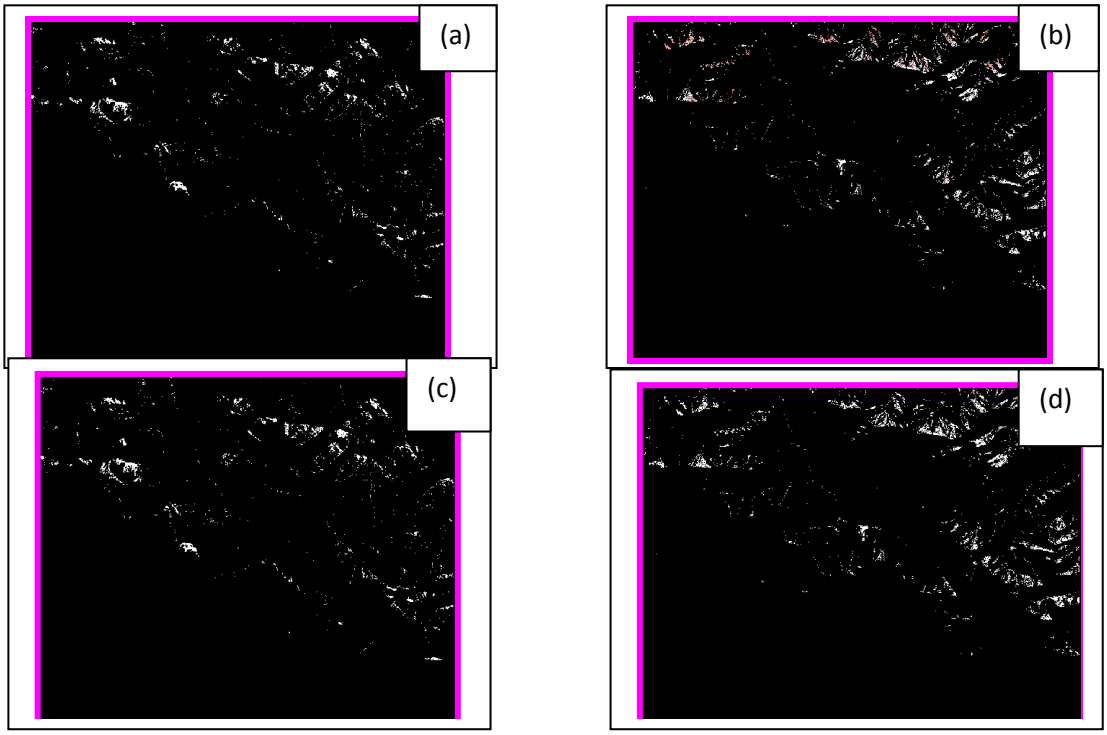

Figure 4.15 Snow samples on the south and north aspect for AWiFS image of 11 December 2005 (a) south aspect before topographic correction (b) north aspect before topographic corrections (c) south aspect after topographic corrections using slope match and (d) north aspect after topographic corrections using slope match.

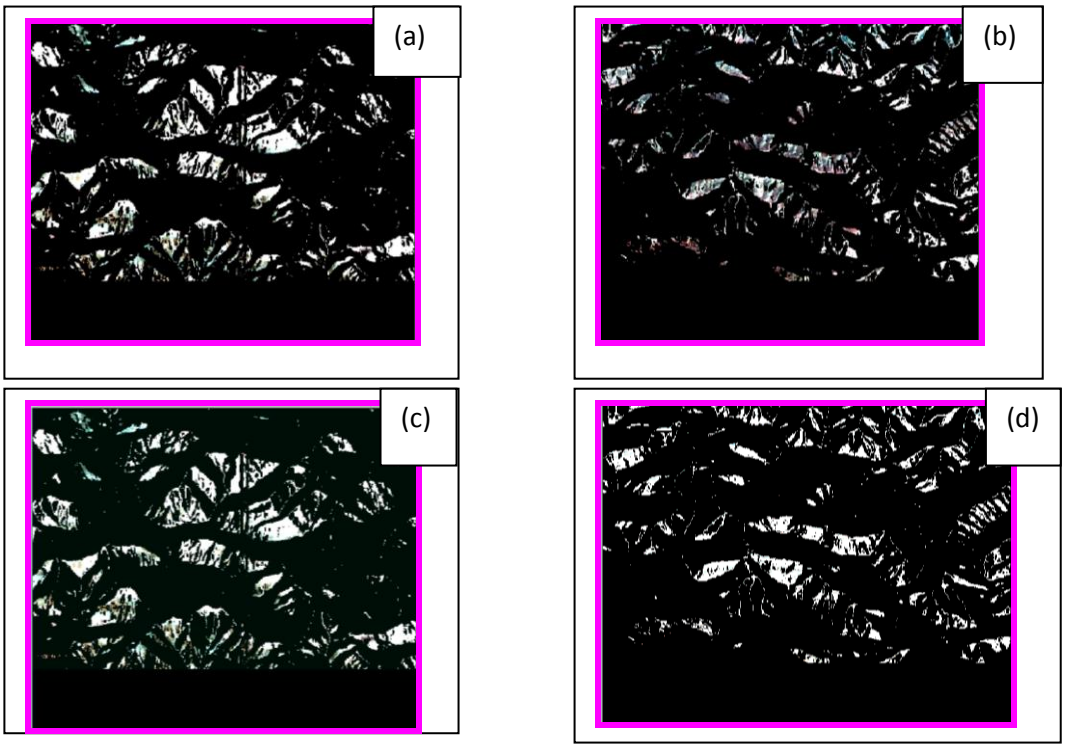

Figure 4.16 Snow samples on the south and north aspect for AWiFS image of 21 February 2005 (a) south aspect before topographic correction (b) north aspect before topographic corrections (c) south aspect after topographic corrections using slope match and (d) north aspect after topographic corrections using slope match.

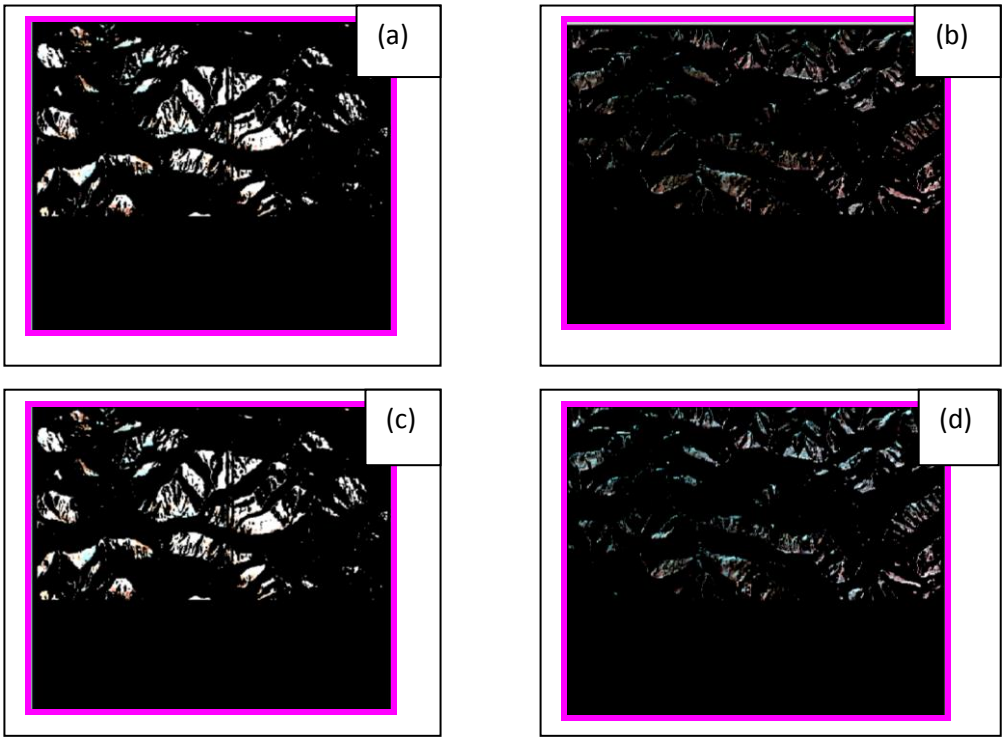

Figure. 4.17 Snow samples on the south and north aspect for AWiFS image of 26 February 2005 (a) south aspect before topographic correction (b) north aspect before topographic corrections (c) south aspect after topographic corrections using slope match and (d) north aspect after topographic corrections using slope match.

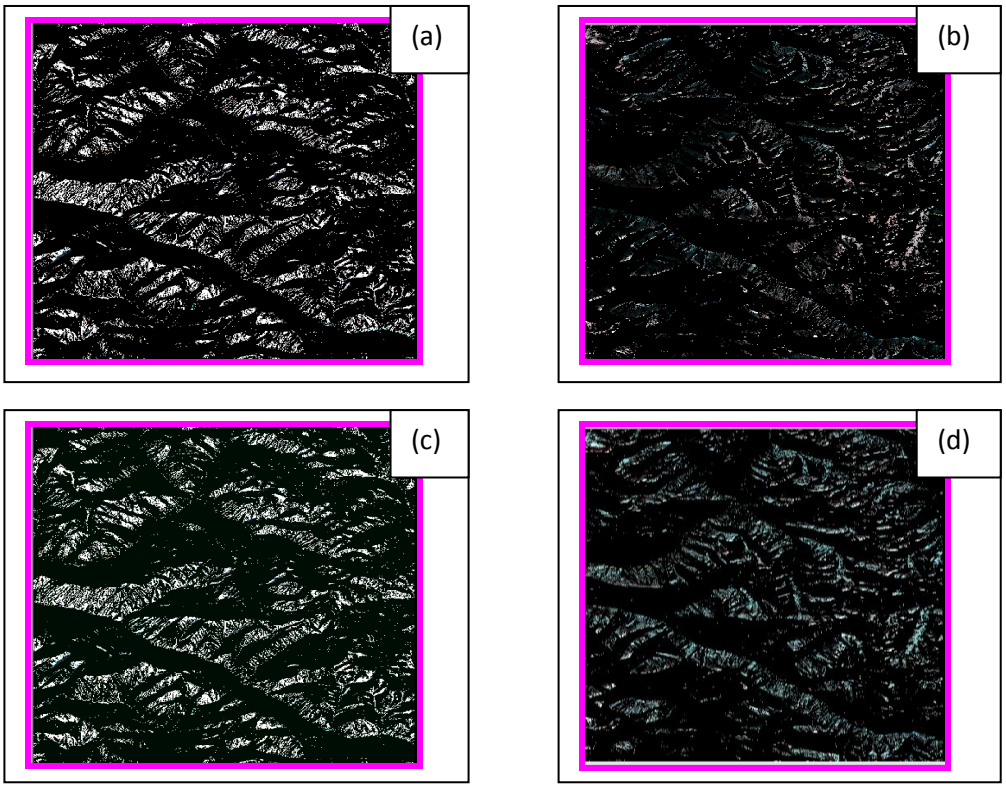

Figure 4.18 Snow samples on the south and north aspect for AWiFS image of 8 January 2009 (a) south aspect before topographic correction (b) north aspect before topographic corrections (c) south aspect after topographic corrections using slope match and (d) north aspect after topographic corrections using slope match.

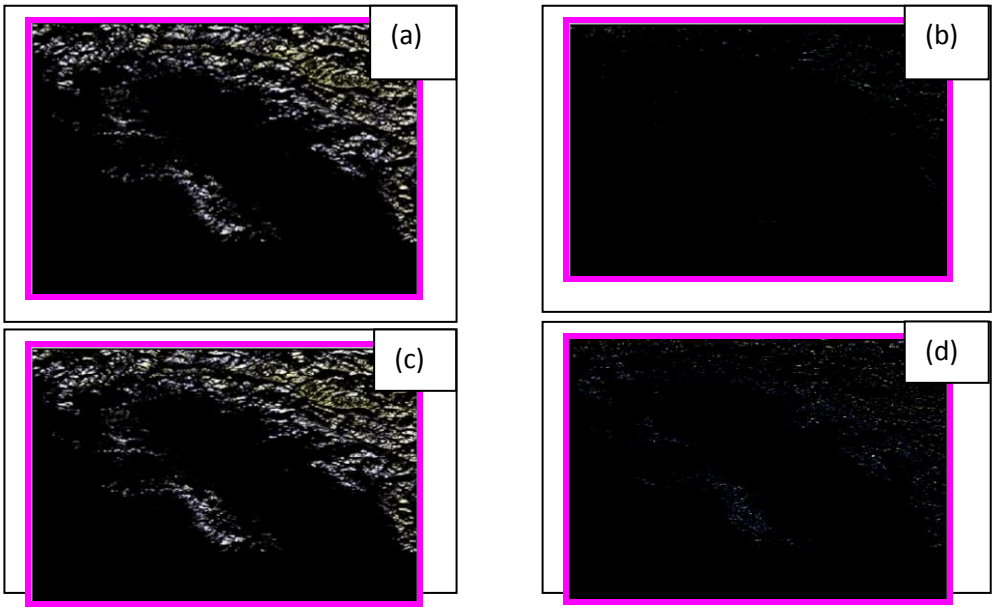

Figure 4.19 Snow samples on the south and north aspect for MODIS image of 19 January 2005 (a) south aspect before topographic correction (b) north aspect before topographic corrections (c) south aspect after topographic corrections using slope match and (d) north aspect after topographic corrections using slope match.

Topographic corrections are also tested using a criteria based on graphical analysis of R_T (reflectance on the tilted surface) and R_H (topographically corrected reflectance) *versus* IL for few images of AWiFS and MODIS proposed by various authors (Meyer *et al.*, 1993; Ekstrand, 1996) are shown in Figure 4.20 and Figure 4.21.

4.8 Visual analysis (qualitative analysis)

The visual interpretation of the false color composite images (Figure 4.6 to Figure 4.9) reveals that occlusions due to terrain illumination effects in the original image after topographic corrections are still pronounced except for two-stage normalization (Figure 4.6 f) and slope matching (Figure 4.6 g and Figure 4.7(e), 4.8(e) and 4.9 (e)). Areas of slopes that face away from the Sun are still darker and three dimensional relief impressions are not suppressed completely. However, visual analysis of the results obtained by slope matching method looks more realistic as compared to two-stage normalization, which shows very high brightness on the sunny and shady slopes (Figure 4.6 f, g). Although, corrected images using both these methods show flat view of the terrain, and the three dimensional relief effects is minimized. The visual analysis by slope matching also reveals that there is less variability in spectral response of the snow classes and can handle the corrections for the problem of shaded relief very well, where the incident angle i is $\geq 90^0$.The similar interpretation for

visual analysis are also reported by (Law and Nichol, 2004; Nichol, 2006) for high resolution IKONOS data.

The topographically corrected results are compared visually with NDSI images (Figures 4.10 a-h) also. NDSI is used to monitor snow cover information under mountain shadow and it can very well identify snow in shadow areas. The visual comparative analysis of topographically corrected results by slope matching method (Figures 4.10 a, c, e, g) with NDSI images (Figures 4.10 b, d, f, h) show that only this method gives most acceptable results and retrieve the actual land cover information for low illumination areas ($\cos i \leq 0$) and other methods fail to produce successful results.

Table 4.7 Comparative quantitative analysis of mean value of snow samples on south and north aspect of an entire image of study area in AWiFS of 11 December 2005 using different topographic models.

AWiFS 11Dec. 2005	**Spectral reflectance of snow samples in AWiFS bands on the south and north aspect of an entire image**			
	B2	B3	B4	B5
Original Image				
S-aspect	0.669	0.697	0.731	0.100
N-aspect	0.276	0.276	0.289	0.041
C-correction (eq.4.6)				
S-aspect	0.559	0.575	0.600	0.081
N-aspect	0.397	0.376	0.425	0.068
Minneart (eq.4.7)				
S-aspect	0.601	0.617	0.642	0.086
N-aspect	0.408	0.425	0.453	0.074
Minneart (eq.4.9)				
S-aspect	0.560	0.577	0.602	0.081
N-aspect	0.384	0.402	0.430	0.069
Civco (eq. 4.10)				
S-aspect	0.499	0.520	0.545	0.074
N-aspect	0.349	0.348	0.363	0.053
Two stage (eq.4.12)				
S-aspect	0.472	0.312	0.168	0.077
N-aspect	0.361	0.423	0.491	0.123
SlopeMatch(eq.4.15)				
S-aspect	0.675	0.703	0.738	0.101
N-aspect	0.675	0.703	0.724	0.102

Table 4.8 Comparative quantitative analysis of mean value of snow samples on south and north aspect of an entire image of study area in AWiFS of 18 January 2005 using different topographic models.

AWiFS 18 Jan. 2005	Spectral reflectance of snow samples in AWiFS bands on the south and north aspect of an entire image			
	B2	B3	B4	B5
Original Image S-aspect N-aspect	 0.669 0.257	 0.663 0.227	 0.697 0.228	 0.089 0.033
C-correction (eq.4.6) S-aspect N-aspect	 0.558 0.360	 0.548 0.334	 0.576 0.334	 0.075 0.048
Minneart (eq.4.7) S-aspect N-aspect	 0.583 0.405	 0.586 0.356	 0.616 0.355	 0.079 0.055
Minneart (eq.4.9) S-aspect N-aspect	 0.539 0.377	 0.540 0.332	 0.568 0.332	 0.073 0.051
Civco (eq. 4.10) S-aspect N-aspect	 0.480 0.340	 0.482 0.297	 0.506 0.298	 0.298 0.045
Two stage (eq.4.12) S-aspect N-aspect	 0.472 0.361	 0.312 0.423	 0.168 0.491	 0.077 0.123
SlopeMatch(eq.4.15) S-aspect N-aspect	 0.652 0.645	 0.654 0.645	 0.687 0.675	 0.089 0.084

4.9 Validation of results with field observed data

The results obtained using different topographic models are compared with the *in-situ* observations of spectral reflectance recorded at the time of satellite pass at Indian standard time (1100 IST) on 18 January 2005, 21 February2005, 26 February 2005, 8January 2009 and 19 January 2005. The field observations for 11 December 2005 were not available, therefore, topographic results are compared only for four AWiFS images of January and February 2005 and one MODIS image of 19 January 2005. The field

Table 4.9 Comparative quantitative analysis of mean value of snow samples on south and north aspect of an entire image of study area in AWiFS of 21 February 2005 using different topographic models.

AWiFS 21 Feb. 2005	Spectral reflectance of snow samples in AWiFS bands on the south and north aspect of an entire image			
	B2	B3	B4	B5
Original Image				
S-aspect	0.775	0.775	0.785	0.096
N-aspect	0.300	0.288	0.274	0.036
C-correction (eq.4.6)				
S-aspect	0.669	0.663	0.683	0.098
N-aspect	0.460	0.438	0.431	0.059
Minneart (eq.4.7)				
S-aspect	0.677	0.674	0.685	0.085
N-aspect	0.482	0.468	0.438	0.059
Minneart (eq.4.9)				
S-aspect	0.643	0.641	0.651	0.080
N-aspect	0.454	0.443	0.413	0.055
Civco (eq. 4.10)				
S-aspect	0.531	0.532	0.538	0.066
N-aspect	0.391	0.374	0.355	0.048
Two stage (eq.4.12)				
S-aspect	0.546	0.544	0.543	0.035
N-aspect	0.352	0.330	0.314	0.032
SlopeMatch(eq.4.15)				
S-aspect	0.751	0.751	0.759	0.094
N-aspect	0.726	0.725	0.735	0.092

observations are collected at number of points for pure snow samples and the mean of all the observations are estimated (Figures 4.11 and 4.12).

As the surrounding field area has coniferous trees, it is very difficult to verify the field reflectance results accurately at the same latitude and longitude with the satellite estimated value because of these objects, which may give some variations in the reflectance values of medium and moderate spatial resolution pixels of 56m and 500m respectively. Therefore, the satellite estimated reflectance was verified with the field results in the neighbourhood pure pixel of snow on the image. It is observed from Figure 4.11 and Figure 4.12 that reflectance of snow is high at the red end of the visible

Table 4.10 Comparative quantitative analysis of mean value of snow samples on south and north aspect of an entire image of study area in AWiFS of 26 February 2005 using different topographic models.

AWiFS 26 Feb. 2005	Spectral reflectance of snow samples in AWiFS bands on the south and north aspect of an entire image			
	B2	B3	B4	B5
Original Image				
S-aspect	0.750	0.753	0.749	0.059
N-aspect	0.300	0.325	0.334	0.039
C-correction (eq.4.6)				
S-aspect	0.640	0.642	0.640	0.053
N-aspect	0.545	0.546	0.555	0.054
Minneart (eq.4.7)				
S-aspect	0.667	0.670	0.665	0.055
N-aspect	0.538	0.539	0.554	0.056
Minneart (eq.4.9)				
S-aspect	0.636	0.638	0.634	0.0513
N-aspect	0.510	0.511	0.526	0.0510
SlopeMatch(eq.4.15)				
S-aspect	0.749	0.752	0.748	0.059
N-aspect	0.754	0.725	0.755	0.065

Table 4.11 : Comparative quantitative analysis of mean value of snow samples on south and north aspect of an entire image of study area in AWiFS of 8January 2009 using different topographic models.

AWiFS 8 January 2009	Spectral reflectance of snow samples in AWiFS bands on the south and north aspect of an entire image			
	B2	B3	B4	B5
Original Image				
S-aspect	0.859	0.854	0.853	0.152
N-aspect	0.392	0.373	0.339	0.066
C-correction (eq.4.6)				
S-aspect	0.792	0.785	0.781	0.139
N-aspect	0.437	0.418	0.402	0.075
Minneart (eq.4.7)				
S-aspect	0.741	0.728	0.721	0.131
N-aspect	0.558	0.548	0.529	0.105
Minneart (eq.4.9)				
S-aspect	0.663	0.655	0.650	0.117
N-aspect	0.538	0.530	0.513	0.099
SlopeMatch (eq.4.15)				
S-aspect	0.853	0.849	0.847	0.152
N-aspect	0.786	0.782	0.766	0.151

Table 4.12 Comparative quantitative analysis of mean value of snow samples on south and north aspect of an entire image of study area in MODIS of 19 January 2005 using different topographic models.

MODIS – 19 January2005	Spectral reflectance of snow samples in MODIS bands on the south and north aspect of an entire image				
	B3	B4	B5	B6	B7
Original Image S-aspect N-aspect	0.712 0.480	0.695 0.437	0.444 0.269	0.110 0.064	0.048 0.031
C-correction (eq.4.6) S-aspect N-aspect	0.696 0.494	0.678 0.452	0.429 0.282	0.105 0.069	0.047 0.032
Minneart (eq.4.7) S-aspect N-aspect	0.644 0.635	0.616 0.607	0.419 0.387	0.106 0.095	0.048 0.041
Minneart (eq.4.9) S-aspect N-aspect	0.604 0.576	0.581 0.555	0.397 0.351	0.100 0.086	0.046 0.037
SlopeMatch (eq.4.15) S-aspect N-aspect	0.700 0.711	0.682 0.692	0.438 0.421	0.108 0.099	0.063 0.046

spectrum. It tends to decline in the near-infrared region until 1050 nm, where slight gain in reflectance occurs and gives a minor peak at approximately 1090 nm to 1100 nm. The reflectance also shows minor peaks around1800 nm and 2250 nm with
a sharp depression of reflectance around 1950 nm to 2050 nm. This sharp depression is due to strong water absorption bands at these wavelengths. The comparative analysis of different topographic results with *in-situ* observations in Table 4.7 and Table 4.8 shows that all the topographic models underestimate the reflectance in different satellite bands of AWiFS and MODIS except slope matching technique which gives most acceptable results with high accuracy (>96%) and very low relative error (0.2–0.4) for both AWiFS and MODIS images.

4.10 Performance analysis of different topographic corrections

The performance of the topographic corrections can be assessed quantitatively using several possible methods (Riano *et al*., 2003). First method is based on the analysis of changes in spectral characteristics of the training snow samples on the south and north aspects after the

topographic corrections (Civco 1989). Second criterion is based on the graphical analysis of $R_{\lambda T}$ and $R_{\lambda H}$ *with* illumination, IL (Meyer *et al* 1993; Ekstrand 1996). The spectral reflectance on the tilted surface, $R_{\lambda T}$, varies with illumination angle before topographic corrections and should remain almost constant after the corrections have been carried out in satellite data. Both these methods are implemented to test the topographic corrections by different methods. The analysis of changes in the spectral reflectance characteristics of the image is tested before and after the topographic corrections choosing snow samples on south and north aspects for satellite images. Training areas of snow were created on both sunny (south aspect) and shady slopes (north aspect) using normalized difference snow index (NDSI $\geq$ 0.6) in Figures 4.15 to Figures 4.19. Mean values of reflectance on the sunny slopes are expected to decrease while those on the shady side are expected to increase for successful topographic corrections (Law and Nichol 2004). It can be inferred from the quantitative analysis in the Table 4.9 to Table 4.14 that only slope matching method is able to retrieve acceptable values of spectral reflectance of snow samples in shadow areas. It is also observed that this method is applicable to different solar geometry, e.g., varying solar zenith angle and differential illumination condition. Slope matching method is found to be unique and gives the best results (satisfy all the four criteria) for qualitative and quantitative analysis as compared to other methods. Although the values of reflectance marginally decreases on the south aspect and increases on the north aspect by all the methods but the values calculated on the north aspect does not represent to true snow reflectance values when compared with the results of slope matching method. The plot of mean *reflectance* with mean IL after the topographic corrections (Figures 4.20, 4.21) is observed to be invariant by all the methods but quantitative assessment as discussed above fails except for slope matching. The slope matching method is unique among all the methods and is more suitable for Himalayan terrain for qualitative and quantitative assessment for snow cover analysis.

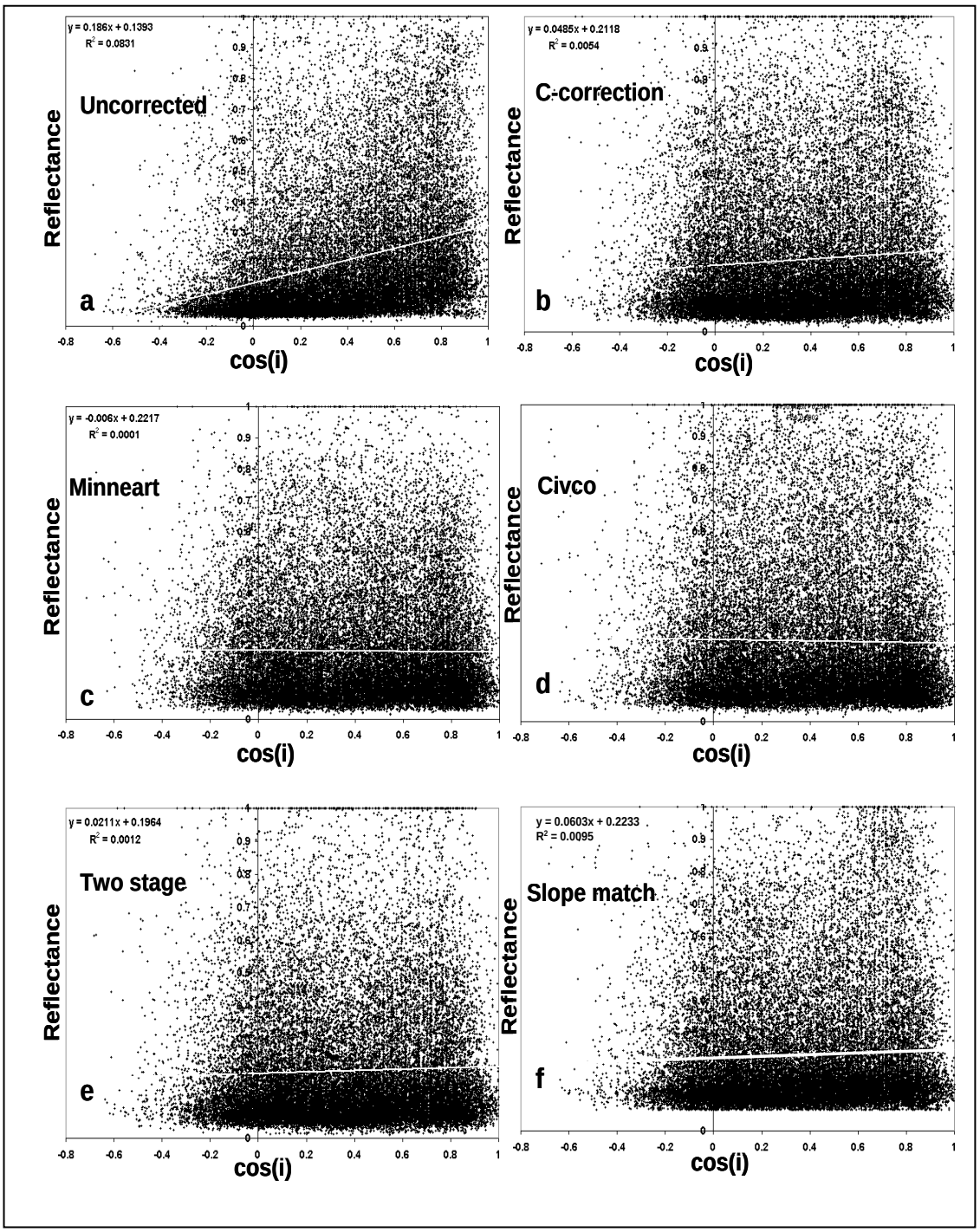

Figure 4.20 Graphical analysis of reflectance in AWiFS band 2 (520–590 nm) *versus* illimunation (IL) before and after the topographic corrections for AWiFS image of 11 December 2005 image.(a) Without topographic corrections, (b) C-correction, (c) Minneart -(equation 5), (d) Civco modified version of cosine correction, (e) two-stage normalization and (f) slope matching method.

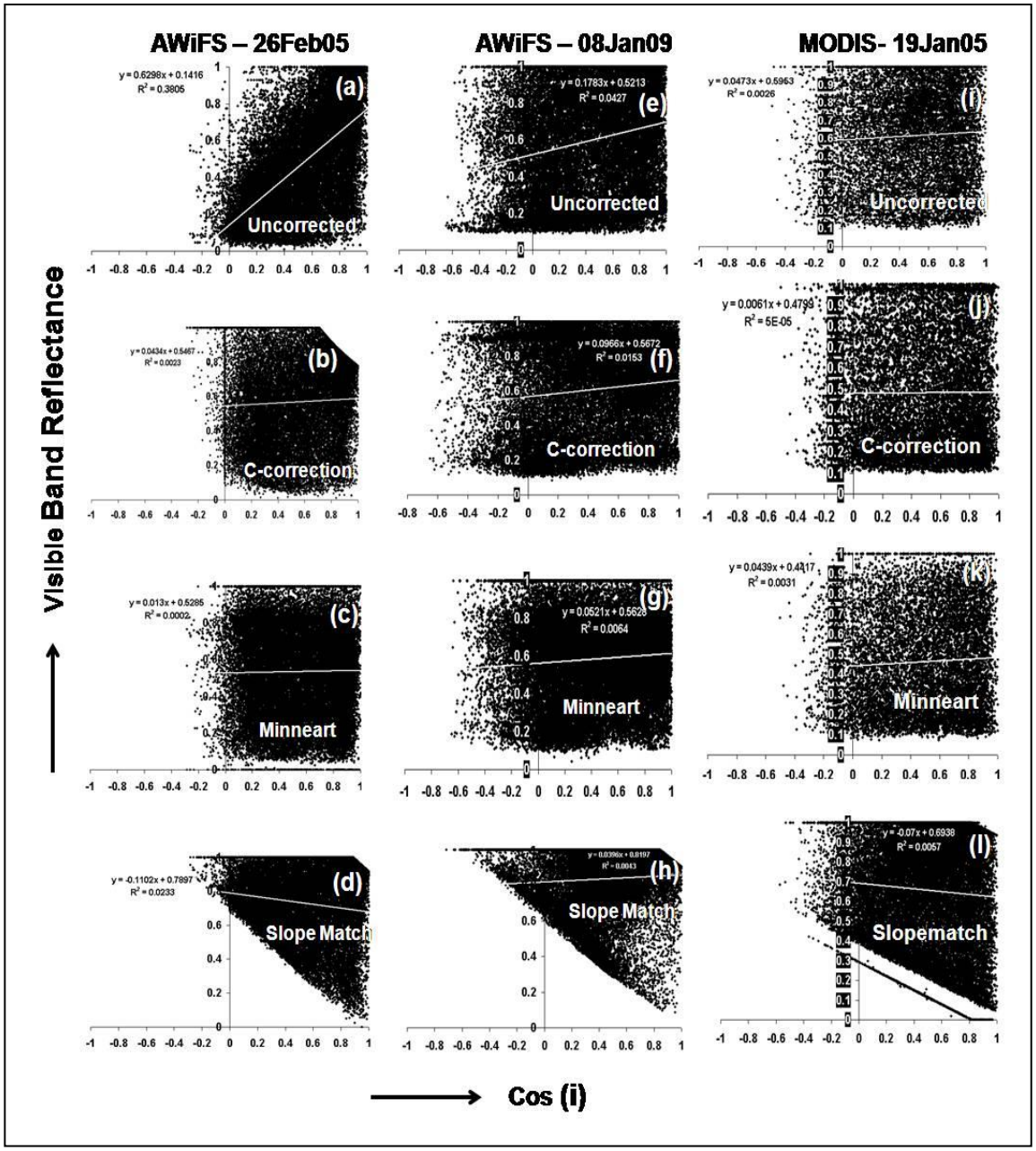

Figure 4.21 Graphical analysis of reflectance in visible band with illumination before and after topographic corrections using different methods (a-d) AWiFS – 26 February 2005 (e-h) AWiFS – 08 January 2009 and (i-l) MODIS – 19 January 2005.

It is also observed that some of topographic correction methods have overestimated and some of topographic correction methods have underestimated the parameters but only slope matching method is unique among all the methods based on validation. Slope matching method has advantages in the true quantitative retrieval of spectral reflectance, especially in shady area, as compared to C-correction, cosine, Minneart, and Single stage and two stage normalization topographic correction methods. Topographic corrections are very useful for

further applications as sub-pixel snow mapping, energy balance studies, climatic modeling, snow melt run-off modeling, avalanche hazard analysis, change detection analysis, etc. In this thesis work, Slope match was selected as a topographic correction method based on results obtained from field observation and visual analysis for change detection analysis on snow cover area of western Himalaya region as discussed in chapter 6.

CHAPTER 5

Snow cover monitoring algorithms

Chapter 5

Performance Analysis of Snow Cover Monitoring Algorithms

5.1 Models and methods of snow cover monitoring.

Different methods and models have been implemented for snow cover monitoring namely visible band reflectance (Kazama and Sawamoto, 1995, Asaoka *et al.*, 2002), Normalized Difference Snow Index (NDSI) (Hall *et al*., 1995) and other methods using sub-pixel classifications based on linear and iterative methods. High resolution images of survey satellites such as IRS, Landsat and SPOT and medium resolution meteorological satellites have been widely used for snow cover monitoring (Singh 2001). The choice of sensor is generally governed by the size of the basin under study and the temporal resolution required. The Landsat MSS images with 80 m resolution have been applied for mapping of snow in basins larger than 10 Km^2 (Rango *et al*., 1985). The data from Landsat TM, SPOT HRV, and IRS - LISS III is much suited for snow cover information of basins as small as 2.5 Km^2. However these sensors have become saturated for snow due to its high reflectance in most of their spectral regions. Furthermore, the revisit time of these satellites varies from 16 to 24 days which limits the utility of their data for winter months in Himalayan terrain (Kulkarni 2003, 2006; Negi *et al*., 2008).

The availability of data from new sensors such as MODIS on board Terra and Aqua satellites and AWiFS on board IRS-P6 in the last 10 years has not only helped us in overcoming the saturation problem due to their high radiometric resolution but facilitated the effective monitoring of large snow covered areas as a result of high temporal resolution and wide swath coverage. However, the data provided from these sensors are at medium spatial resolution ranging from 56m for AWiFS to moderate resolution of 250m, 500m and 1000m for MODIS, which brings the problem of mixed pixels (i.e., pixels containing more than one class). To overcome this problem, a number of techniques for mapping the land cover at sub-pixel level have been developed. These include MLC (Maximum Likelihood Classification), Linear Mixture Modeling (LMM) (Nolin *et.al*., 1993; Rosenthal and dozier, 1996; Painter *et.al*., 1998, 2003; Vikhamar and Solberg, 2002, 2003; Foppa *et.al*., 2004), Artificial Neural Network (ANN) (Foody and Arora, 1997), Decision Tree Classification etc. However, not all these techniques have yet been explored for snow-cover sub-pixel mapping (Foody and Arora, 1996; Foody and Arora, 1997; *Tiwari et al*., 1999; Arora, 1999). The literature

suggests the use of empirical relationships (Kaufman *et al*., 2002, Barton, 2002; Salomonson and Appel, 2004, 2006), using LMM (Nolin et al., 1993; Rosenthal and dozier, 1996; Painter et al., 1993, 2003; Vikhamar and Solberg, 2002, 2003; Foppa *et al*., 2004) and ANN (Simpson and McIntire, 2001), for snow cover mapping at sub-pixel level. The main aim of this chapter is to devise an objective and comprehensive approach for snow cover mapping for precise estimation and distribution of snow class fractions from moderate spatial resolution images. The study has evaluated whether there is an indication in the NDSI that could be used to retrieve the sub-pixel snow information within 500 m MODIS pixels and thereby enhance the potential of NDSI approach in snow cover monitoring without assuming threshold value. The following objectives are implemented:

(a) Sub-pixel snow cover mapping using linear mixture model (LMM) and fuzzy C-means clustering.

(b) Fuzzy c-means clustering algorithm using different norms.

(c) Statistical relationship between snow fraction and normalized difference snow index (NDSI).

(d) Performance analysis of different algorithms for sub-pixel snow mapping.

(e) Validation with AWiFS data and RMSE.

5.2 Methodology

In this thesis, we tested two different sub-pixel classification techniques: Linear Mixture Model (LMM) and Fuzzy c-means Clustering (FCM) using three norms Euclidean norm, Diagonal norm and Mahalonobis norm. Statistical relationships have been developed between the Normalized Difference Snow Index (NDSI) and the fraction of snow-cover at 500-meter grid resolution for different MODIS images. The resultant algorithm is applied for other geographical region and results are validated with AWiFS satellite image.

5.2.1 Study area

The study area comprises of Pir-panjal and Greater Himalaya ranges of North West Himalaya as shown in Figure 1. The brief about different ranges of Himalaya are given in chapter 3. The lower part of the study area is Beas basin from where the Beas River originates and upper part lie in Chenab basin of Himachal Pradesh (Indian Himalaya). Thus being a catchment area of a river it is important to monitor the snow cover for various potential applications. The Beas basin is located in North East (NE) of Kullu district of

Himachal Pradesh, India. The study area is extending from latitude 32.19° N to 33.05° N and longitude 76.35° E to 77.64° E. The altitude varies from 1100 m to 6457 m with a mean altitude of 4376 m. The entire basin has three permanent field observatories of Snow and Avalanche Study Establishment (SASE) located within basin at varying altitudes, i.e. Bahang (2039 m), Solang (2480 m) and Dhundi (3050 m).

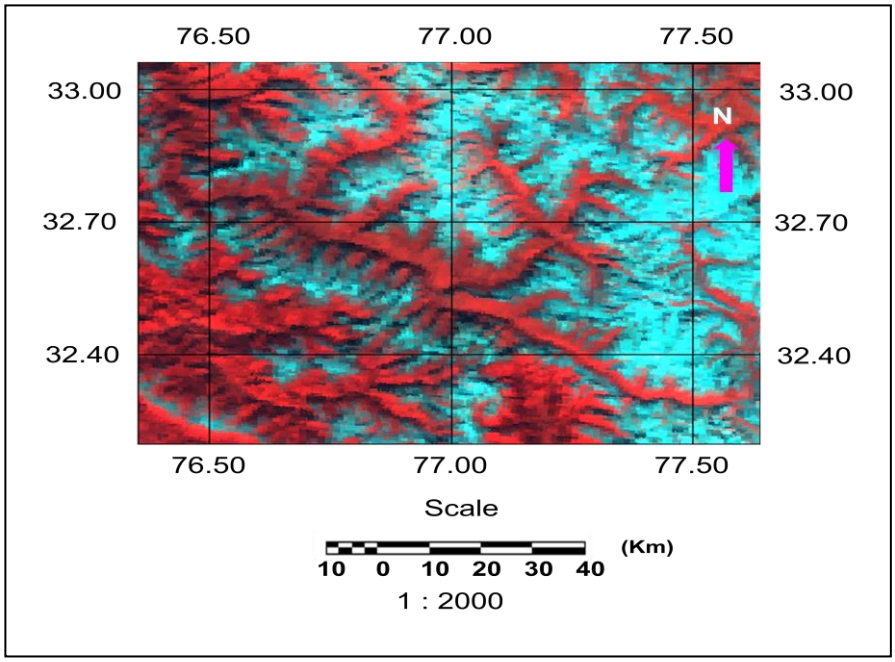

Figure 5.1: Study area on MODIS image

5.2.2 Satellite data used

MODIS sensor data of Terra satellite has been used for monitoring of the snow cover. Seven scenes between the period from 01 October 2008 and 13 April 2009 comprising the complete winter season were selected for analysis. ERDAS IMAGINE 8.7 and SnowFrac software has been used for snow cover analysis using different sub-pixel classification techniques. SnowFrac software was earlier developed at Snow and Avalanche Study Establishment (SASE), Chandigarh India. The general methodology adopted for this analysis is shown in Figure 5.2.

5.2.3 Calculation of reflectance values:

The received MODIS image data is of raw digital number (DN) values The DN values do not provide the correct information for comparative analysis (Negi et al 2009). Thus the DN values from the satellite data is converted into reflectance values, using the following reflectance model:

$$R_\lambda = \frac{SI\,(reflectance_{scale} - reflectance_{offset})}{\cos Z} \qquad (5.1)$$

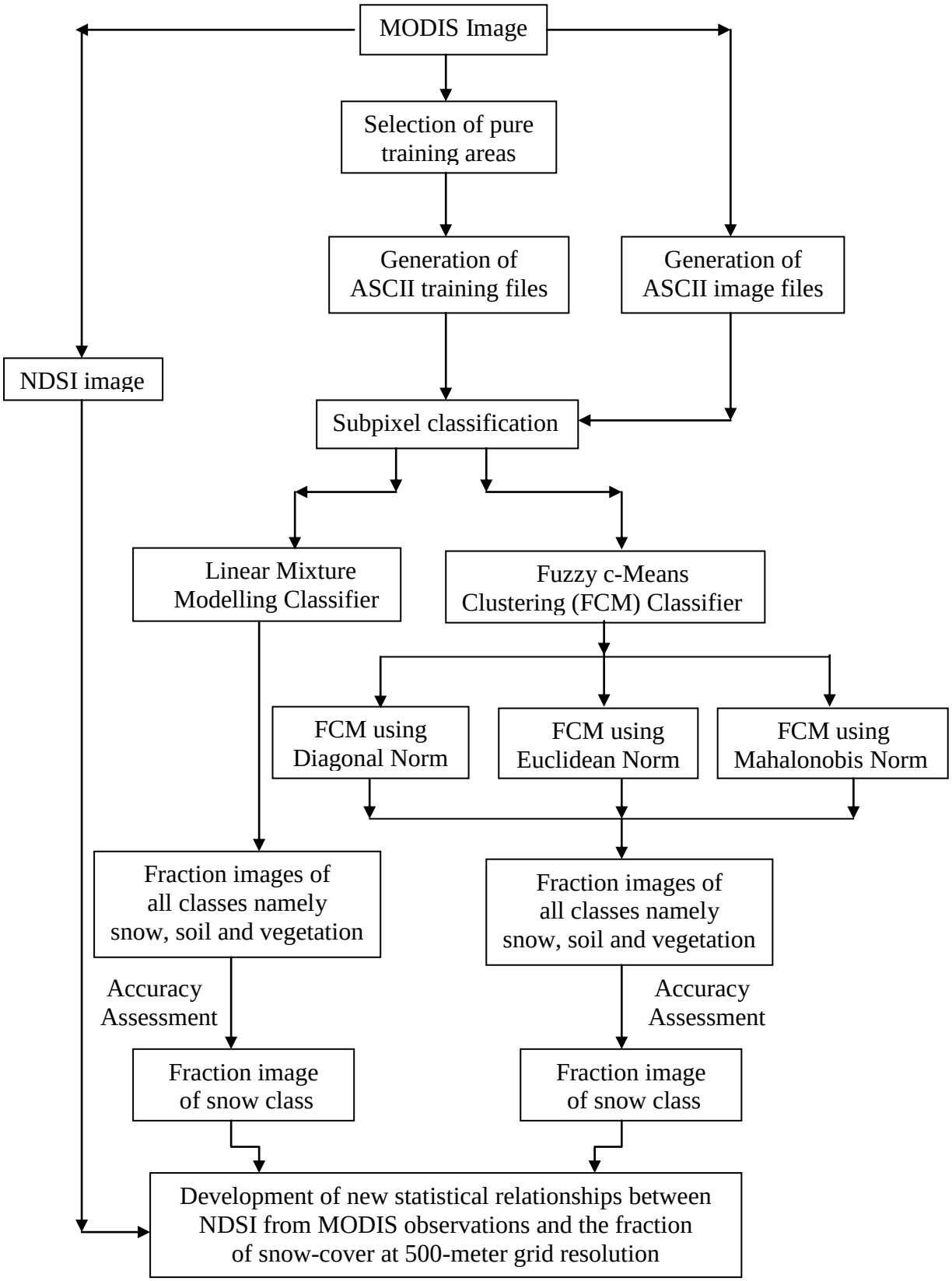

Figure 5.2: Flowchart of the general methodology for Sub-pixel Classification

where SI is the scaled integer image and Z is the solar zenith angle. The related scales and offsets obtained from MODIS sensor Level 1B (L1 B) data set in band 1 to 7 are given in Table 5.1.

Table 5.1: The bands, related scales and offsets obtained from MODIS Level 1B (L1B) dataset

MODIS Sensor Bands	reflectance_scales	reflectance_offsets
1	$5.11591*10^{-5}$	0
2	$3.18419*10^{-5}$	0
3	$3.03671*10^{-5}$	0
4	$2.97935*10^{-5}$	0
5	$3.37758*10^{-5}$	0
6	$3.22512*10^{-5}$	0
7	$2.62223*10^{-5}$	0

5.2.4 Selection of end members

Three end members snow, soil and vegetation are considered as three classes in a MODIS pixel. Soil/rocks are merged in one class due their similar spectral characteristics. The end member spectra corresponding to these classes have been obtained from the average spectral response of pure pixels of each class in the image. The training areas belonging to the pure pixels of these classes have been demarcated on the image using ERDAS Imagine. Assistance from the reflectance values from available field data (Figure 5.3) has been taken to demarcate the classes.

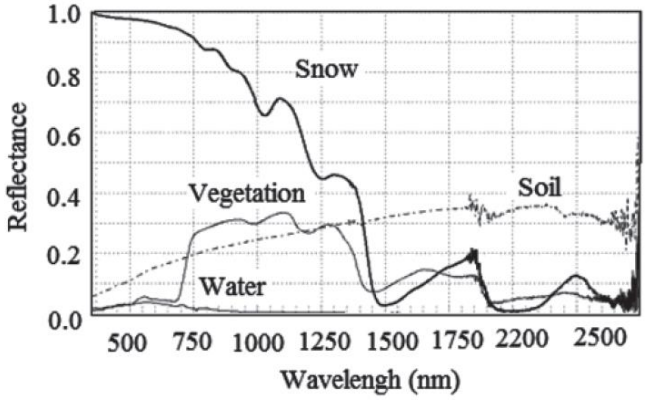

Figure 5.3: Field observations of spectral reflectance characteristics of different land covers.

5.2.5 Normalized difference snow index (NDSI)

Snow has high reflectance at visible wavelength band (0.4 μm – 0.7 μm) and low reflectance at short wave infrared wavelengths (1.55 μm -1.75 μm). These properties are used

to distinguish snow from other surface types (Hall *et al.*, 1995). For MODIS data NDSI is estimated using following formula:

$$NDSI = \frac{Band\,4 - Band\,6}{Band\,4 + Band\,6} \quad (5.2)$$

The spectral range of MODIS band 4 is 0.545 μm - 0.565 μm and that of band 6 is 1.628 μm -1.652 μm. In this snow-mapping algorithm, snow is mapped in a pixel when the NDSI is ≥ 0.4. A pixel that is approximately 50% or more covered by snow is considered as snow-covered pixel (Hongen Zhang *et al.*) Snow under shadow and low illumination conditions where the reflectance signal is low can be retraced using NDSI. However, the NDSI cannot provide fractional snow cover information thus it has limitation in use in images having moderate spatial resolution. In such cases sub-pixel techniques are having better utility.

5.2.6 Linear mixture model

Traditionally, the linear spectral mixing model has been widely used to calculate the percentages of several individual surface components contained in each pixel of a remote sensing image (*Thomos et al*., 1996). The LMM assumes that the spectral response of an individual pixel (i.e. the pixel reflectance, X) is a linear sum of the mean spectral responses of its components, R (i.e. land cover classes) weighted by their relative proportions, f, on the ground (Thomas *et al.*, 1996). Mathematically, the model for a pixel may be expressed as,

$$X_i = \sum_{j=1}^{c} f_j \, R_{ij} + e_i \quad (5.3)$$

where X_i is the spectral response of *ith* pixel, *c* is the number of end members, f_j is the fraction of *jth* class in a pixel, R_{ij} is the end member spectral representing the mean class spectral response of *jth* class in *ith* band, and e_i is the error term for *ith* band. The limitation here is that the number of classes should be one less than number of bands used (Vikhamar *et al*., 2003). Two more constraints are also generally added and are given by,

$$\sum_{j=1}^{c} f_j = 1 \quad (5.4)$$

This constraint states that the class fractions of pixels cannot add up to more than 100%, and,

$$f_j \geq 0 \quad \text{for all j land cover classes} \quad (5.5)$$

This constraint states that all the class proportions of mixed pixels are nonnegative.

5.2.7 Fuzzy c-means clustering

The FCM algorithm is one of the most widely used fuzzy clustering algorithms. FCM, is an iterative clustering method that may be employed to partition pixels of remote sensing image into different class membership values. The key is to represent the similarity that a pixel shares with each cluster with a function (membership function) whose values lie between zero and one. Each pixel will have membership in every cluster. Memberships close to unity signify a high degree of similarity between the pixel and that cluster (Bezdek *et al*., 1984). The net effect of such a function for clustering is to produce fuzzy *c*-partitions (*U*) of a given data. A fuzzy *c*-partition of the data is the one which characterizes the membership of each pixel in all the clusters by a membership function which ranges from zero to one. Additionally, the sum of the memberships for each pixel must be unity. This is achieved by minimizing the generalized least-square error objective function given below (Mohanad Alata *et al*., 2008)

$$J_m(U,V) = \sum_{i=1}^{N}\sum_{j=1}^{c} \mu_{ij}^{m} \left\|X_i - v_j\right\|^2 \quad (5.6)$$

subject to constraints,

$$\sum_{j=1}^{c} \mu_{ij} = 1 \quad \text{for all i} \quad (5.7)$$

$$\sum_{j=1}^{c} \mu_{ij} > 0 \quad \text{for all j} \quad (5.8)$$

$$0 \leq \mu_{ij} \leq 1 \quad \text{for all i,j} \quad (5.9)$$

where X_i is the vector denoting spectral response of *ith* pixel (i.e. a vector of spectral response of a pixel in various bands of a multi-spectral remote sensing image), *V* is the collection of vectors of cluster centers, v_j, μ_{ij} are class membership values of a pixel (members of fuzzy *c*-partition matrix) , *c* and N are the number of clusters and pixels respectively, *m* is the weighting exponent ($1 < m < \infty$), which controls the degree of fuzziness, $\left\|X_i - v_j\right\|_A^2$ is the squared distance (d_{ij}) between X_i and v_j and is given by,

$$d_{ij}^2 = \left\|X_i - v_j\right\|_A^2 = (X_i - v_j)^T A (X_i - v_j) \quad (5.10)$$

where A is the weight matrix.

Weighted exponent *m* controls the relative weights placed on each of the squared error d_{ij}^2 . At m=1, At *m* = 1, partitions that minimize J_m become increasingly hard and as *m* tends to

reach ∞, partitions that minimize J_m become increasingly fuzzy. Consequently, increasing *m* tends to degrade the membership towards the fuzziest state. Each choice of *m* will generate one FCM solution keeping all other parameters fixed. No theoretical or computational evidence provides an optimal *m*. The best strategy for selecting *m* is experimental. The weight matrix *A.* controls the shape of the optimal clusters. Amongst a number of *A*-norms, three namely Euclidean, Diagonal and Mahalonobis norm, each induced by specific weight matrix, are widely used and are given as (Bezdek, 1981),

$$A = I \quad \text{Euclidean Norm (EN)} \tag{5.11}$$

$$A = D_j^{-1} \quad \text{Diagonal Norm (DN)} \tag{5.12}$$

$$A = C_j^{-1} \quad \text{Mahalonobis Norm (MN)} \tag{5.13}$$

where *I* is the identity matrix, *Dj* is the diagonal matrix having diagonal elements as the eigen values of the variance covariance matrix, *Cj*. When the diagonal norm is used, each dimension is effectively scaled *via* the eigen values. The Euclidean norm is the only choice for which extensive experience with the data is available.

The fuzzy *c*-partition is obtained through an iterative process of optimization using the following two equations. The cluster centers are updated by,

$$v_j = \frac{\sum_{i=1}^{N} \mu_{ij}^{m} x_i}{\sum_{i=1}^{N} \mu_{ij}^{m}} \tag{5.14}$$

and the class membership matrix μ_{ij} is obtained by

$$\mu_{ij} = \frac{1}{\sum_{k=1}^{C} \left\langle d_{ij}^2 | d_{ik}^2 \right\rangle^{\frac{1}{m-1}}} \tag{5.15}$$

$$\text{Where} \quad d_{ik}^2 = \sum_{j=1}^{c} d_{ij}^2 \tag{5.16}$$

The class membership values of a pixel denote the class fractions or the sub-pixel snow-cover.

5.2.8 NDSI and its use for snow fraction retrieval

Although the sub-pixel classification solved the problem of mixed pixels, but the information of snow under shadow cannot be retraced with the help of sub-pixel classification (Solomonson *et al*., 2004). As discussed earlier NDSI technique can be used to retrace snow under mountain shadow, but one need to set the threshold value properly, which

is a very critical task (Solomonson *et al*., 2006). Therefore, a new statistical relationship is developed between NDSI and sub-pixel fraction snow covered image. Statistical relationships between the NDSI from MODIS observations and the fraction of snow-cover at 500-meter grid resolution were tested on Himalayas.

5.2.9 Accuracy assessment

Classification is not complete unless assessment of accuracy has been performed. The accuracy assessment is a critical step in any mapping process and thus is an essential component, which allows a degree of confidence to be attached to maps for their effective use. Various measures of accuracy assessment evaluating the sub-pixel classification outputs are the root mean square errors, Euclidean distances etc. The root mean square error (RMSE) is estimated using the following equation.

$$RMSE = \sum_{i=1}^{M} \sqrt{\frac{1}{M} \sum_{j=1}^{n} \left(\frac{e_i}{n}\right)^2} \qquad (5.17)$$

where *M* is the number of bands and n is the number of pixels.

5.3 Results and Discussion

MODIS sensor data of Terra satellite are used for monitoring of the study area. The seven almost cloud free scenes of dates 01 October 2008, 10 November 2008, 02 December 2008, 28 January 2009, 26 February 2009, 16 March 2009 and 13 April 2009 were selected for present work. All these satellite images are shown in Figure 5.4. The DN values from the satellite data were converted into reflectance values using equation 5.1. The calculated zenith angles for all the seven images are shown in Table 5.2.

Table 5.2: Estimated values of zenith angle of different dates MODIS images

MODIS images obtained on dates	**Elevation angle in degree**	**Zenith angle (Z) = 90^o – Elevation Angle**
01 October 2008	55.7	34.3
10 November 2008	42.1	47.9
02 December 2008	36.7	53.3
28 January 2009	38.9	51.1
26 February 2009	47.6	42.4

16 March 2009	55.7	34.3
13 April 2009	66.3	21.7

5.3.1 Snow Cover monitoring using NDSI

NDSI images of MODIS using equation 5.2 are shown in Figure 5.5. The snow cover area calculated using NDSI is shown in Table 5.3. The MODIS pixel is mapped as snow if NDSI>=0.4 and Reflectance in near infrared band >0.10.

Table 5.3: Snow covered areas (Km^2) obtained using NDSI technique

MODIS images obtained on different dates	**Snow covered areas (Km^2) obtained using NDSI technique**
01 October 2008	2710.6
10 November 2008	1225.93
02 December 2008	506.81
28 January 2009	4909.62
26 February 2009	6931.25
16 March 2009	7133.68
13 April 2009	7187.25

5.3.2 Snow covers monitoring using Liner Mixture Model (LMM)

Three classes viz. snow, vegetation and soil are selected as three end members. MODIS band 3 to band 6 are best suited for the extraction of pure spectral signatures of these classes. The band 3 and band 4 are visible bands (wave length of 459 nm - 479 nm and 545 nm - 565nm respectively). Band 5 is near infrared band (wavelength1230 nm - 1250 nm) and band 6 is short wave infrared (1628 nm -1652 nm). Snow has high reflectance in visible band and low reflectance in shortwave infrared band. Vegetation has high reflectance in near infrared band and low reflectance in shortwave infrared band. The reflectance of soil goes on increasing from visible to shortwave infrared band. Fractional snow covered images obtained using LMM methods are shown in Figure 5.6. The area covered by snow using LMM has been estimated and is shown in Table 5.4.

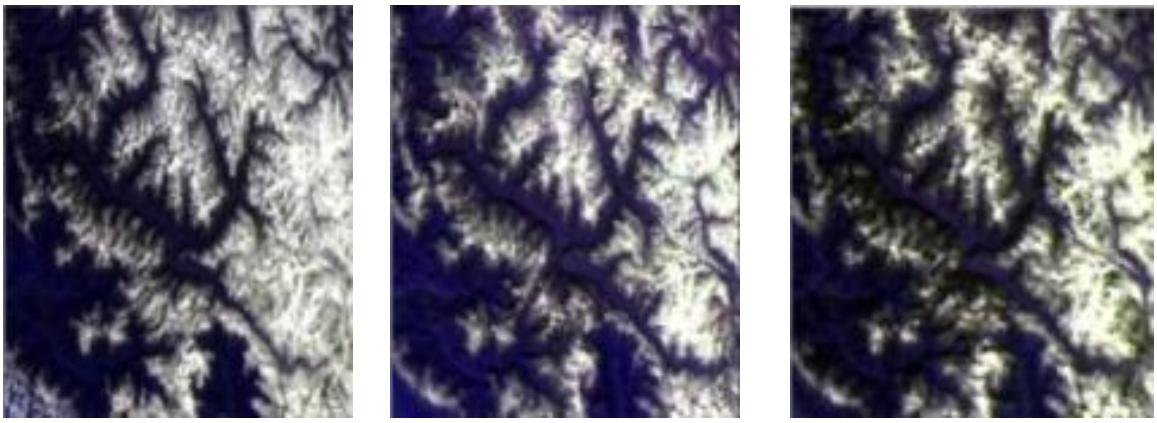

(a) **(b)** **(c)**

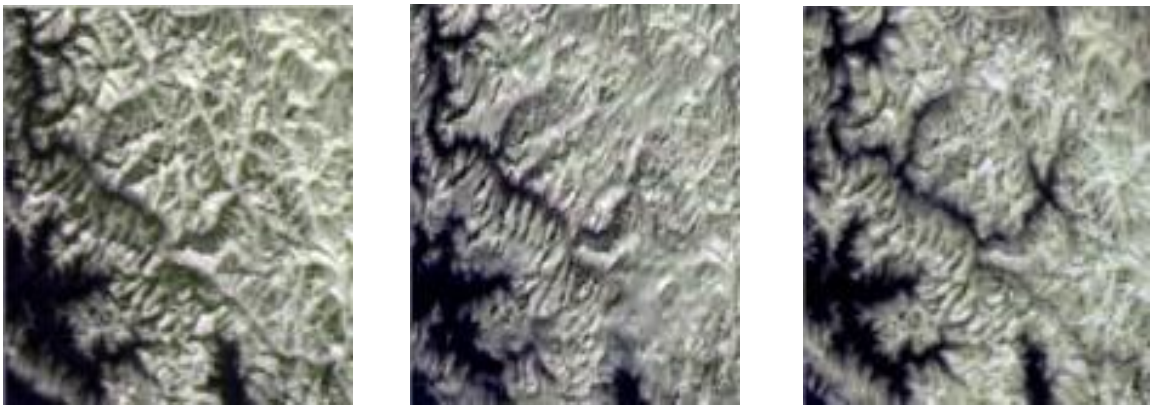

(d) **(e)** **(f)**

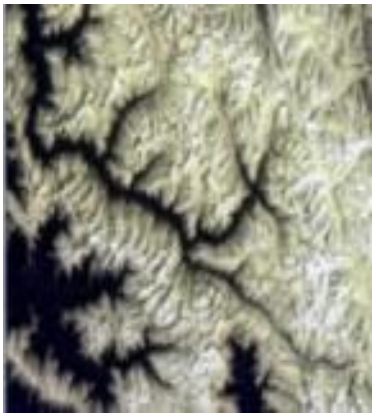

(g)

Figure 5.4: MODIS Images obtained on dates (a) 01 October 2008. (b) 10 November 2008, (c) 02 December 2008, (d) 28 January 2009, (e) 26 February 2009, (f) 16 March 2009, (g) 13 April 2009.

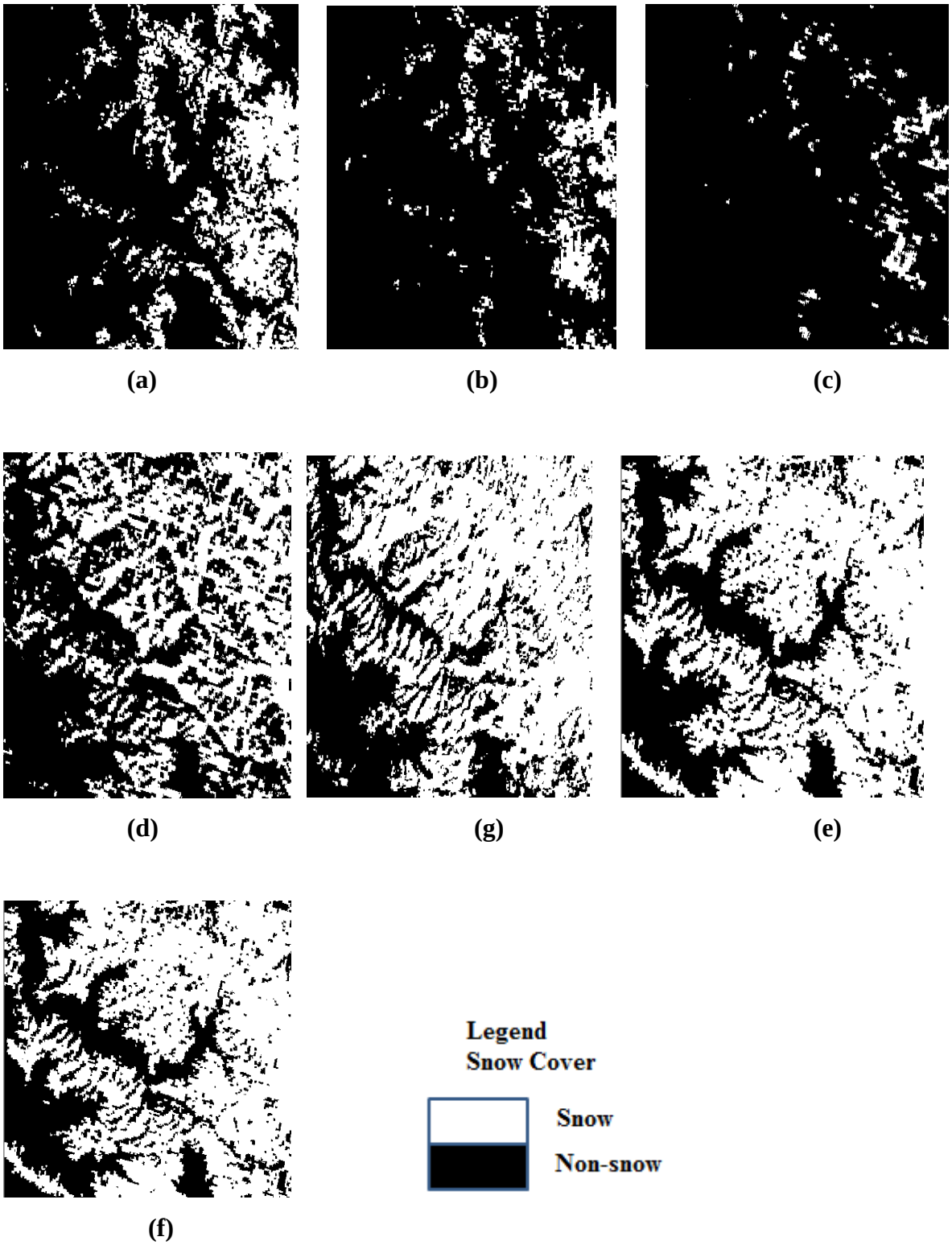

Figure 5.5: MODIS NDSI images of dates (a) 01 October 2008, (b) 10 November 2008 (c), 02 December 2008, (d) 28 January 2009, (e) 26 February 2009, (f) 16 March 2009, (g) 13 April 2009.

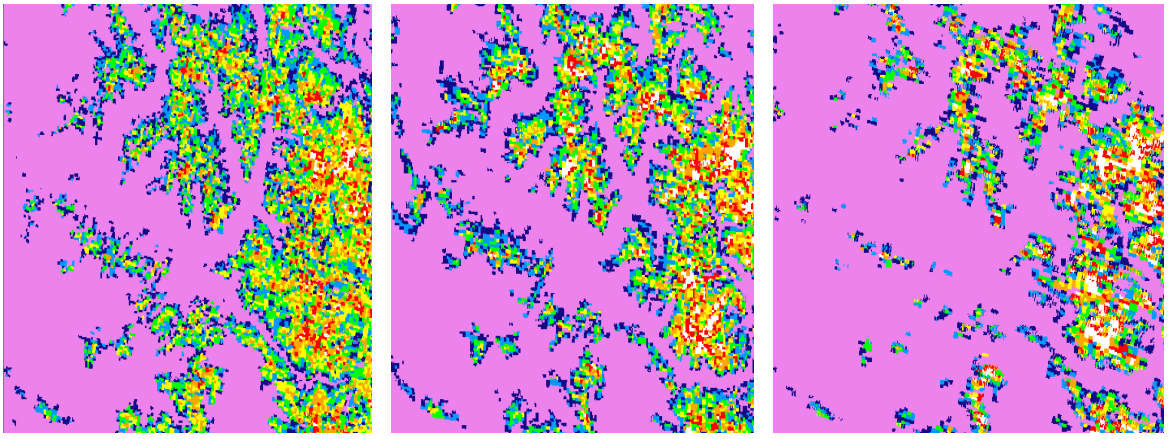

(a) (b) (c)

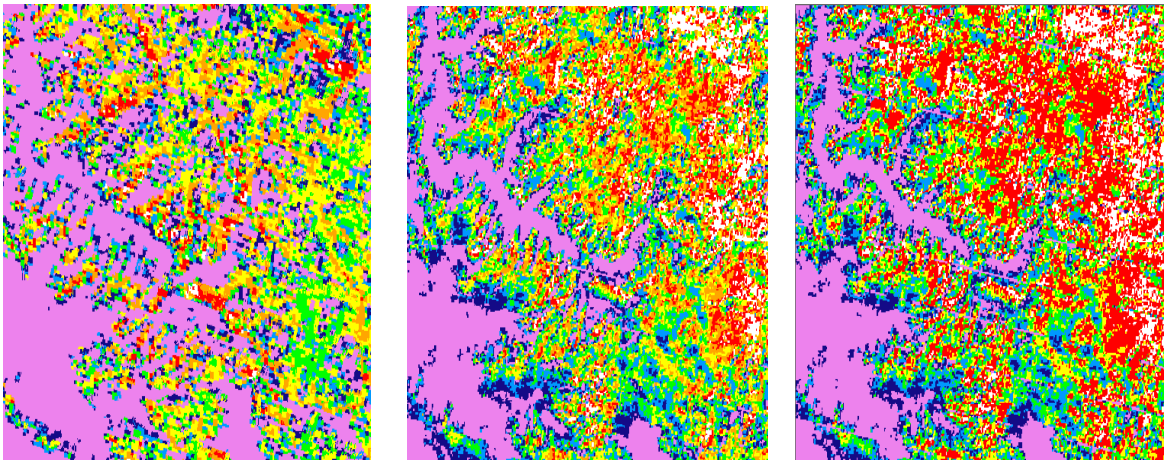

(d) (e) (f)

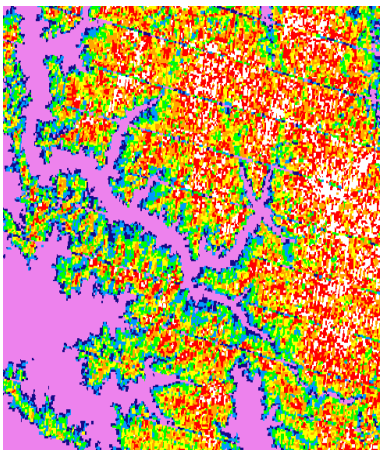

(g)

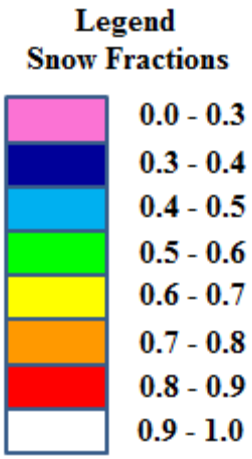

Figure 5.6: MODIS snow fraction images obtained using LMM method of dates (a) 01 October 2008, (b) 10 November 2008, (c) 02 December 2008, (d) 28 January 2009, (e) 26 February 2009, (f) 16 March 2009, (g) 13April 2009.

Table 5.4: Area covered by snow when images are classified using LMM.

Images obtained on dates	Snow covered area (km^2)
01 October 08	3886.26
10 November 08	3837.51
02 December 08	2619.75
28 January 09	5062.06
26 February 09	6558.53
16 March 09	6852.33
13April 09	6859.45

5.3.3 Snow cover monitoring using Fuzzy c-means clustering

Fractional snow covered images obtained using FCM method using the selected three different norms are shown in Figures 5.7 – 5.9. Area covered by snow in Km^2 when the images are classified with FCM using Diagonal norm, Euclidean norm and Mahalonobis norm are given in Table 5.5 .

Table 5.5: The area covered by snow when images are classified with FCM using DN, EN, MN

Images obtained on dates	Snow covered area in Km^2		
	FCM using DN	FCM using MN	FCM using EN
01 Oct08	3229.45	4872.3	2941.74
10Nov 08	2729.55	6001.91	2422.68
02 Dec 08	2108.17	3586.57	2049.93
28 Jan 09	5209.34	7685.25	6456.93
26 Feb 09	6406.23	5606.78	6484.9
16 Mar 09	7241.85	6352.25	7301.12
13 Apr 09	6971.87	6185.85	6940.17

5.4 Development of statistical relationship between NDSI and sub-pixel snow fraction retrieval (SFRA)

An ordinary least squares regression approach was used to derive linear relationships between and NDSI corresponding to 500 m MODIS pixels for all LMM and FCM

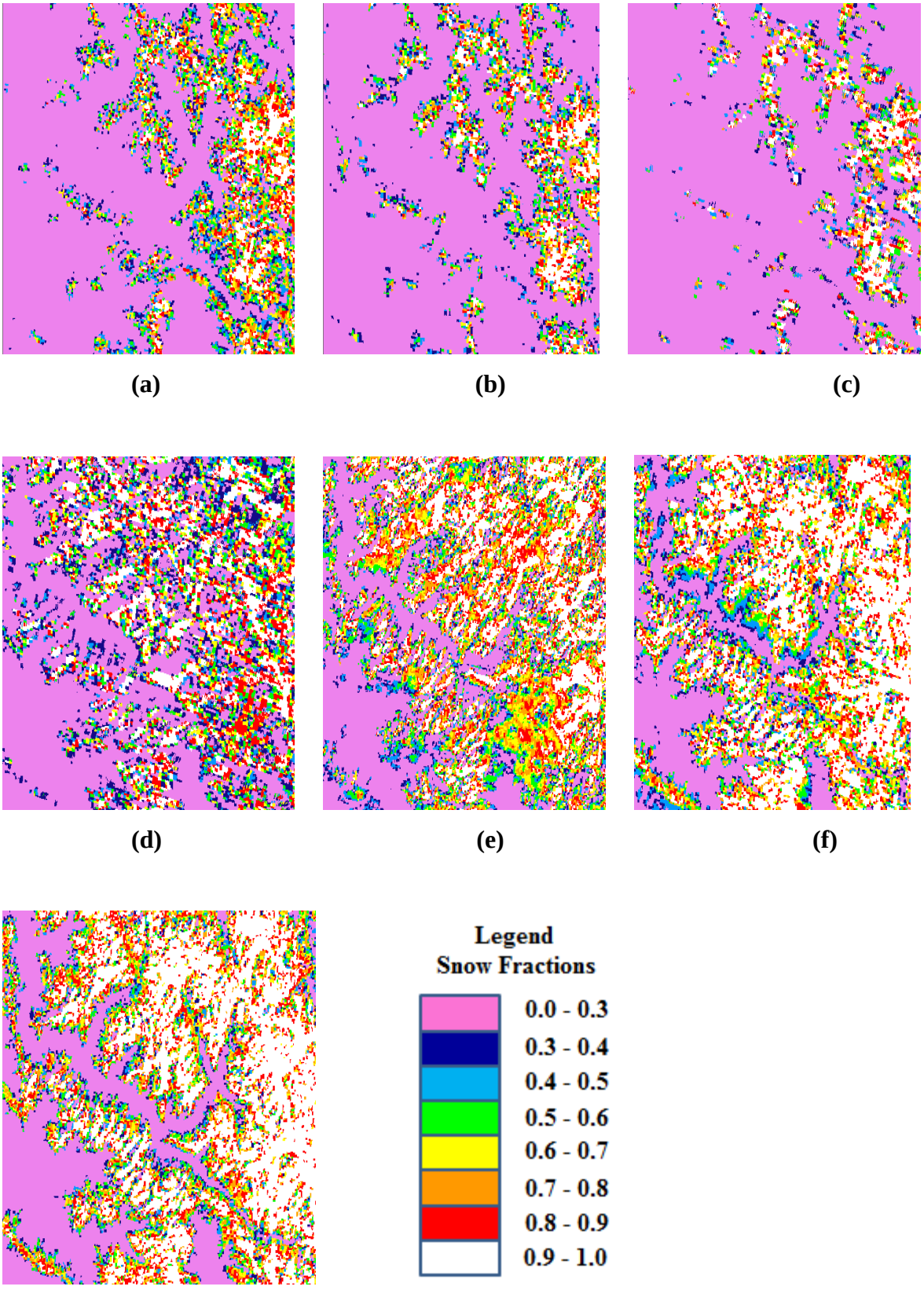

Figure 5.7: MODIS snow fraction images obtained using FCM (Diagonal Norm) method on dates (a) 01 October 2008 (b), 10 November 2008, (c) 02 December 200, (d) 28 January 2009, (e) 26 February 2009, (f) 16 March 2009, (g) 13April 2009.

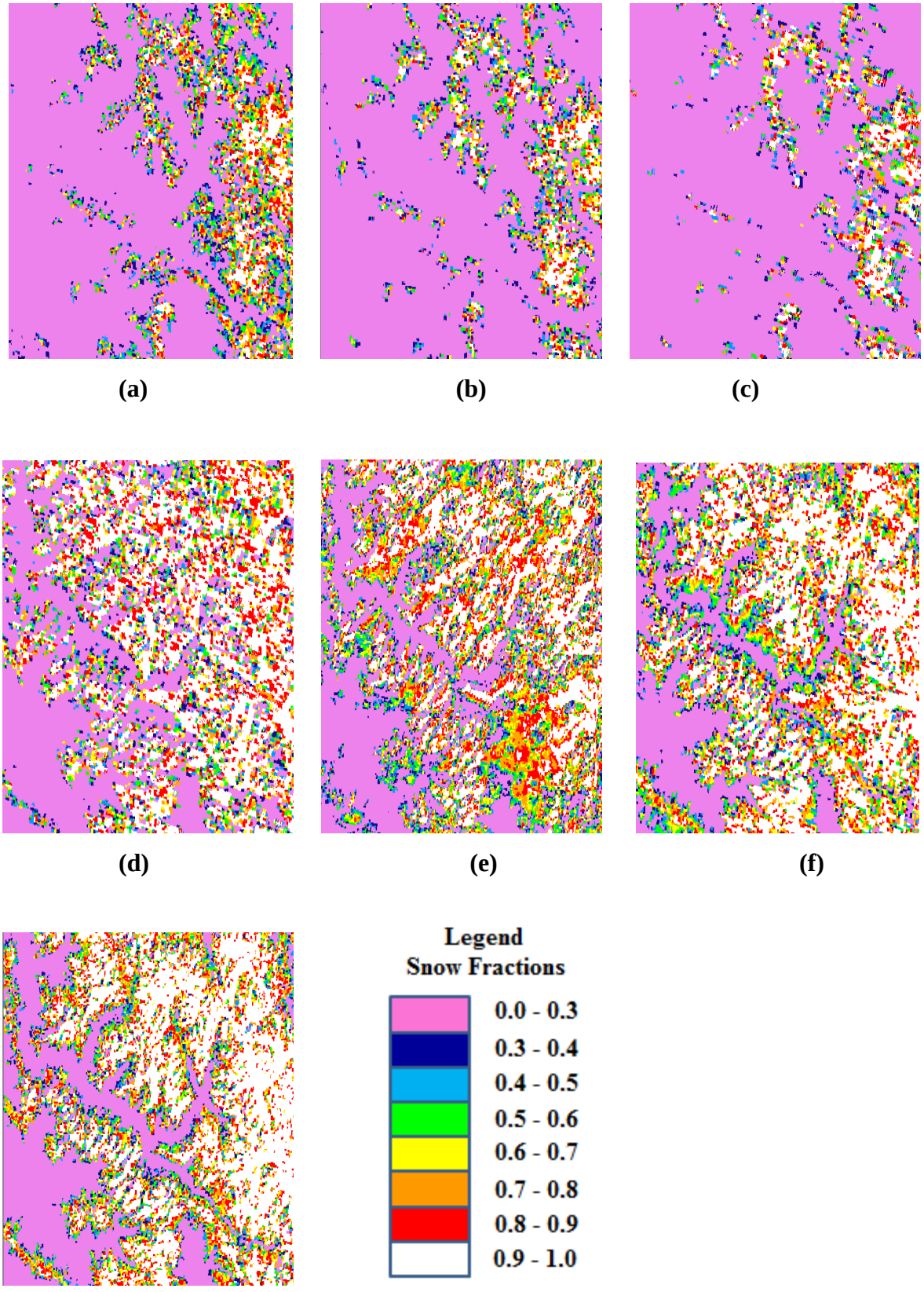

Figure 5.8: MODIS Snow fraction images obtained using FCM (Euclidean Norms) method on dates (a) 01 October 2008 (b) 10 November 2008 (c) 02 December 2008 (d) 28 January 2009 (e) 26 February 2009 (f) 16 March 2009 (g) 13April 2009

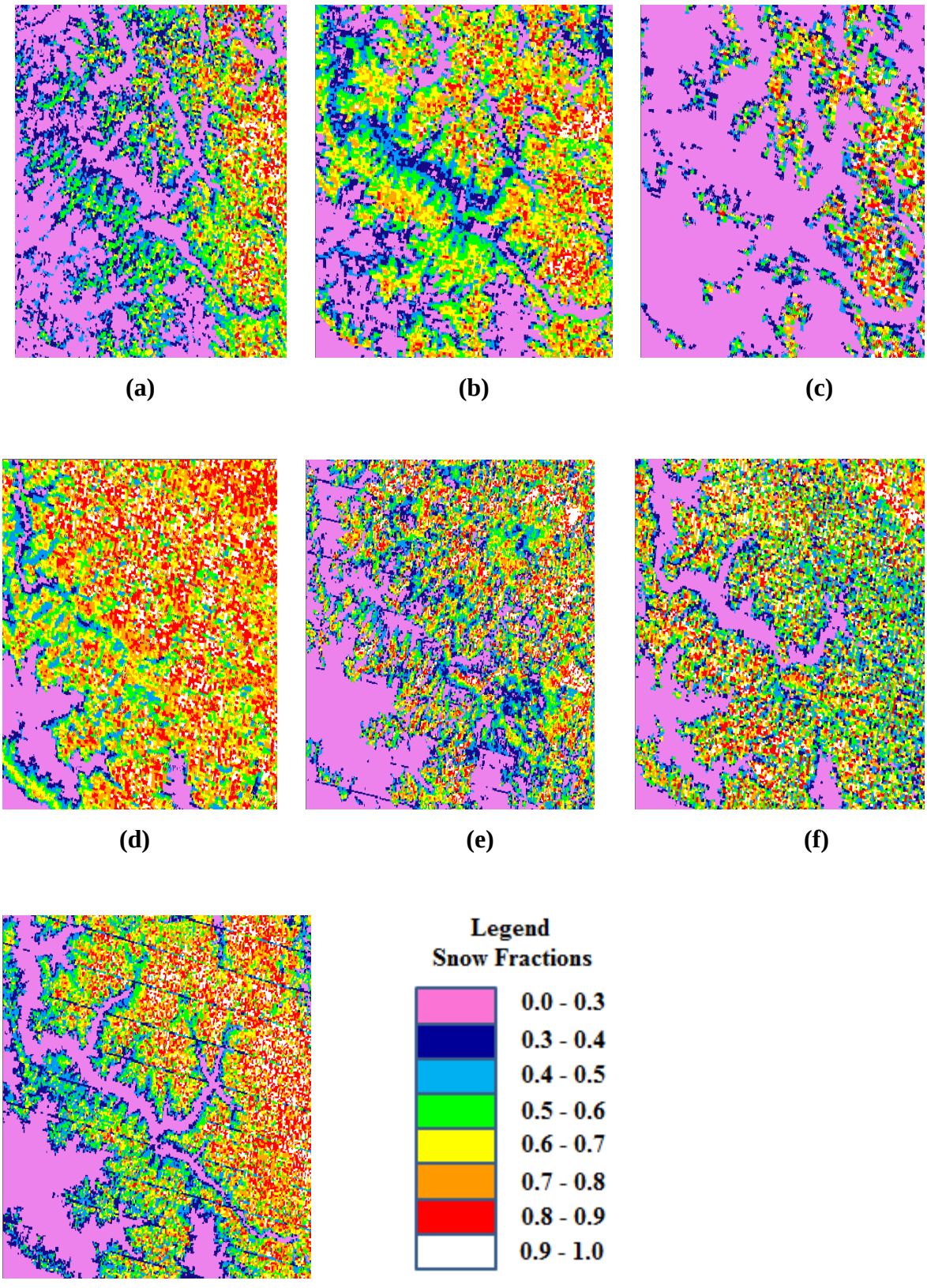

Figure 5.9: MODIS snow fraction images obtained using FCM (Mahalonobis Norms) method on dates (a) 01 October 2008 (b) 10 November 2008 (c) 02 December 2008 (d) 28 January 2009 (e) 26 February 2009 (f) 16 March 2009 (g) 13 April 2009

methods. 2-D scatter plots (Figure 5.10 to Figure 5.13) of SFRA versus NDSI estimated from MODIS reflectance image were examined for all the methods. SFRA generally serves well as the dependent variable and NDSI as the independent variable. The specific regression relationships achieved for SFRA versus NDSI for all MODIS images using different methods are given in the Table 5.6. This table also shows the average (universal) relationships for each of the methods. The values of correlation coefficients of regression equation are given in Table 5.7. It is seen from the comparative analysis of different sub-pixel classification techniques that highest correlation is obtained for FCM methods with Diagonal and Euclidean norms as shown in Figure 5.11 and Figure 5.12. The calculated snow covered areas using average equations obtained with different methods are given in Table 5.8. The average regression equation in Table 5.6 are used directly for automated snow cover fraction in 500 m MODIS pixels and the results are given in the Figures 5.14 to Figures 5.17.

Table 5.6 Statistical relationship between NDSI and fraction of snow cover at 500m grid

MODIS images obtained on dates	**Equation of regression for snow fraction obtained using LMM**	**Equation of regression for snow fraction obtained using FCM (DN)**	**Equation of regression for snow fraction obtained using FCM (EN)**	**Equation of regression for snow fraction obtained using FCM (MN)**
01 Oct-08	1.145NDSI+0.097	1.632NDSI- 0.096	1.724NDSI-0.161	0.806NDSI+ 0.241
10-Nov-08	1.420NDSI+0.126	1.731NDSI+0.010	1.79NDSI- 0.039	1.226NDSI+ 0.217
02-Dec-08	1.805NDSI+0.052	2.123NDSI- 0.012	2.124NDSI-0.016	1.643 NDSI+0.112
28-Jan-09	0.932NDSI+0.089	1.386NDSI- 0.056	1.139NDSI+0.193	0.586NDSI+0.474
26-Feb-09	0.886NDSI+0.156	1.254NDSI- 0.017	1.264NDSI-0.016	0.961NDSI+0.066
16-Mar-09	1.170NDSI+0.030	1.464NDSI- 0.015	1.462NDSI-0.012	0.932NDSI+ 0.165
13-Apr-09	1.015NDSI+0.157	1.512NDSI- 0.054	1.545NDSI–0.070	0.833NDSI+ 0.210
Average (Universal) relationships	**1.196 NDSI +.101**	**1.586 NDSI-.034**	**1.578NDSI–.044**	**0.998NDSI+.212**

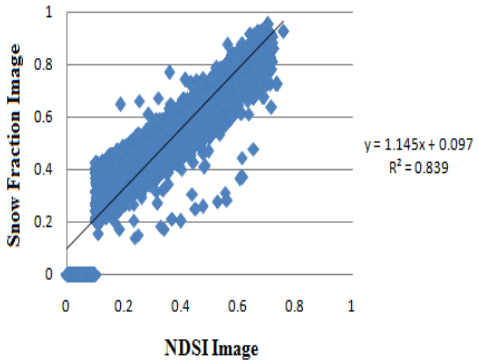

01 October ,2008

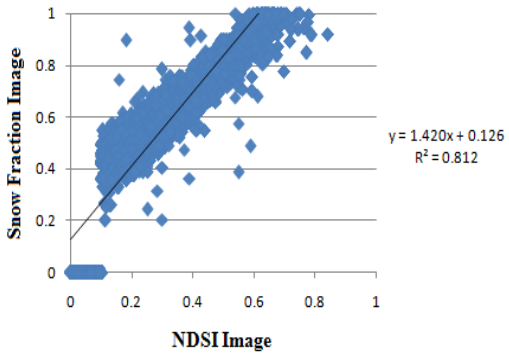

10 November 2008

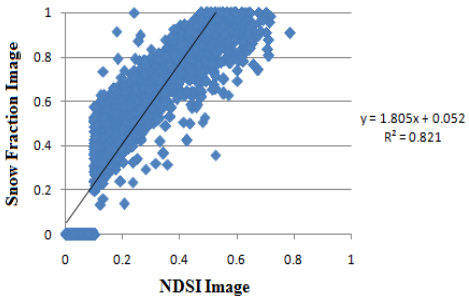

02 December 2008

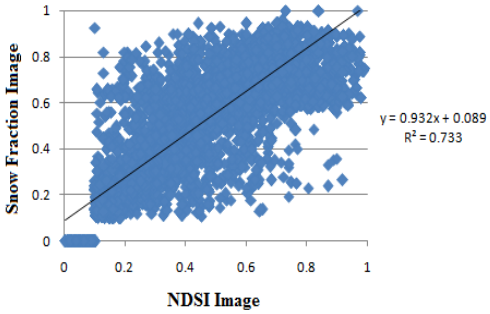

28 January 2009

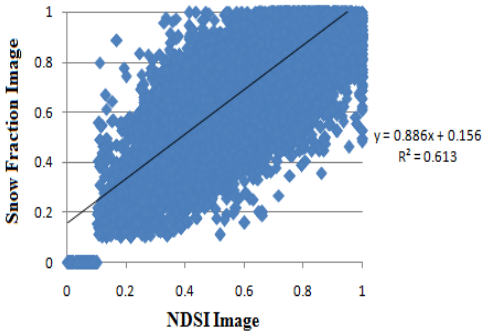

26 February 2009

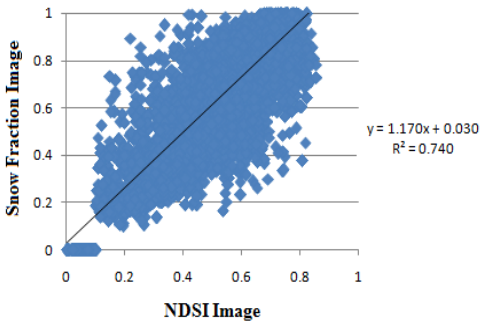

16 March 2009

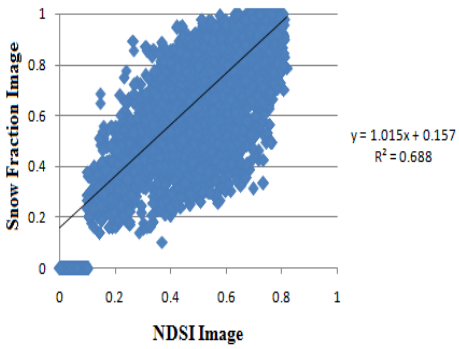

13 April 2009

Figure 5.10: Regression between values of snow fraction image using LMM and NDSI images.

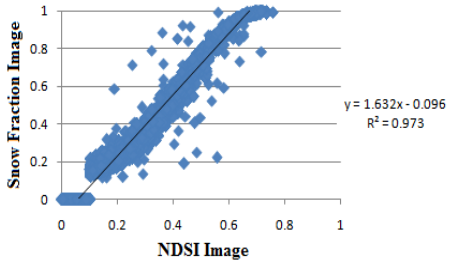

(a) 01October 2008

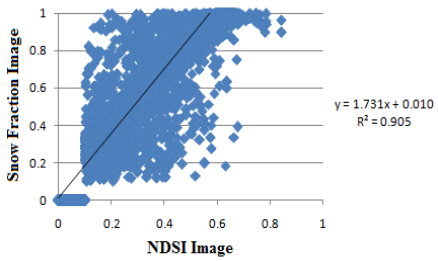

(b) 10 November 2008

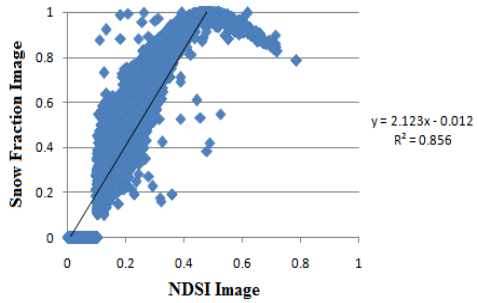

(c) 02 December 2008

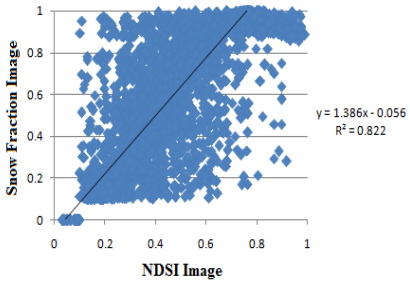

(d) 28 January 2009

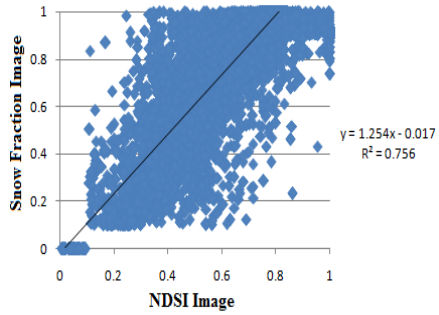

(e) 26 February 2009

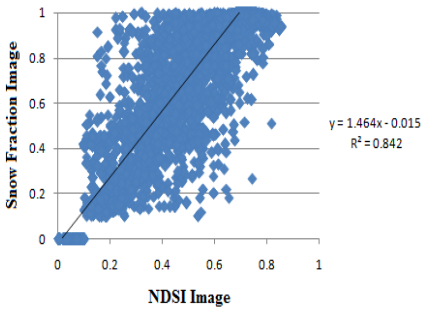

(f) 16 March 2009

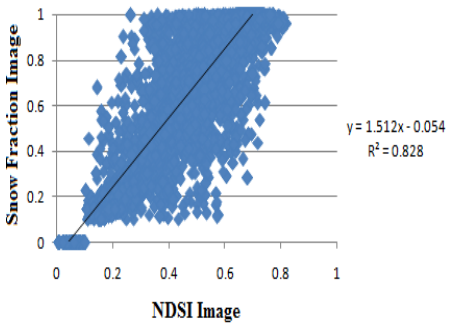

(g) 13April 2009

Figure 5.11: Regression between values of snow fraction image (FCM using DN) and NDSI images.

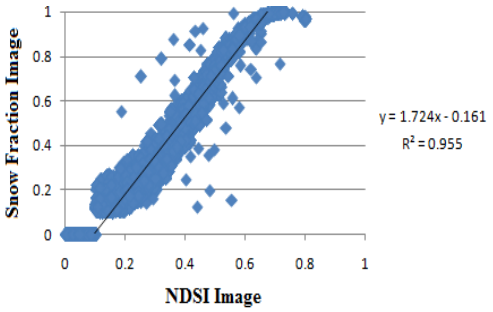

(a) 01October 2008

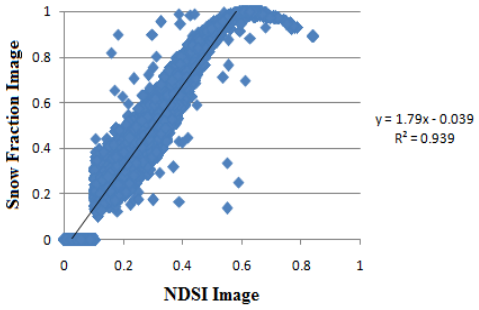

(b) 10 November 2008

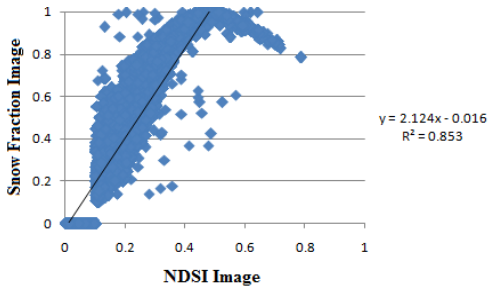

(c) 02 December 2008

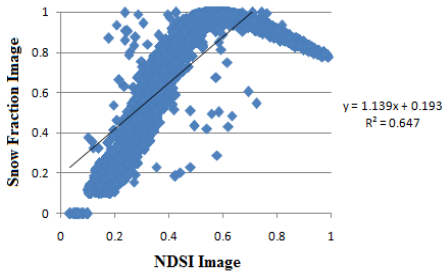

(d) 28 January 2009

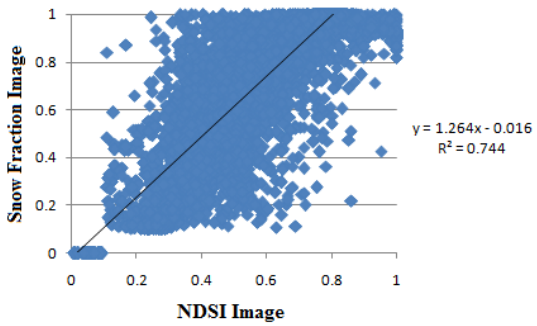

(e) 26 February 2009

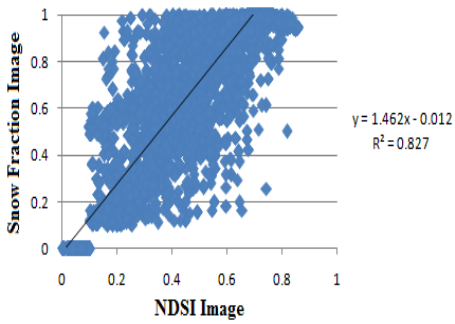

(f) 16 March 2009

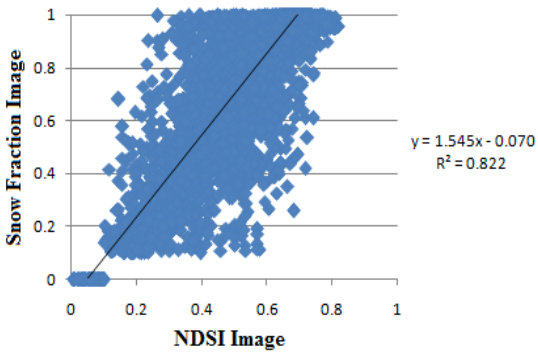

(g) 13April 2009

Figure 5.12: Regression between values of snow fraction image (FCM using EN) and NDSI image.

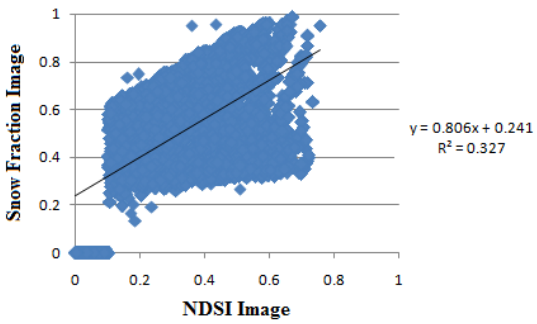

(a) 01October 2008

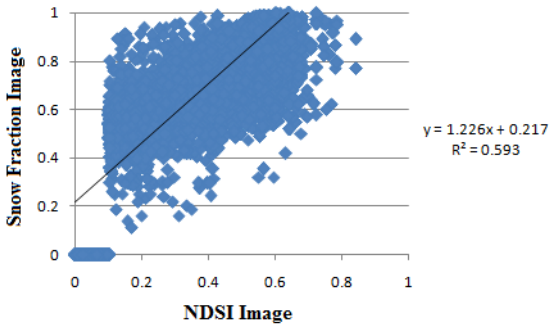

(b) 10 November 2008

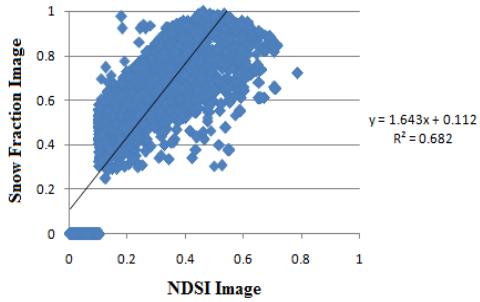

(c) 02 December 2008

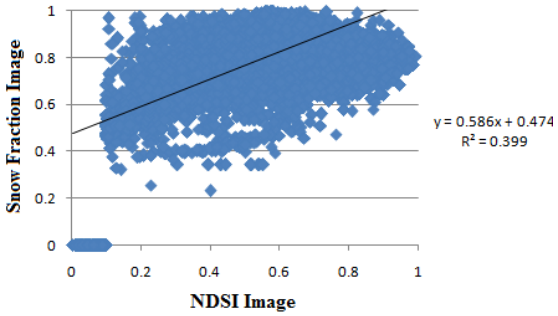

(d) 28 January 2009

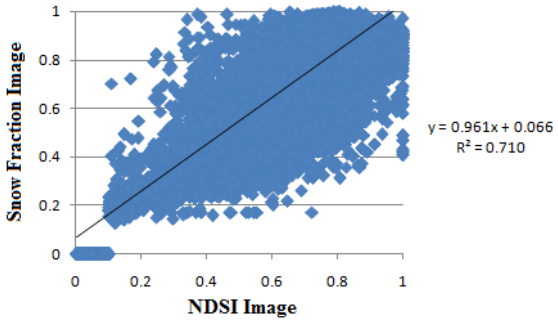

(e) 26 February 2009

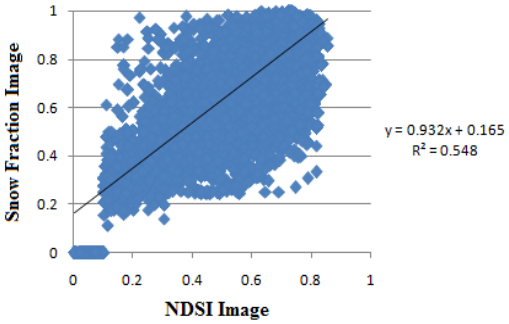

(f) 16 March 2009

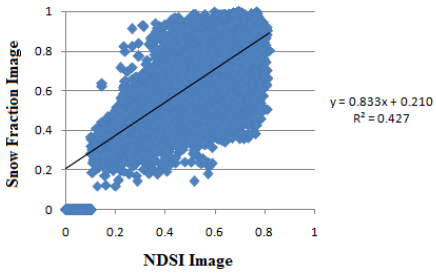

(g) 13April 2009

Figure 5.13 :Regression between values of snow fraction image (FCM using MN) and NDSI image.

Table 5.7 Values of correlation coefficients of regression equations.

MODIS images obtained on dates	Correlation Coefficient (LMM)	Correlation Coefficient (FCM using Diagonal Norm)	Correlation Coefficient (FCM using Euclidean Norm)	Correlation Coefficient (FCM using Mahalonobis Norm)
01-Oct-08	0.839	0.973	0.955	0.327
10-Nov-08	0.812	0.905	0.939	0.593
02-Dec-08	0.821	0.856	0.853	0.682
28-Jan-09	0.733	0.822	0.647	0.399
26-Feb-09	0.613	0.756	0.744	0.710
16-Mar-09	0.740	0.842	0.827	0.548
13-Apr-09	0.688	0.828	0.822	0.427

Table 5.8 Calculated snow covered areas using average equations obtained with different methods.

MODIS images obtained on dates	Snow covered area (km^2) using NDSI technique	Snow covered area (km^2) using average equation of regression b/w LMM and NDSI	Snow covered area (km^2) using average equation of regression b/w FCM (DN) and NDSI	Snow covered area (km^2) using average equation of regression b/w FCM (EN) and NDSI	Snow covered area (km^2) using average equation of regression b/w FCM (MN) and NDSI
01-Oct-08	2710.06	3273.42	3318.32	3402.19	3585.55
10-Nov-08	1225.93	1942.54	1842.93	1903.02	2276.42
02-Dec-08	506.81	1384.36	1192.4	1244.39	1782.02
28-Jan-09	4909.62	6022.59	6293.24	6432.24	6389.97
26-Feb-09	6931.25	7199	7851.36	7984.01	7379.02
16-Mar-09	7133.68	6974	7564.22	7696.79	7189.27
13-Apr-09	7187.25	6829.41	7432.54	7556.07	6952.33

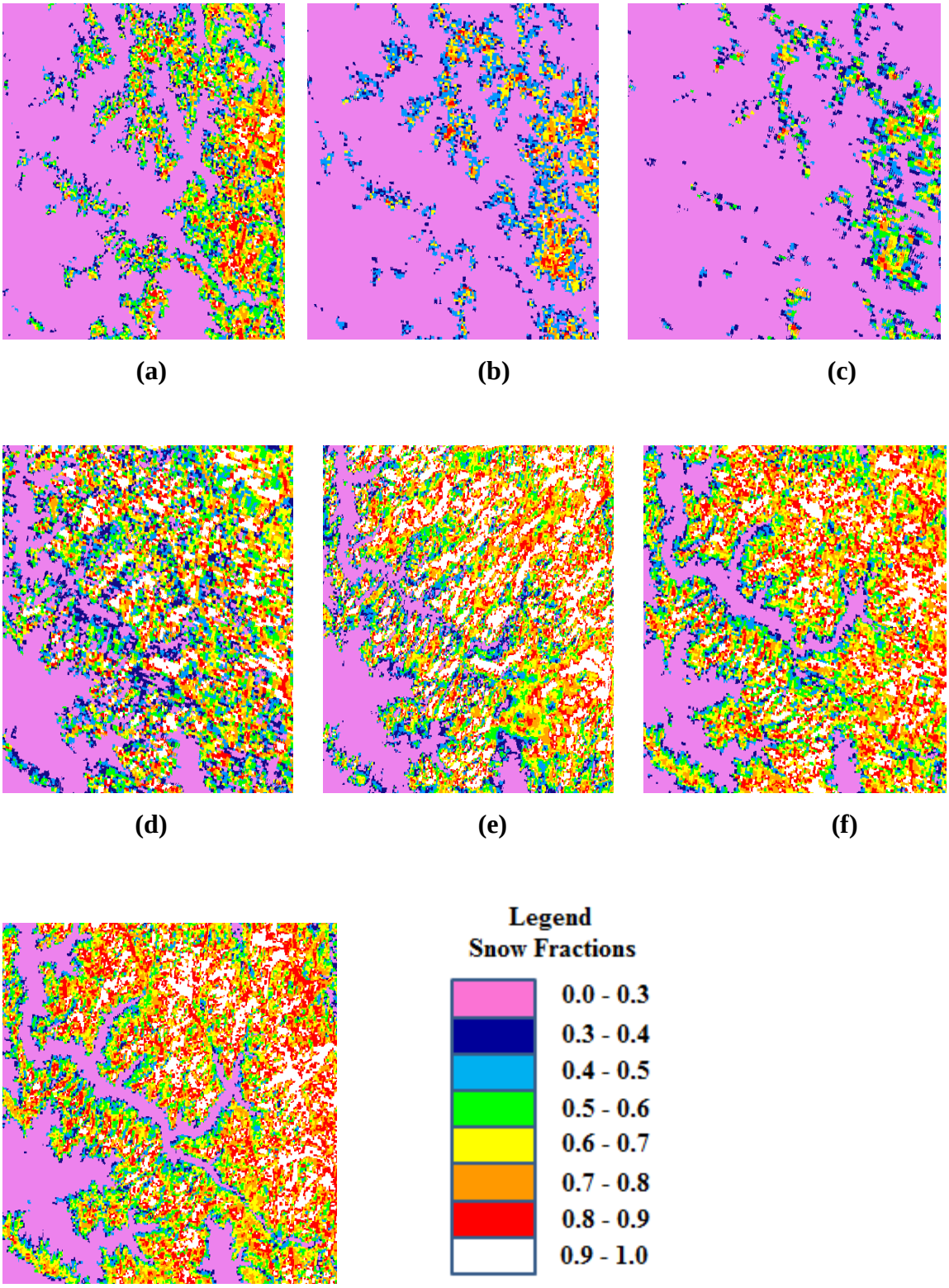

Figures 5.14 : MODIS Snow fraction images (LMM) obtained using NDSI method on dates: (a) 01 October 2008, (b) 10 November 2008, (c) 02 December 2008, (d) 28 January 2009, (e) 26 February 2009, (f) 16 March 2009, (g) 13April 2009.

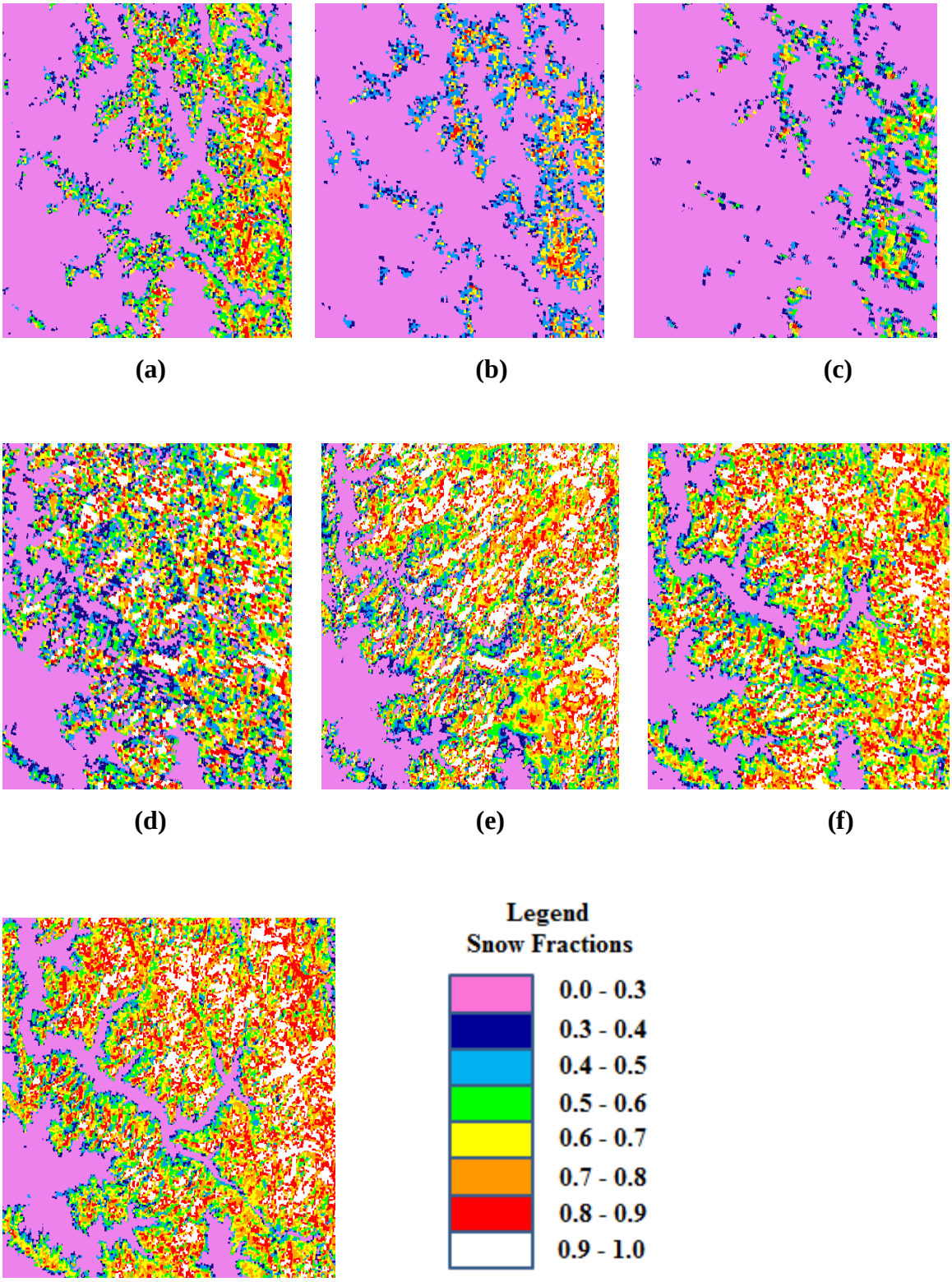

Figures 5.15 : MODIS snow fraction images obtained from NDSI by developing statistical relationship between FCM (using diagonal norm) and NDSI method on dates: (a) 01October 2008, (b) 10 November 2008, (c) 02 December 2008, (d) 28 January 2009, (e) 26 February 2009, (f) 16 March 2009, (g) 13April 2009.

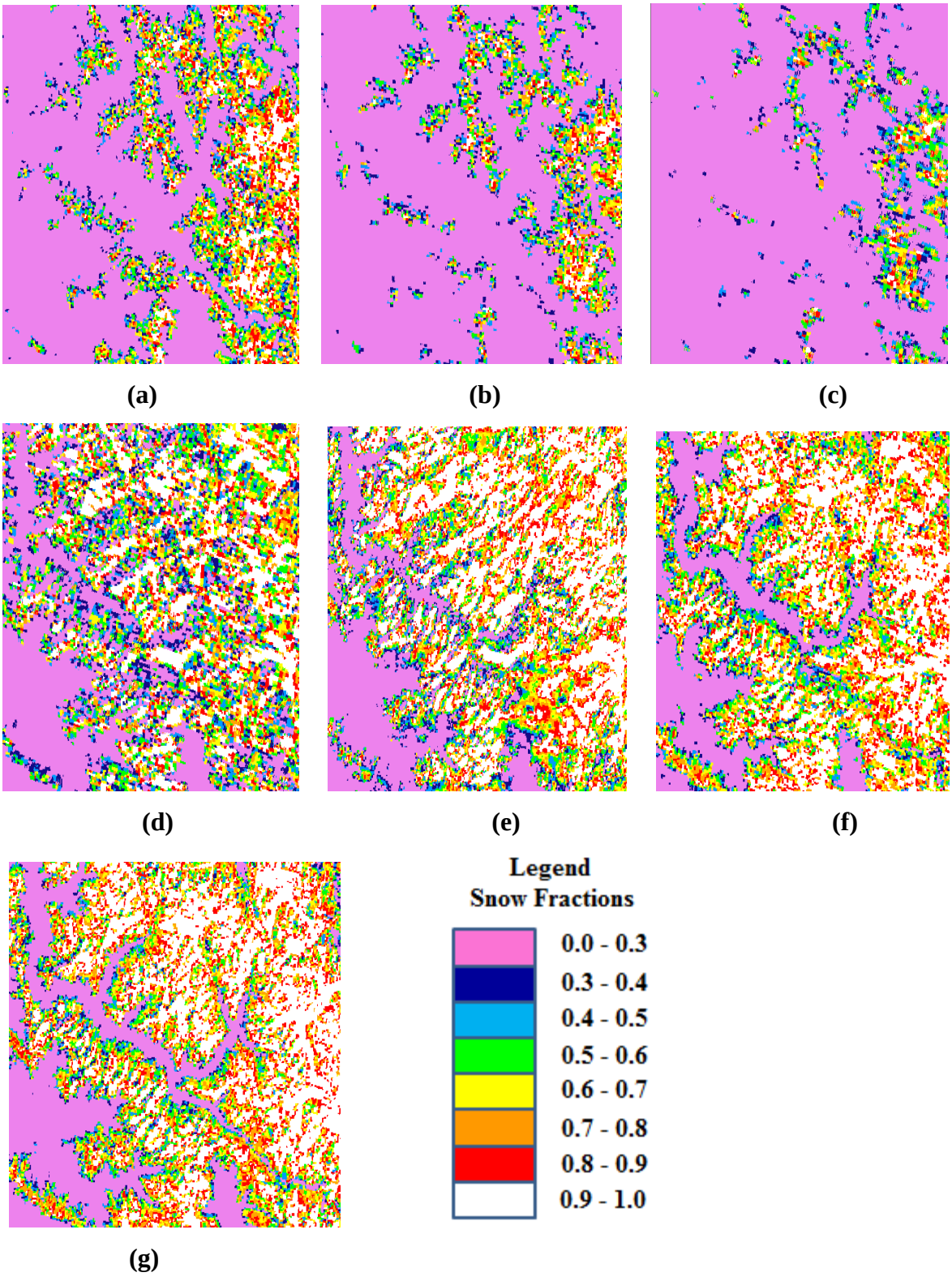

Figures 5.16 : MODIS snow fraction images obtained from NDSI by developing statistical relationship between FCM (using EN) and NDSI method on dates (a) 01 October 2008 (b) 10 November 2008 (c) 02 December 2008 (d) 28 January 2009 (e) 26 February 2009 (f) 16 March 2009 (g) 13April 2009

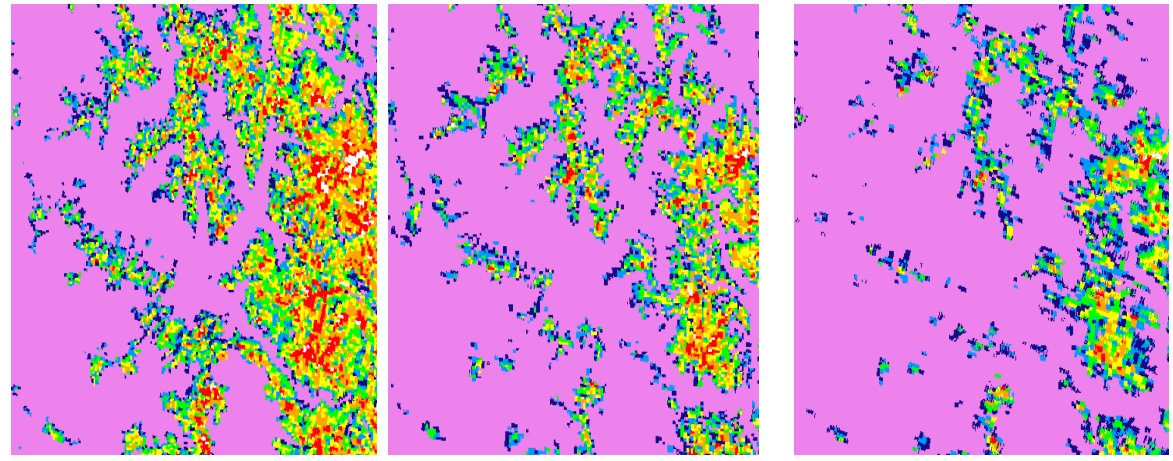

(a) (b) (c)

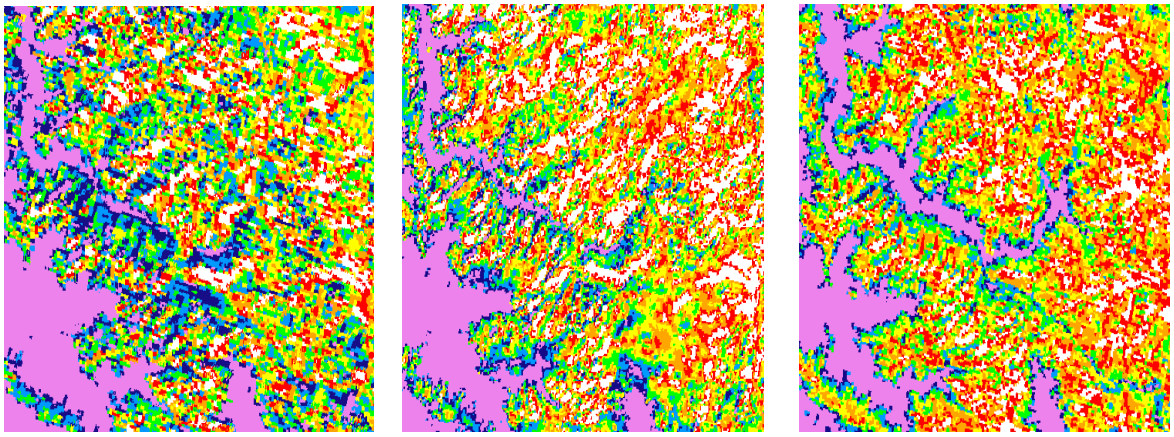

(d) (e) (f)

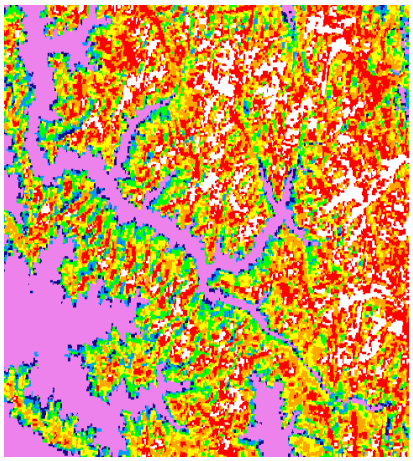

(g)

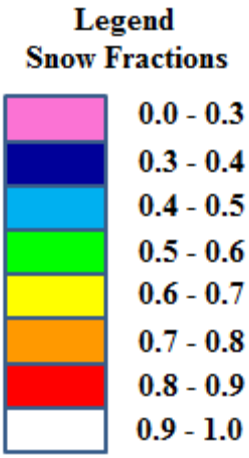

Figures 5.17: MODIS Snow fraction images obtained from NDSI by developing statistical relationship between FCM (using MN) and NDSI method on dates (a) 01 October 2008 (b) 10 November 2008 (c) 02 December 2008 (d) 28 January 2009 (e) 26 February 2009 (f) 16 March 2009 (g) 13April 2009

5.5 Accuracy Assessment

Accuracy assessment of sub-pixel snow classification has been performed. The root mean square error (RMSE) is calculated using equation 5.17. The RMSE values obtained for all the four sub-pixel techniques are shown in Table 5.9. RMSE values for all the images from FCM using EN are found to be the lowest followed by those from FCM using DN, LMM and FCM using MN. However, the RMSE values from FCM using EN and FCM using DN are almost comparable signifying that these methods can classify the images more accurately than other methods.

Table 5.9 Calculated values of RMSE

MODIS images obtained on dates	LMM	FCM (DN)	FCM (EN)	FCM (MN)
01 October 08	0.073	0.057	0.050	0.13
10 November 08	0.053	0.041	0.036	0.15
02 December 08	0.035	0.041	0.054	0.086
28 January 09	0.124	0.101	0.075	0.139
26 February 09	0.09	0.075	0.071	0.123
16 March 09	0.178	0.065	0.062	0.123
13 April 09	0.287	0.267	0.258	0.25

5.6 Validation of MODIS subpixel with medium resolution AWiFS image

The average regression equations in Table 5.6 are implemented directly to other geographical area of North West Himalaya on MODIS image of 2 November 2009. The AWiFS image of the same area and almost near real time of 1 November 2009 is used for validation. The detailed salient specifications of AWiFS sensor are already described in the Chapter 4. The MODIS and AWiFS pixel has spatial resolution of 500m and 56 m respectively. AWiFS image which has comparatively ten times higher resolution corresponding to MODIS image is used for validation. The AWiFS pixels were re-sampled to 50m spatial resolution for simplicity so that a single 500 m MODIS pixel will cover total 100 AWiFS pixels. The MODIS and AWiFS images used for validation are given in the Figure 5.18. The validation area is part of North West Himalaya and varies from Latitude 33.667 degree to Latitude 34.175 and Longitude 75.579 degree to Longitude 76.285 degree.

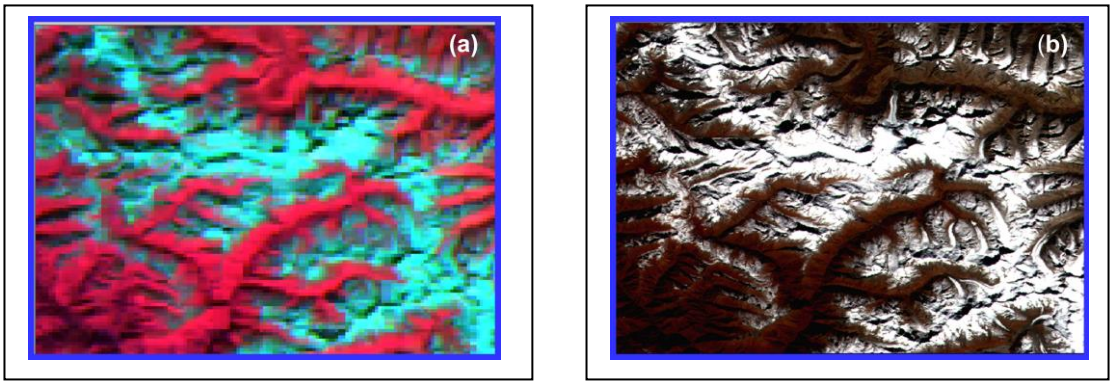

Figure 5.18: (a) MODIS image – 2 November 2009 and (b) AWiFS image – 1 November 2009 for validation

The MODIS image and AWiFS image were georeferenced with subpixel accuracy. The single MODIS pixels and corresponding AWiFS pixels are shown in the Figure 5.20. Figure 5.19 (c) shows the visual accuracy of matching of MODIS pixels with AWiFS pixels. Figure 5.20 shows the MODIS sub-pixel snow classification using universal

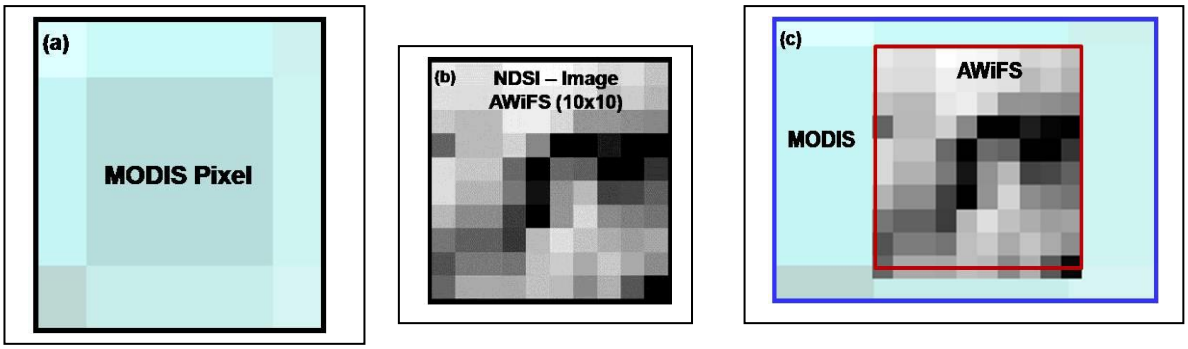

Figure 5.19: (a) MODIS single pixel 500mx500m (b) corresponding 100 AWiFS pixels in one MODIS pixel and (c) geolocation accuracy red boundary correspond to one MODIS pixel.

algorithms (Table 5.6) for LMM and FCM clustering. The visual analysis reveals same color pattern for sub-pixel snow for LMM and FCM using MN (Figure 5.20(a) and 5.20 (d). The same similarity is also observed for FCM using DN and FCM using EN (Figure 5.20 (b) and 5.20 (c). The MODIS results of different geographical area in Figure 5.20 (a-d) are validated for random pixels with sub-pixel fraction vary from 10% to 100% using AWiFS image. Each AWiFS pixel is classified as a single class either snow or non-snow based on NDSI. The

NDS)nn

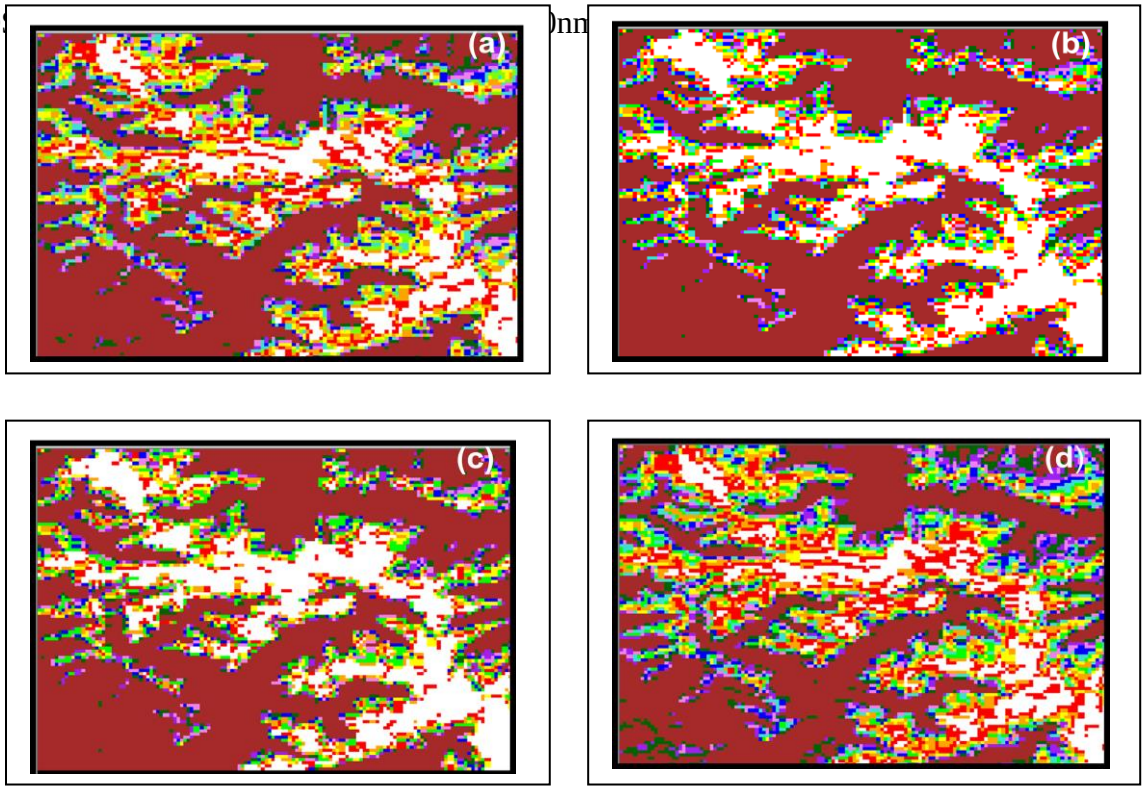

Figure 5.20: Sub-pixel snow fractions (SFRA) for MODIS image of date – 2 November 2009 using universal algorithm (a) Linear Mixture Model (LMM) (b) FCM using Diagonal Norm (c) FCM using Euclodiean Norm and (d) FCM using Mahalonobis Norm.

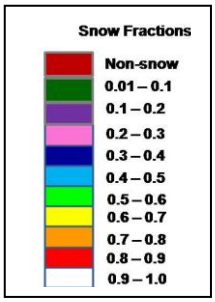

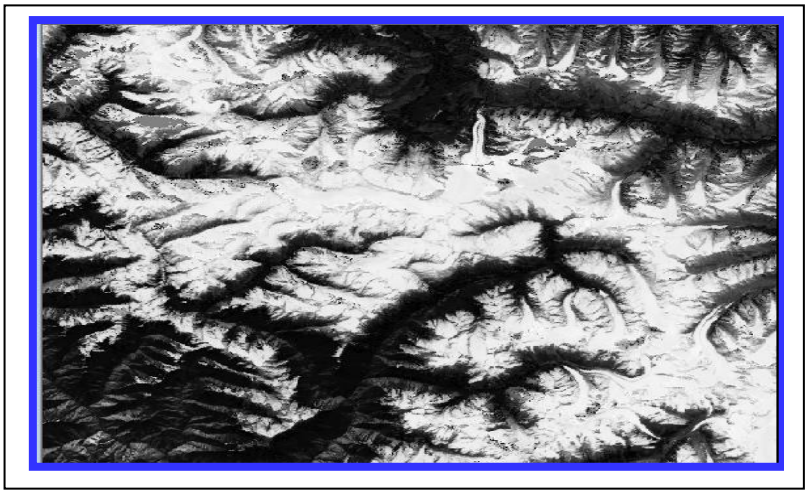

Figure 5.21: NDSI images of AWiFS – 1 November 2009 corresponding to geographical area of MODIS image in Figure 5.21 .

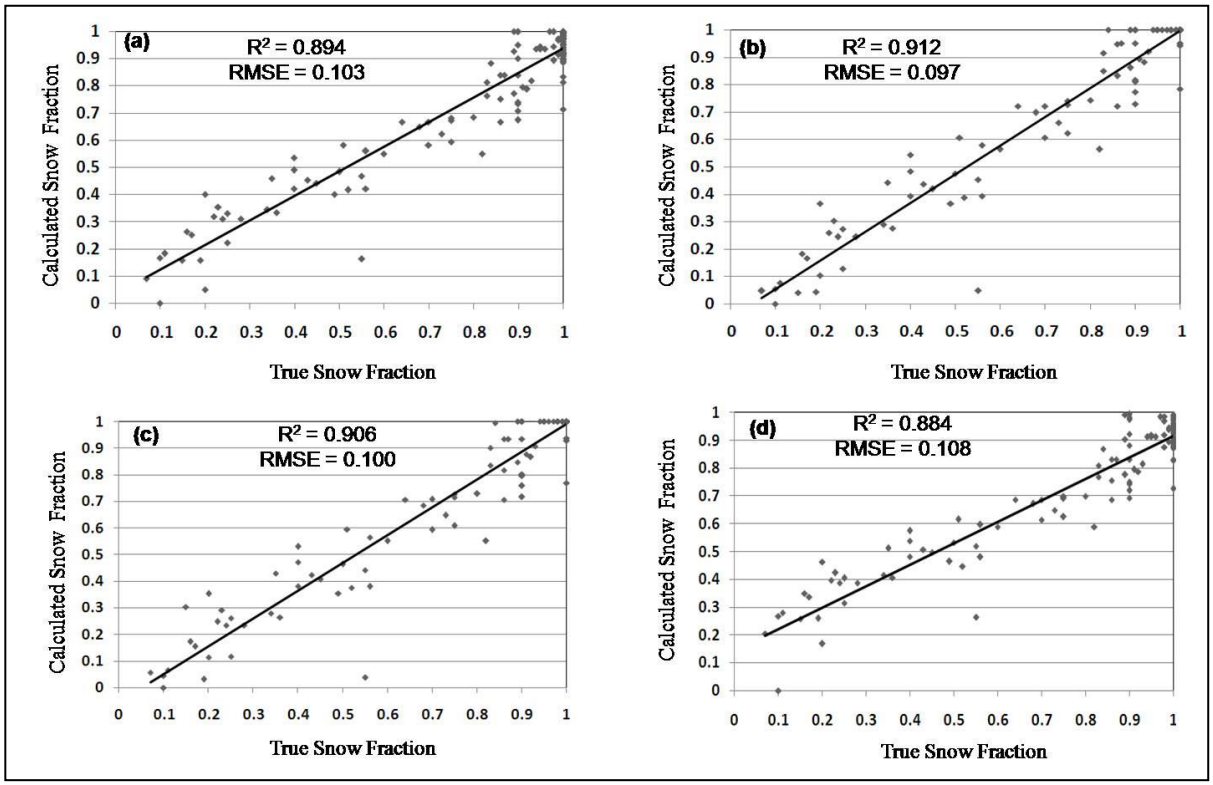

Figure 5.22 : Calculated snow fractions versus true snow fractions observations based on AWiFS scene of north west Himalaya (a) LMM (b) FCM-DN (c) FCM-En and (d) FCM-MN.

infrared band 4 (1550 nm – 1700 nm) is estimated for AWiFS image using equation 5.3 and is shown in the Figure 5.21. A total of 122 random pixels of MODIS SFRA at 500 m spatial resolution are verified with AWiFS pixels. If NDSI >=0.4, the AWiFS pixel is mapped as snow. Total hundred AWiFS pixels at 50 m spatial resolution are counted corresponding to single MODIS snow fraction pixel. The results of regression between true snow pixels (AWiFS) and calculated SFRA from MODIS are shown in the Figure 5.22. The good correlation (> 0.88) is observed for all the methods, although the FCM using DN and FCM using EN show the best correlation having values more than 0.9. The RMSE is also determined using calculated and true snow faction and is found to vary from 0.097 to 0.108. The RMSE for FCM using DN (0.097) and FCM using EN (0.100) are estimated to be the lowest among all.

CHAPTER 6

Change Detection Analysis

Chapter 6

Evaluation of influence of topography on change detection in snow covered areas

6.1 Change Detection Analysis

In Himalaya, snow cover distribution is very complex due to rugged topography and highly variable climatic conditions. The accurate land use/land cover change feedback is very important for avalanche forecasters in Himalayan region. These land/snow covered changes cannot be retrieved manually. Multitemporal and multispectral analysis of satellite images is becoming important research fields in geoinformation science. Satellite based remote sensing technology has been successfully used in the past to accurately detect, monitor and display changes over large areas (Gong and Xu 2003). In snow covered Himalaya regions, frequent changes occur at every spatial and temporal scale by virtue of natural atmospheric processes such as human-caused activity and natural hazards like landslides and avalanches. The qualitative and quantitative analysis of different changes occurring at spatial and temporal scale help to get reliable information for users and forecasters un Himalayan region. Proper and accurate use of information retrieved from satellite remote sensing can help to link science and management by understanding natural processes impacted as a result of the disturbances (Wulder and Franklin, 2003).

In the past few years, there has been a growing interest in the development of change detection techniques for the analysis of multi-temporal remote sensing imagery. Change detection, by definition, requires images from two dates. Ideally, change detection procedures should involve data acquired by the same sensor, having the same spatial resolution, viewing geometry, spectral bands, same spatial location, radiometric resolution, and acquired at the same time of day (Lillesand *et al.*, 2000). A synoptic review of large number of change detection techniques used by various researchers using remote sensing images are summarized or classified from different viewpoints (Lu *et al*., 2004; Coppin *et al*., 2004). It has generally been agreed that change detection is a complicated and integrated process. No existing approach is optimal and universally applicable to all cases. Standard change vector analysis (CVA) is cited as an effective change detection tool (Warner, 2005) that characterizes movement in spectral space over time in terms of magnitude and direction. The drawback of conventional CVA is that it shows changes only in two dimensions in spectral feature space. The other problem is estimation of threshold of magnitude between change and

no change classes. The threshold is generally defined by visual qualitative analysis using satellite images or by experience and familiarization about the area which may not produce accurate results.

6.2 Methodology

The present work is not intended for discussion and implementation of various change detections methods or algorithms. The core issue discussed in this study is to investigatethe effect of topography and topographic corrections on change detection analysis of snow cover in the Himalayan terrain. The improved CVA has been implemented and accuracy assessment carried out as compared to conventional CVA. In the light of the drawbacks of CVA mentioned earlier, the improved CVA method is considered in the present work. Firstly we discuss a multidimensional extension in spectral space called hyperspherical direction cosine (HSDC) or simply direction cosine (Chen *et al*., 2003). Secondly, a semiautomatic method, called Double-Window Flexible Pace Search (DFPS) is implemented which determines efficiently the threshold of change magnitude between change and no change classes. The image based atmospheric corrections are applied before computation of spectral reflectance. Combination of dark object subtraction model (DOS1 and DOS3) is used for atmospheric corrections (Song *et al*., 2001; Mishra *et al*., 2009a). All satellite images are topographically corrected using slope matching method which was found to be most suitable for Himalaya terrain as concluded in chapter 4 earlier and has also been reported (Mishra *et al*., 2009b,c). Finally change detection accuracy assessment for improved CVA method is reviewed with and without topographic inclusion. The flow chart of detailed methodology is given in the Figure 6.1.

6.2.1 Study area

The study area is a part of Lower and Middle Himalaya and shown on AWiFS images (Advance Wide Field Sensors) in the Figure 6.2. It lies between latitude of 32.254 degree to 32.999 degree North and longitude of 77.00 degree to 77.497 degree East. The lower part of the area is populated by forest and tree line exists up to 3100 m. The upper part (Middle Himalaya) is devoid of forest. The average minimum temperature in winter is generally observed to be -12^{o}C to -15^{o}C in Lower Himalaya (Pir-Panjal range) and -30^{o}C to -35^{o}C in Middle Himalaya (Greater Himalaya range). Pir-Panjal receives the higher snowfall (average 15-20 m) as compared to Greater Himalayan range (12-15m) during the winter period between October and May. The altitude in the entire study area varies from 1900 m to 6500 m (Figure 6.3) with a mean value of 4700 m. The slope in the study area varies from 1-86

degrees with a mean value of 28 degrees and aspect ranges from 0-360 degree with mean values of 180 degree. Most of the slopes in the study regions are oriented to south aspect.

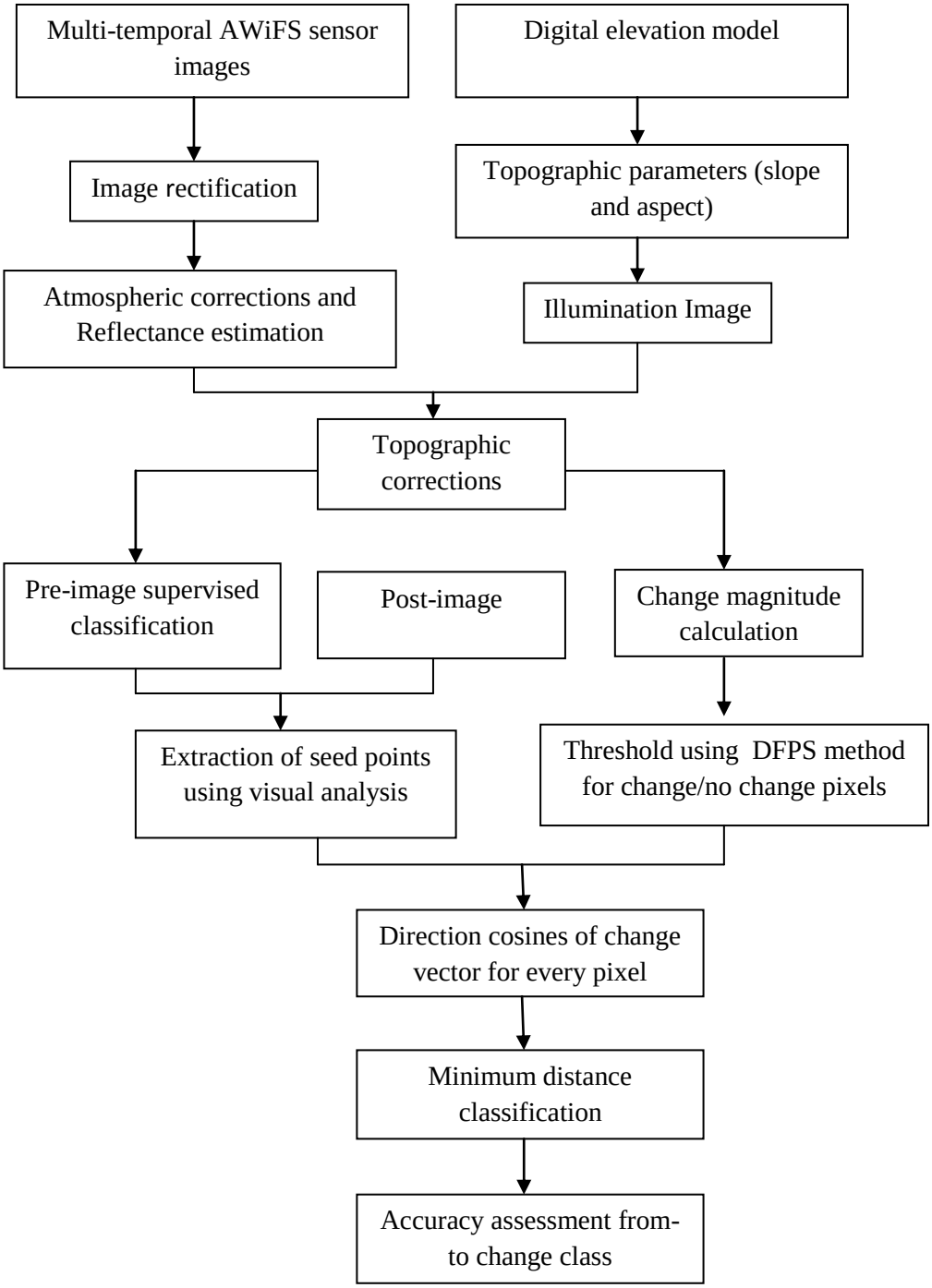

Figure 6.1 : Flow chart showing methodology for improved spectral change vector analysis.

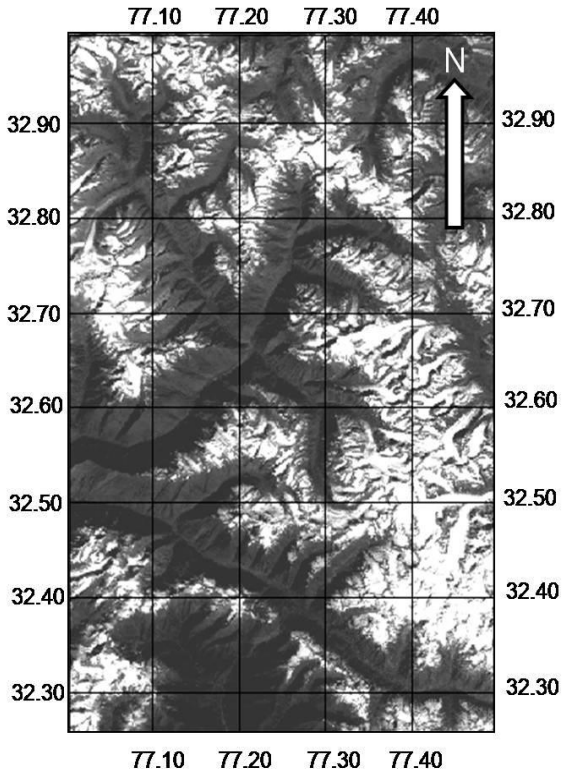

Figure 6.2 : Radiometrically corrected AWiFS image of study area

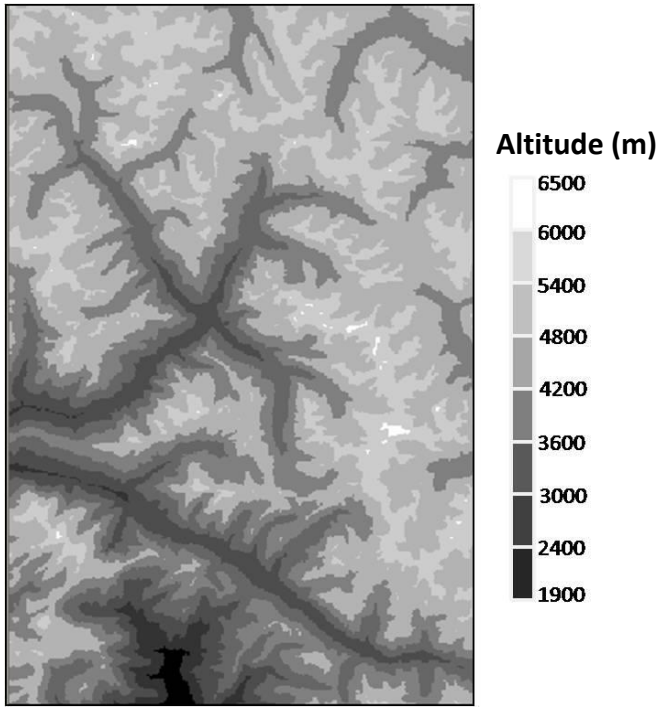

Figure 6.3 : Digital elevation model of study area

6.2.2 Satellite images and geometric correction

Two almost cloud free multi-temporal Advance Wide Field Sensor (AWiFS) images (13 October 2009 and 20 November 2009) of RESOURCESAT-1 onboard IRS-P6 have been used in the present analysis. AWiFS scans a 740 km wide swath acquiring data in four spectral bands including Visible (Green and Red), near infrared (NIR), and SWIR. Its spatial resolution is 56m at Nadir. Its radiometric resolution is 10 bit, which does not saturate over snow. The salient specifications of AWiFS sensor are found in the literature (Mishra *et al*., 2009b, Singh *et al*., 2009) and mentioned in chapter 3. All the AWiFS sensor imageries are geometrically and radiometrically corrected before performing change detection analysis. It is a very crucial step in change detection analysis. The mismatch of two multi-date imageries may produce erroneous result and significantly affect change detection results. It is very difficult to select the ground control point (GCPs) in mountainous region mainly during peak winter period when most of the area is covered with snow. Thus a, master image of summer season of IRS-LISS-III (Indian Remote Sensing, Linear Imaging Self Scanning) has been prepared after rectification with 1:50,000 toposheet. This master image served as a reference for further geo-referencing of AWiFS satellite images. Second order polynomial transformation was used for image rectification and geolocation error was about one pixel (X= 0.4313, Y = 0.4137 and total error 0.5977) or less in both the satellite images. Satellite images were geo-coded to the EVEREST datum by ERDAS/Imagine 8.7 (Leica Geosystems GIS & Mapping LLC) software.

6.2.3 Digital elevation model

A digital elevation model (DEM) of the study area has been generated using 1:50,000 toposheet at 40 m contour interval as shown in the Figure 6.3. The non-linear interpolation function is used for 3-D surface generation. The initial grid resolution of the DEM is 6m which was further re-sampled at satellite sensor spatial resolution of AWiFS. It was then used to generate topographic parameters namely slope, aspect and illumination required for slope match method for terrain corrections.

6.2.4 Estimation of reflectance

Without topographic consideration, the atmospherically corrected surface spectral reflectance under lambertian assumption for AWiFS is computed using the following

equation (Song *et al*., 2001; Pandya *et al*., 2002):

$$R_\lambda = \frac{\pi\left(L_{sat\lambda} - L_p\right) d^2}{t_v \left(E_0 \cos\theta_z \, t_z + E_d\right)} \quad (6.1)$$

Where t_v and t_z are the transmittances of the atmosphere in the view and illumination directions respectively calculated for AWiFS bands using the equation proposed by authors (Russell et al. 1993, Song et al., 2001); E_0 is the exo-atmospheric spectral irradiance, θ_z is the solar zenith angle and calculated for each pixel (Kasten 1962); d is the earth – sun distance in astronomical units and calculated using the approach of Van Dee Meer (1996), E_d is the downwelling diffused radiation and assumed to be zero according to (Chavez, 1996). L_p Is the path radiance and computed using (Chavez 1996). Multi-temporal topographically uncorrected AWiFS images are shown in the Figures.6.4 (a, b).

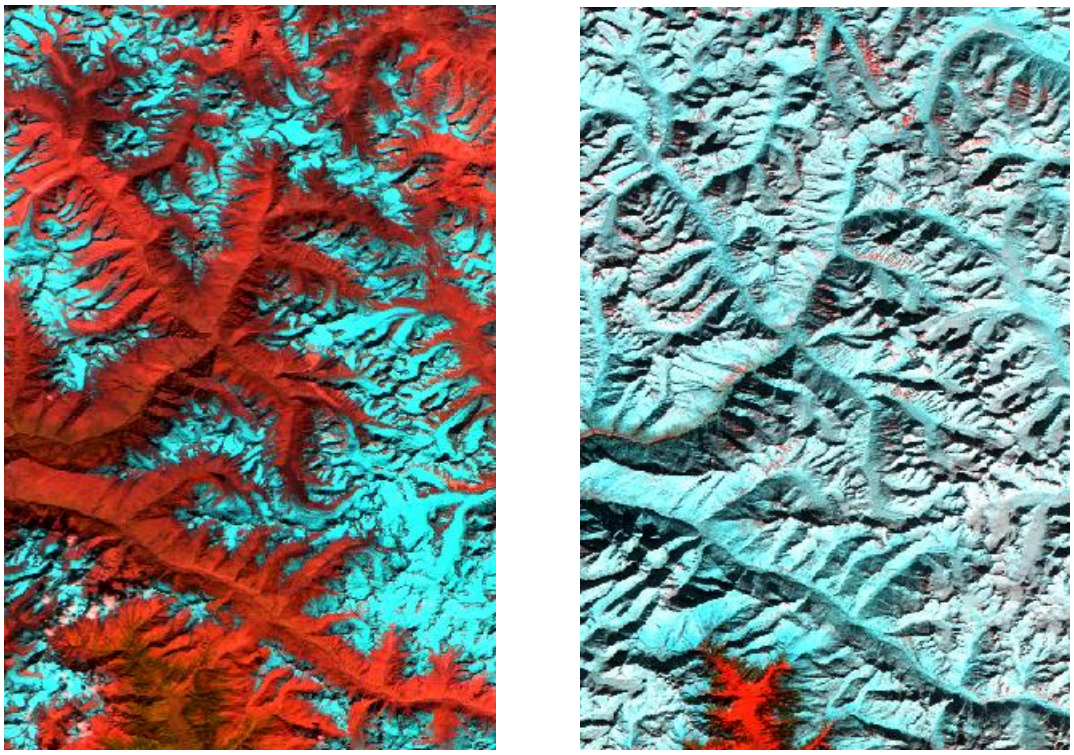

(a) **(b)**

Figure 6.4: Topographic uncorrected AWiFS images (a) 13th October 2009 (*Pre-image*) (b) 20th November 2009 (*Post image*)

6.2.5 Topographic corrections using slope match method

There are various methods for topographic corrections such as Cosine corrections, C-correction, Minneart correction, Statistical methods etc. as reported in the literature (Civco, 1989; Colby, 1991).The extensive analysis of efficacy of different topographic correction methods for Himalayan terrain has been carried out as given in chapter 4 earlier and has also been reported (Mishra *et al*., 2009b,c). Slope matching method has been found to be most suitable topographic corrections for Himalayan terrain and used in the present work. Topographically corrected spectral reflectance using AWiFS imagery are estimated using slope matching method given below (Mishra *et al*., 2009b):

$$R_\lambda^t = R_\lambda + (R_{\lambda max} - R_{\lambda min}) \left(\frac{<cosi>s - cosi}{<cosi>s} \right) C_\lambda \qquad (6.2)$$

Where R_λ^t is topographically corrected spectral reflectance, R_λ is reflectance on the tilted surface, $R_{\lambda max}$ and $R_{\lambda min}$ is maximum and minimum spectral reflectance and estimated from topographically uncorrected reflectance R_λ image , $< cosi > s$ is mean

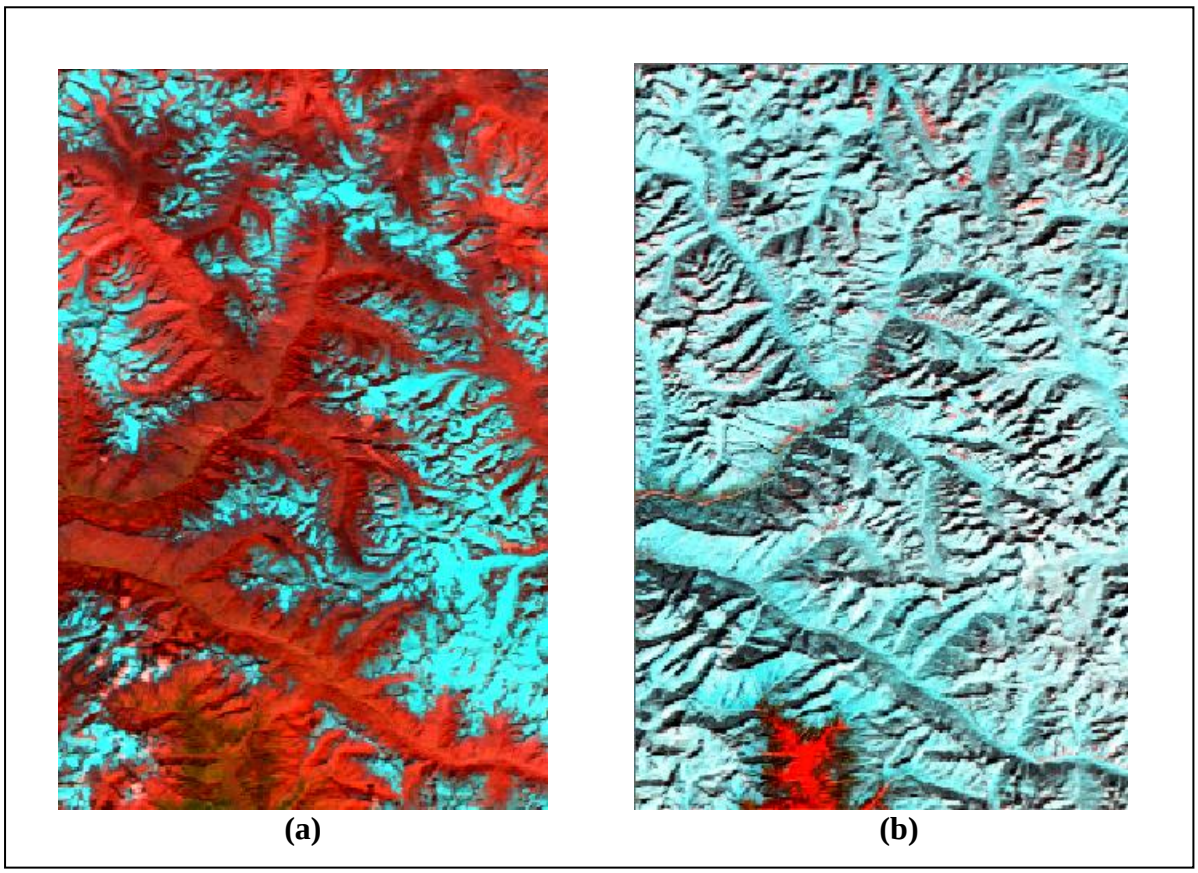

(a) **(b)**

Figure 6.5 : Topographic corrected AWiFS images (a) 13th October 2009 (*Pre-image*), (b) 20th November 2009 (*Post image*)

value of illumination on the south aspect and $cosi$ is illumination and calculated using equation proposed by (Civco, 1989). C_λ is normalization coefficient for different satellite bands and estimated using equation given in the literature (Nichol *et al*., 2006) and discussed in chapter 4. The topographically corrected images are shown in the Figures 6.5 (a, b).

6.3 Change Vector Analysis

A change vector can be represented as a method of detecting radiometric changes between multispectral and multi-date satellite data in any number of spectral bands. It is described by an angle of change (vector direction) and a magnitude of change from date 1 satellite image to date 2 satellite image of the same geographical area (Jensen, 1996). The original CVA works on two and occasionally three bands only. This method extracts information about both the magnitude and the direction of changes in the data, so that the changes are characterized by vectors having magnitudes and directions in two dimensional spectral change space (Michalek et al., 1993). If a pixel's reflectance values in two images on date t_1, t_2 are given by $I_1 = (I_{11}, I_{12}, \text{-------}, I_{1N})$ and $I_2 = (I_{21}, I_{22}, \text{-------}, I_{2N})$. The change vector can be expressed as :

$$\Delta I = I_1 - I_2 = \begin{pmatrix} I_{21} - I_{11} \\ I_{22} - I_{12} \\ - \quad - \quad - \\ I_{2N} - I_{1N} \end{pmatrix} \tag{6.3}$$

where the magnitude can be estimated using the equation of the Euclidean distance in an N-dimensional (spectral space equal to number of bands) space :

$$\|\Delta I\| = \sqrt{(I_{21} - I_{11})^2 + (I_{22} - I_{12})^2 + \ldots\ldots\ldots\ldots (I_{2N} - I_{1N})^2} \tag{6.4}$$

A change in the pixel depends on whether change magnitude exceeds a specific threshold. Once change pixel is identified, the direction of ΔI can be analyzed further to determine the type of change. The type of change is identified using the angle of the change vector, $\cos\theta$, in two dimension spectral space using the following equation:

$$\cos\theta = \frac{\Delta I}{\|\Delta I\|} \tag{6.5}$$

The drawback of the existing CVA is (i) the threshold of change magnitude is difficult to identify for change/no change area and (ii) the type of change in equation (6.5) can be described in only two dimensional spectral spaces. These two drawbacks are overcome in the new CVA and discussed in the next section.

6.4 Improved CVA

Double - Window flexible pace search (DFPS) to estimate change magnitude threshold

The threshold of change magnitude is generally determined using empirical methods which may vary from person to person. Double - Window Flexible Pace Search (DFPS) algorithm suggested by Chen *et al*., 2003 is used to systematically determine optimal value of change magnitude threshold between change and no change classes. The threshold is determined by selecting training samples after visual analysis containing all types of changes in two multi-date satellite images. The training samples are generally representative of the entire study area. This condition may not always exist in AWiFS images of Himalaya due to very limited land covers available during winter period. Most of the area is covered by snow during winter and from - to - class inter change is very limited. We have used training samples of maximum possible change area. It is obvious that when threshold of change magnitude decreases, the number of change pixels inside the training area will also increase which will lead to improve an accuracy of change detection. However, the possibility of no change pixels identified as change pixels in outer boundary will also increase, leading to high commission error. The complete process involves the following steps (Chen *et al*., 2003):

Firstly, the training samples of change area from two multi-date imageries are chosen by visual interpretation and should include only change pixels (inner window). The training samples should be island encircled by no change pixel (outer window).

Secondly, The search range can be set as a difference between minimum value a and maximum value b of the change magnitude and the first search pace P_1 may be calculated according to the following formula :

$$P_1 = \frac{(b-a)}{m} \qquad (6.6)$$

where m is a positive integer that determines the number of potential thresholds in a search process and can be set manually. The potential thresholds to detect change pixels from the training samples in the search process are given within the range of (a,b) as $b - P_1$, $b - 2P_2$, ... It should be noted that the size of the manually set m does not affect the search efficiency

and the final results. A large m increases the number of potential thresholds during one search, but it decreases the number of searches.

Thirdly, the success rate of change detection is defined to evaluate the performance of each potential threshold during one search process for identifying change/no change

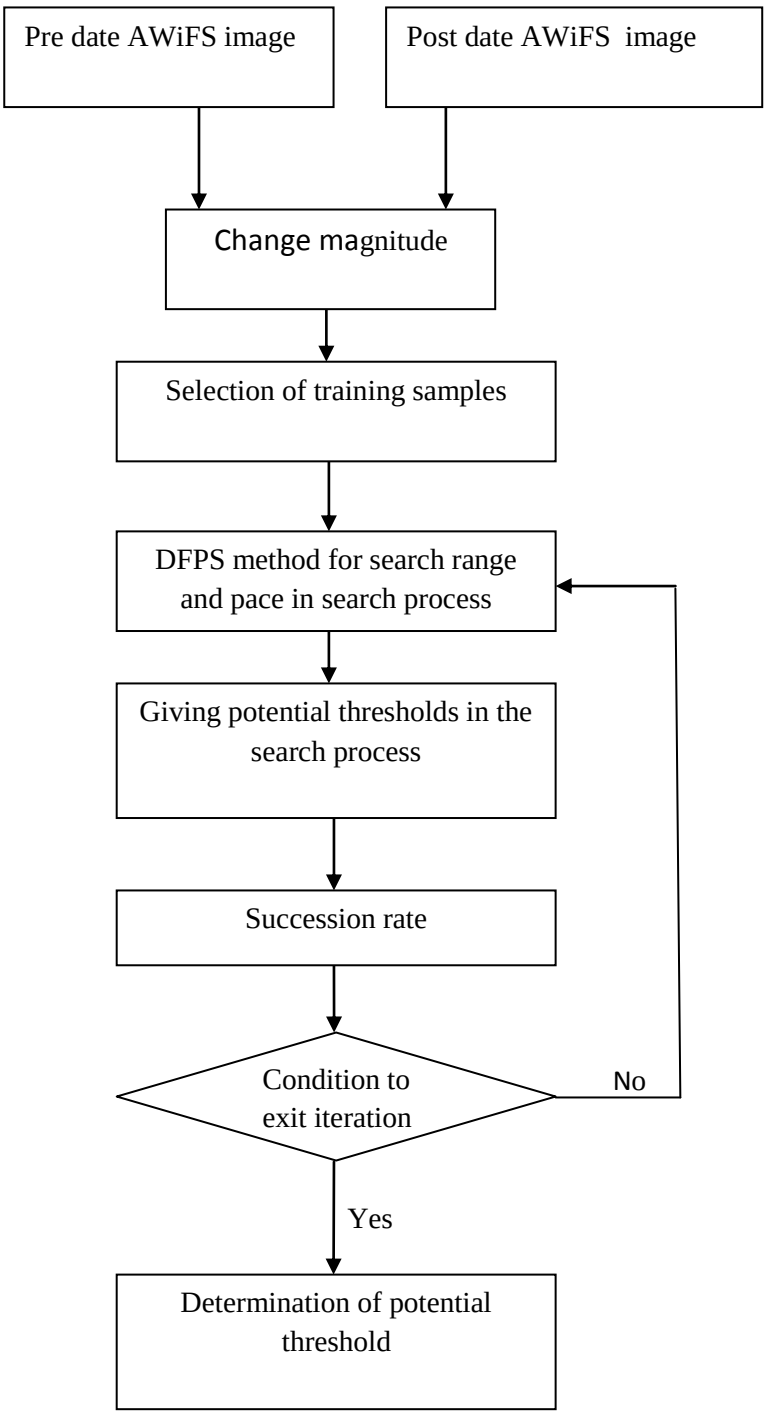

Figure 6.6 : Flow chart of the Double-windows Flexible Pace Search method

pixels. The success rate L_k is calculated for a potential threshold value of k using the

equation

$$L_k = \left(\frac{A_{k1} - A_{k2}}{A}\right) 100\% \quad (6.7)$$

where, A_{k1} is the number of change pixels detected inside all training patches (in inner window) and A_{k2} is the number of changed pixels detected incorrectly (in the outside window) and A is the total number of pixels in all training patches. After all L_k for all m thresholds in one search are obtained the maximum and minimum values of L_k are found and designated as L_{max} and L_{min} during this search process. If the two parameters do not satisfy the condition described in the fourth step, a new search starts. The new search range is set in the range (k_{max} - $P_1, k_{max} + P_1$), and a new smaller search pace is set based on the modified search range with equation (6.6), here k_{max} is the potential threshold value corresponding to L_{max} in the search process. Finally, the second and third steps involve an iterative process, which will be terminated when the following equation is satisfied.

$$(L_{max} - L_{min}) \leq \delta \quad (6.8)$$

where L_{max} and L_{min} are the maximum and minimum values of the success rate in one search process, and δ is an acceptable error constant. The threshold value corresponding to Lmax is considered to be an optimal threshold value for change detection. The flow chart of DFPS method is given in the Figure 6.6.

In the conventional CVA, direction of change vector is defined in equation (6.5) in two dimensional spectral space. Here, HSDC is an extension of CVA in multidimensional space in spectral domain and will depend on the number of bands available in sensor images. Each pixel in an image is considered as a spectral vector (Malila, 1980). If additive atmospheric effect is removed, pixels of a single spectral class should cluster along a line extending from the origin in a single spectral direction. These directions can be specific in multiband spectral space in HSDC values (Pouch and Campagna, 1990). The direction cosine values for a pixel is calculated by dividing the reflectance values in each band by the magnitude of the vector from the origin, represent the cosines of the projection of the pixel onto a hypersphere of unit radius.

Let X ($x_1, x_2, x_3, \ldots\ldots, x_n$) be an N-dimensional vector, its magnitude is calculated as

$$|X| = \sqrt{x_1^2 + x_2^2 + x_3^2 + \cdots + x_n^2} \quad (6.9)$$

If the angles between X and each axis are ($\theta_1, \theta_2, \theta_3, \ldots\ldots, \theta_n$) respectively, then its direction can be defined by cosine functions of these angles as (Hoffmann, 1975)

$$\cos\theta_1 = \frac{x_1}{|X|}\ , \cos\theta_2 = \frac{x_2}{|X|}\ , \cos\theta_3 = \frac{x_3}{|X|}\ , \ldots\ldots\ldots, \cos\theta_n = \frac{x_n}{|X|} \quad (6.10)$$

The direction of change vector can be represented by one and only one point, defined as a new vector Z($\cos\theta_1$, $\cos\theta_2$, $\cos\theta_3, \ldots\ldots, \cos\theta_n$) in the direction cosine space.

6.5 Results and Discussion

6.5.1 Threshold of change magnitude

The change magnitude on images of AWiFS between 13 October 2009 and 20 November 2009 estimated using equation (6.4) is shown in the Figure 6.7(a) (without topographic corrections) and Figure 6.7(b) (with topographic corrections). The change magnitude ranges from 0 to 174 for both without and with topographically corrected image. The threshold value of change magnitude for change/no change and succession rate for training samples from AWiFS images are estimated using DFPS algorithm with equation (6.6) and equation (6.7) respectively with the condition in equation (6.8). The results are shown in the Table1 and Table2. The most change magnitude occurs above 100 (succession rate 84.6%) and 50 (succession rate 78.42%) for topographically uncorrected and corrected image respectively. It is inferred that topographic corrections for differential illumination caused due to slope and aspect variability play an important role in estimation of threshold for change detection analysis.

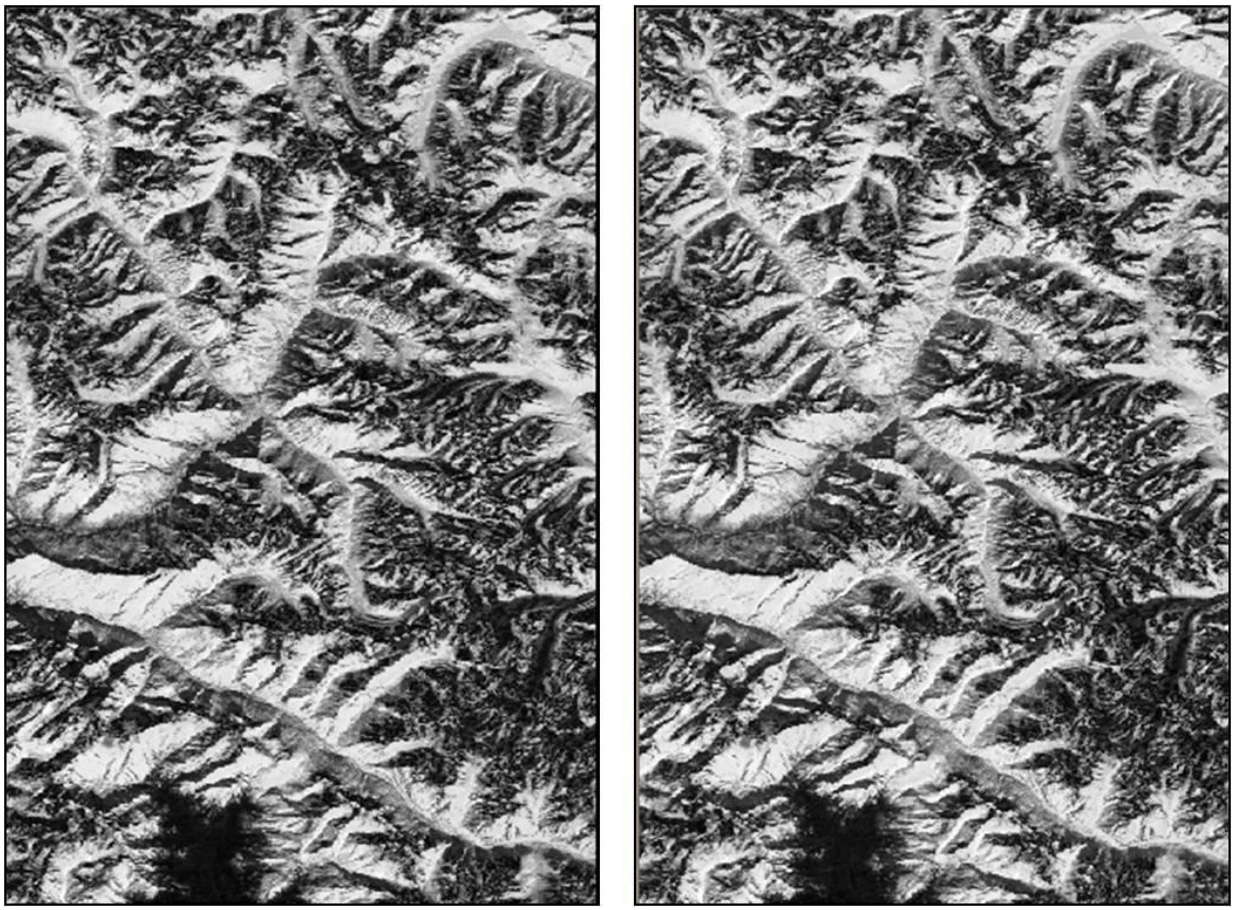

Figure 6.7: Change magnitude image of AWiFS between 13October 2009 and 20 November 2009 (a) Without topographic corrections and (b) With topographic corrections.

6.5.2 Change type discrimination (from-to-class change)

The change type discrimination from one class to another class is analyzed by classification of pre and post image. Four types of land cover namely snow, soil/rocks, vegetation and shadow are classified using supervised classification considering pre image as a reference image.

The post image is classified using direction cosines of change vector which combines single-date image classification with a minimum distance categorizing technique. The seed points (from-to-class change) are selected after visual analysis from both the images. The Euclidean distance between direction cosines of seed points with direction cosines of post image is estimated and minimum distance unsupervised classification is performed for four different land cover classes. The two classified pre and post AWiFS

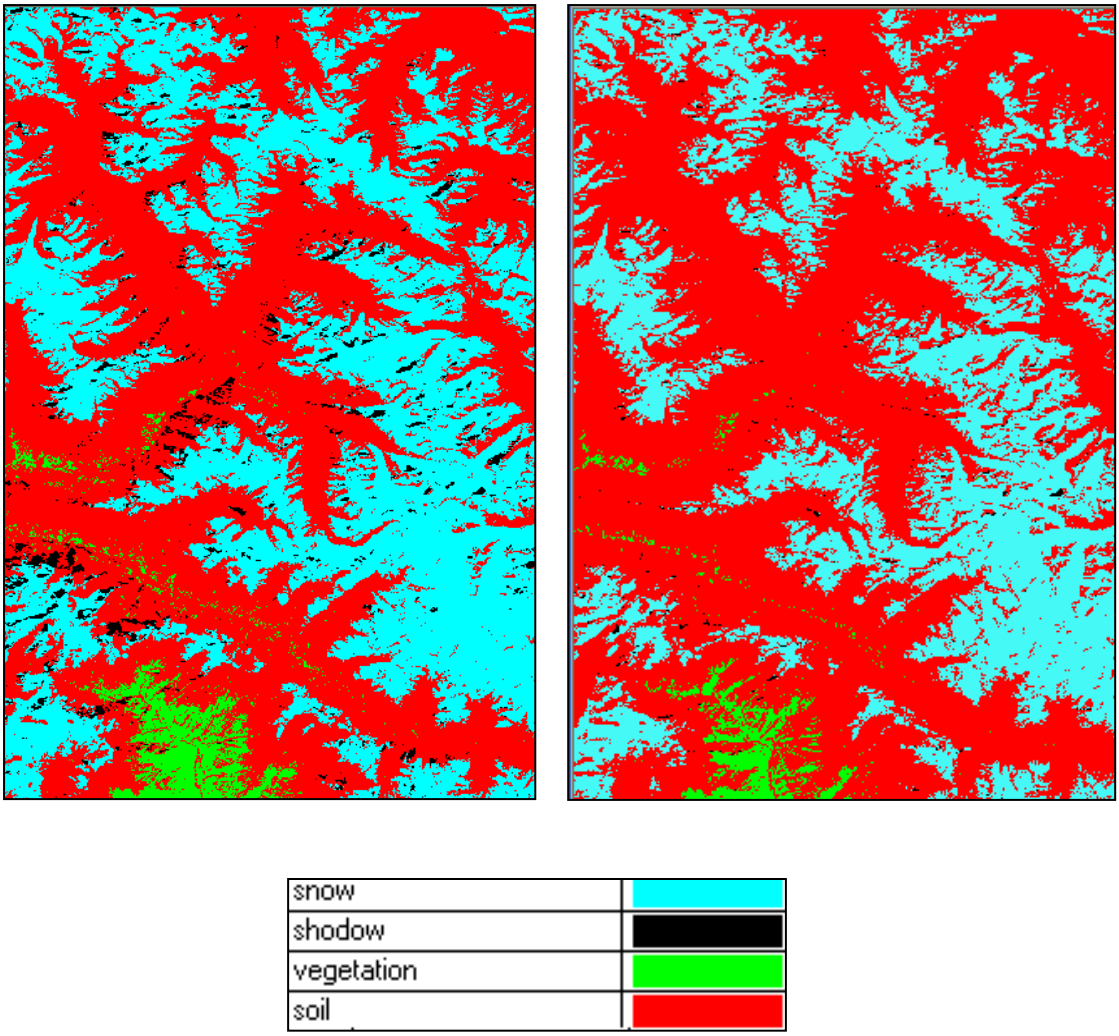

Figure 6.8 Classification of different land covers without topographic corrections (a) 13 October 2009 using supervised classification and (b) 20 November 2009 using improved CVA

images are shown in the Figure 6. 8 (topographically uncorrected) and Figure 6. 9 (topographically corrected).

6.6 Accuracy assessment

The main objective of this study is to assess the impact of topography on improved change vector analysis. The accuracy assessment was performed using improved CVA method and results are compared with topographic inclusion also. The accuracy and kappa coefficient is estimated for both "change/no change" detection and "from-to change detection levels. A random sampling technique was used considering overall 50 samples. The error matrix for change/no change classes using 50 samples in the Table 3 and Table 4 show overall accuracy increase from 82% (Kappa coefficient 0.6512) to 90% (kappa coefficient 0.7811) after topographic correction. It is very necessary to assess the

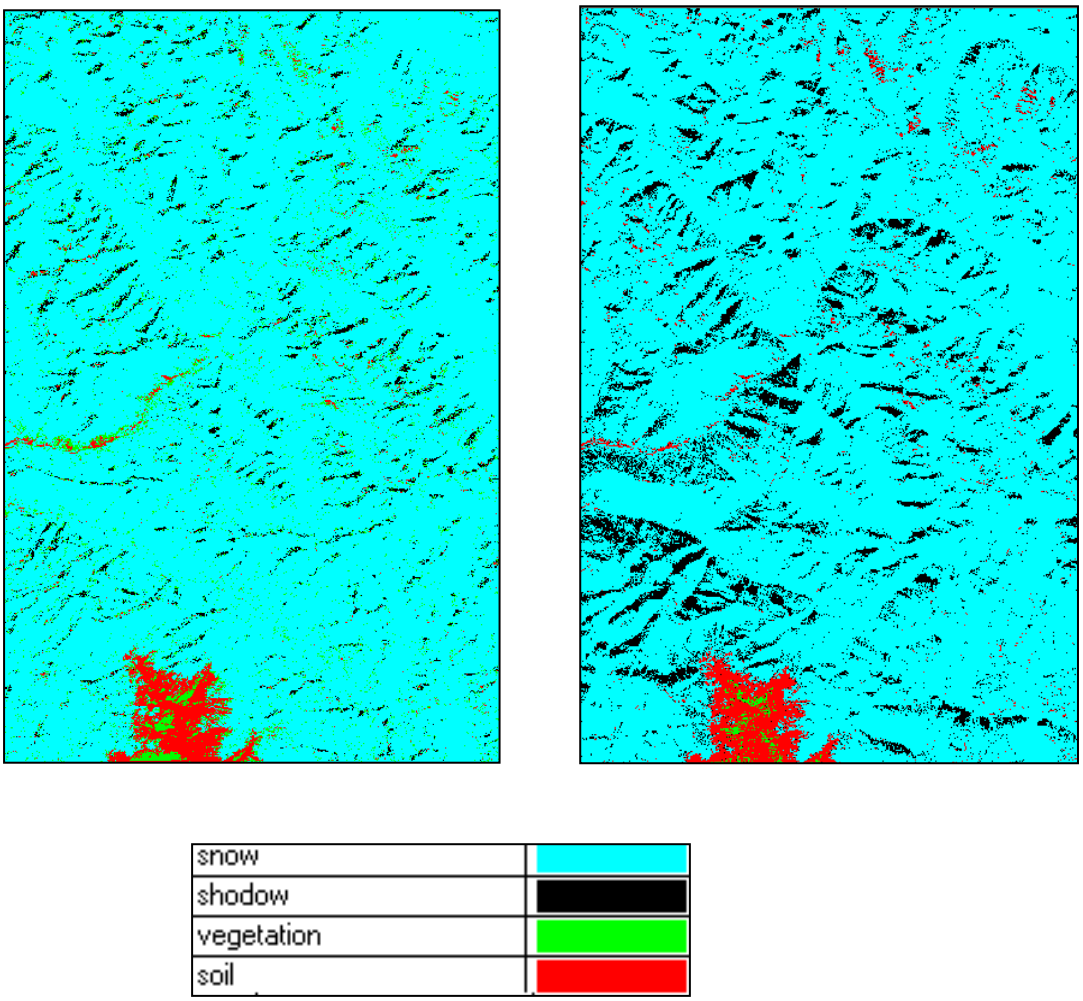

Figure 6.9 : Classification of different land covers with topographic corrections (a) 13 October 2009 using supervised classification and (b) 20 November 2009 using improved CVA.

accuracy of pre and post images before computation of error analysis for from-to change classes. It is evident from the Table 6.5(a, b) that classification accuracy of pre image increases from 94% (Kappa coefficient 0.8919) to 96% (Kappa coefficient 0.9133) after topographic corrections. The post image accuracy increases from 86% (Kappa coefficient 0.6102) to 92% (Kappa coefficient 0.7) as shown in the Table 6.6. The accuracy assessment of the from-to change classes for all kinds of change detection is shown in Table 6.7 and Table 6.8. The accuracy of 90% (Kappa coefficient 0.83) in Table 6.8 has been achieved for change discrimination with topographic models as compared to 86% (Kappa coefficient 0.7817) in Table 6.7 without topographic corrections. The accuracy of from-to change classes of improved change vector analysis are compared with conventional CVA and results are shown in the Table 6.9 (without topographic corrections) and Table 6.10 (with topographic

corrections). The conventional CVA shows an accuracy of 80% (Kappa coefficient 0.6474) and 82% (Kappa coefficient 0.6624) for topographically uncorrected and corrected data. It can be clearly inferred from the results in Tables (6.7 to 6.10) that (i) improved CVA produced best results as compared to conventional CVA and (ii) topographic corrections on satellite images significantly improve the accuracy of change classes.

CHAPTER 7

Conclusion and Future Scope

Chapter7

CONCLUSION AND FUTURE SCOPE

7.1 Salient Features of work done and conclusion

In the present thesis work we have carried out the performance analysis of various algorithms for snow cover assessment in the Western Himalayas. In this region, the snow cover distribution is very complex due to its rugged topography. Therefore, qualitative and quantitative comparative analysis of different topographic models for Himalayan terrain is carried out. The main objective of the research in this area is (i) to implement different topographic models for qualitative and quantitative assessment of snow reflectance estimation using medium resolution (AWiFS) and moderate resolution (MODIS) satellite imageries (ii) visual analysis of images after topographic corrections (iii) validation of terrain corrected satellite estimated reflectance by all these methods with field measurements (iv) examination of topographically corrected results for snow samples on the south and north aspects (v) graphical analysis after topographic corrections and (vi) to identify the most appropriate model for topographic corrections for Western Himalaya.

The important main topographic correction methods, namely C-correction, Minneart correction, the two-stage normalization and slope matching methods have been used for different solar geometry as well as different geographical regions having different terrain variability. All these methods are verified using four criteria (i) visual analysis (ii) model validation with in-situ observations (iii) reflectance of training snow samples on the south and north aspects before and after topographic corrections and (iv) graphical analysis.

Visual analysis reveals that two-stage normalization and slope matching methods are suitable for Himalayan terrain due to minimization of three dimensional relief effects. Graphical analysis of reflectance *versus* illumination (IL) satisfies the condition for all the terrain models and validates their suitability for Himalayan region. Model validation with field results and spectral reflectance of snow samples on the south and north aspects fails for all the methods except slope matching. It is, therefore, concluded that no model can be suitable for Himalayan region just satisfying only one or two of the above mentioned four criteria. Slope matching technique is the only method which satisfies all the four criteria successfully. It is found to be unique and most suitable for Himalayan terrain for qualitative

and quantitative analysis of snow cover and also for varying solar geometry using different satellites imagery of different dates. Another important conclusion drawn in this study is that snow in this region has highly non-Lambertian surface as Minneart constant is estimated to lie between zero and 0.5. The study has then been extended to include the image data obtained from MODIS sensor and similar conclusions have been drawn. It is also concluded that topographic corrections are very essential for further applications such as sub-pixel snow cover mapping, and change detection analysis, etc.

The performances analysis of various models and methods of snow cover monitoring at sub pixel level has been carried out. It has been found that MODIS sensor onboard Terra and Aqua satellites having higher temporal resolution as well as an appropriate spectral resolution, is quite suitable for snow cover analysis. However, due to its moderate resolution, MODIS data suffers from the problem of mixed pixels. In this thesis work, sub-pixel classification algorithms such as Linear Mixture Modeling (LMM), Fuzzy c-Means Clustering (FCM), have been used for the estimation of various class proportions in the moderate resolution MODIS images. Seven scenes obtained from MODIS sensor covering the Beas and Chenab basins of Himachal Pradesh (Indian Himalaya) dating between October 2008 and April 2009 were selected. The present work is confined to extraction of three main end members namely snow, vegetation and soil. It has been found that the sub-pixel snow cover can be retrieved accurately from the snow fraction images obtained from FCM clustering using diagonal and Euclidean norms.

Snow under shadow cannot be retraced with the help of sub-pixel classification techniques. NDSI image products can be used to retrace snow under shadow. However, the main limitation of the NDSI is that one need to set the threshold value properly, which again is a very critical task. Therefore, a new statistical relationship has been developed between the NDSI from MODIS data and the fraction of snow-cover at 500-meter grid resolution. It has been tested on seven selected images. Average equations of regression for snow fraction (SFRA) have been retrieved. The result shows FCM using diagonal norms are found to have highest correlation coefficient R^2 (0.8545) followed by those from FCM using Euclidean norms (0.826), LMM (0.749) and FCM using Mahalonobis norms (0.526).

The sub-pixel snow fraction (SFRA) estimated from MODIS image at 500m grid resolution using average equation on different geographical area is validated using medium resolution AWiFS satellite imagery. Total 122 MODIS pixels containing 12,200 AWiFS

pixels were verified for true snow fraction verification. Although good correlation > 0.88 was observed for all the methods but the FCM – DN and FCM – EN shows the best correlation more than 0.9. The RMSE determined using calculated and true snow faction vary from 0.097 to 0.108. The RMSE for FCM-DN (0.097) and FCM-EN (0.100) are estimated to be the lowest among all.

The effect of topographic corrections on accuracy of change detection in Himalaya terrain was studied to achieve the third objective. In the light of the drawbacks of conventional CVA, the main focus of the work here has been to analyse the effect of topography on improved CVA and its assessment vis-a-vis conventional CVA. Slope matching method for topographic corrections further improves the accuracy of change/no change area and "from-to class change. Double Window Flexible Pace Search method (DFPS) is applied to estimate of threshold of change magnitude between change/no change classes. The maximum accuracy of change/no change area is achieved 90% (Kappa coefficient 0.7811). It is found to be logical mathematical formulation as compared to conventional methods to estimate threshold. The impact of topography on land cover classification and improved change vector analysis for class changes are discussed in detail. The inclusion of topographic correction significantly improves the results and the maximum accuracy "from-to class change is 90% (Kappa coefficient 0.83). The conventional CVA does not produce very good results. It is concluded that improved CVA is very effective when implemented with proper topographic corrections in the rugged Himalayan terrain

7.2 Future Scope

In this study it has been concluded that Himalayan terrain is non-Lambertian only based on the four commonly used methods. Therefore, the analysis could be extended to other methods such as SCS (Gu, 1998), Smooth C (Raino, 2003) and SCS+C (Seonen, 2005). This conclusion may then be verified using other non-Lambertian methods such as Ekstrand-e, Ekstrand-r and Minneart-SCS. The physical modelling aspect is also required to investigated.

In this study we have utilised data from two different resolution sensors ie. AWiFS and MODIS, whatever were available in SASE archives. The conclusions drawn may also be confirmed by use of Landsat TM &MSS and SPOT as well as NOOA AVHRR sensors. The Himalayan region is frequently covered by clouds during winters and therefore imposing limitations on the use of optical sensors. AWiFS images are available at a repeat cycle of five

days and many changes may occur if one or two cycles are obscured by clouds. The effect of topography could also be evaluated both on active and passive microwave sensors which are not affected by clouds.

In the present work three end members namely, snow, vegetation and soil have been classified. This could be extended to extract more end members. The newly developed statistical relationship needs to be refined by use of more images and could also be extended to other sub-regions of Western Himalaya. The methodology for spatial location and shape of sub-pixel components also must be explored. The non-linear model for sub-pixel snow cover component needs to be explored.

CHAPTER 8

List of References

REFERENCES

Andersen T, 1982, Operational snow mapping by satellites, in Hydrological Aspects of Alpine and High Mountain Areas. *Proceedings of the Exeter Symposium*, July 1982, IAHS Publ. **138**, pp. 149-154.

Aniya M, Sato H, Naruse R, Skvarca P and Casassa G, 1996, The use of satellite and airborne imagery to inventory outlet glacier of Southern Patagonian Icefield, South America. *Photogrammetric Engineering and Remote Sensing*, **62**, pp. 1361–1369.

Anup K Prasad, Romesh P Singh, 2007, Changes in Himalayan snow and glacier cover between 1972 and 2000, EOS, *Transactions American Geophysical Union*, **88** Issue 33, pp. 325-327.

Arora M K, 1999, Thematic information extraction using neural network and fuzzy techniques. *Indian Cartographer*, **19**, pp. 344-351.

Asaoka Y, Kazama S and Sawamoto M, 2002, The variation characteristics of snow water resources in a wide area and its geographical and climatic dependency. *Journal of Japan Society of Hydrology and Water Resources*, **15**, pp. 279-289.

Bahuguna I M, Kulkarni A V, Nayak S, Rathore B P, Negi H S and Mathur P, 2007, Himalayan glacier retreat using IRS 1C PAN stereo data, *Int. J. Remote Sens*. **28(2),** pp.437–432

Barton J S, Hall D K and Riggs G A, 2001, Remote sensing of fractional snow cover using Moderate Resolution Imaging Spectroradiometer (MODIS) data. *Proceedings of the 57th Eastern Snow Conference*, May 17–19, 2000, Syracuse, NY, pp. 171– 183).

Barton N, 2002, Some new Q-value correlations to assist in site characterisation and tunnel design, *International Journal of Rock Mechanics and Mining Sciences*, **39,** pp. 185-216.

Bezdek, J. C., 1981, Pattern recognition with fuzzy objective function algorithms: *Plenum, New York*, pp. 256

Bezdek J C, R Ehrlich and W Full, 1984, FCM: The fuzzy *c*-means clustering algorithm, *Computers and Geosciences*, **10(2)** pp. 191–203.

Bhutiyani M R, 1999, Mass-balance studies on Siachen Glacier in the Nubra valley, Karakoram, Himalaya, India, *J. Glaciol*. **45(149**), pp. 112–118.

Bhutiyani M R, Kale V S and Pawar N J, 2008, Changing stream flow patterns in the rivers of northwestern Himalaya: Implications of global warming in the 20th century; *Current Science* **95(5),** pp. 618–626.

Bolsenga S J and Kistler R D, 1982, A Dual Spectroradiometer system for measuring spectral reflectance, *Journal of applied meterology*, **21**, pp. 642-647.

Bronge L B, and Bronge C, (1999), Ice and Snow type classification in Vestfold Hills , East Antarctica, using LANDSAT TM data and ground radiometer measurements, *International Journal of Remote Sensing*, **20(2),** pp. 225-240

Brun E, Martin E, Simon V, Gendre C and Coleou C, 1989, An energy and mass model of snow cover suitable for operational avalanche forecasting, *J. Glaciol*. **15 (121), pp.** 333 –341

Bruzzone L and Serpico S B, 1997, An iterative technique for the detection of land cover transitions in multi-temporal remote sensing images, *IEEE Trans. Geosci. Rem. Sens.* ,**35**, pp. 858-867.

Bruzzone L, 2000, Automatic analysis of the difference image for unsupervised change detection, *I EEE Trans on Geosci Rem. Sens*, **38(3),** pp. 1171-1181.

Buhler Y, Hueni A, Christen M, Meister M, Kellenberger T, 2009, Automated detection and mapping of rough snow surfaces including avalanche deposits using airborne optical remote sensing, *ISSW International Snow Science Workshop Davos Switzerland*, pp. 170-174.

Byrne G F, Crapper P F and Mayo K K, 1980, Monitoring land cover change by principal component analysis of multitemporal Landsat data. Remote Sensing of Enuironment, **10**, pp. 175-1 84.

Campbell J B, 1987, Introduction to Remote Sensing, Guilford Press, New York.

Campbell N, S Furby, and B Fergusson, 1994, Calibrating Images from Different Dates, CSIRO Mathematical and Information Sciences, URL: *http://www.cmis.csiro.au/rsm/research/index.htm*

Chavez P S Jr, 1988, An improved dark-object subtraction technique for atmospheric scattering correction of multispectral data, Remote Sensing of Environment, **24** pp.459-479

Chavez P S Jr, 1989, Radiometric calibration of Landsat Thematic Mapper multispectral images; *Photogramm. Eng.Remote Sens.* **55,** pp. 1285–1294.

Chavez P S Jr, 1996, Image based atmospheric corrections revisited and improved. *Photogramm. Engineering of Remote Sens.* **62** pp. 1025–1036

Chavez P S, MacKinnon D J, (1994), Automatic detection of vegetation changes in the Southwestern United States using remotely sensed images*, Photogramm. Eng. Remote Sens.* **60(5),** pp.571-583.

Chen J, Gong P, He C, Pu R and Shi P, (2003), Land-use/land-cover change detection using improved change-vector analysis, *Photogramm. Engineering and Remote Sens.* **69,** pp. 369-379

Cheng, Qi, Varshney, P. K. and Arora, M. K., 2006, Logistic Regression for Feature Selection and Soft Classification of Remote Sensing Data, *IEEE Transactions on Geosciences and Remote Sensing Letters*, **3**, 491-494

Civco D L, 1989, Topographic normalization of Landsat Thematic Mapper digital imagery; *Photogrammetric Engineering and Remote Sensing*, **55,** pp**.** 1303-1309.

Colbeck SC, 1982, An overview of seasonal snow metamorphism, Review of geophysics and Space Physics, 20 (1), pp 45-61

Colby J D, 1991, Topographic normalization in rugged terrain, *Photogrammetric engineering and Remote Sensing* **57**, pp. 531 – 537.

Colby J D, 1995, Resolution, fractal characterization and the simulated hydrologic response of a Costa Rican watershed. Unpublished PhD dissertation, Department of Geography, University of Colorado.

Colby J D and Keating P L, 1998, Land cover classification using Landsat TM imagery in the tropical highlands: the influence of anisotropic reflectance, Int. Journal of remote sensing, vol. **19(8)** pp. 1479- 1500

Collett L J, B M Goulevitch and T.J. Danaher, 1997, SLATS Radiometric Correction: A Semi-automated, Multi-stage Process for the Standardisation of Temporal and Spatial Radiometric Differences, Queensland Department of Natural Resources, URL: http://www.nrm.qld.gov.au/slats/pdf/arspc9_rad_corrections1.pdf

Colwell J E and Weber F P**,** 1981, Forest change detection, *Proceedings of the 15th International Symposium o**n** Remote Sensing of Environment held in Ann Arbor in 1981 (Ann Arbor, Michigan: Environmental Research Institute of Michigan*), pp. 839-852.

Conese C, Gilabert M A, Maselli F and Bottai L 1993, Topographic normalization of TM scenes thorough the use of an atmospheric corrections method and digital terrain models; *Photogramm. Eng. Remote Sens.* **59** pp. 745 – 1753.

Coppin P R and M E Bauer, 1996, Digital change detection in forest ecosystems with remotely sensed imagery. *Remote Sensing Reviews* **13**, pp. 207-234

Coppin PR, Lambin E, Jonckheere L, Nackaerts K and Muys B (2004) Digital change detection methods in ecosystem monitoring: a review. *Int. J. Remote Sens.* 25 pp 1565-1596.

Crane R B, 1971, Preprocessing Techniques to Reduce Atmospheric and Sensor Variability in Multispectral Scanner Data, *Proceedings of the 7th International symposium on Remote Sensing of* Environment. An Arbor, Michigan, pp. 1345.

Crane R G and Anderson M R, 1984, Satellite discrimination of snow/cloud surfaces, *International Journal of Remote Sensing*, **5(1),** 213–223.

Dale P E R, Chandica A L and Evans M, 1996, Using image subtraction and classification to evaluate change in sub-tropical intertidal wetlands. *International Journal of Remote Sensing.* **17**, pp. 703-719.

Davis R E, Nolin A W, Jordan R. Dozier J, 1993, Towards predicting temporal changes of the spectral signature of snow in visible and near-infrared wavelengths; *J. Glaciol*. **17** pp. 143–147.

Deems J S, 2001, Topographic controls on spatial and temporal variation in snow temperatures in a mountain snowpack; *Proceesing of the 69th Western Snow Conference Sun Valley ID* 131–134.

Ding Yuan, Christopher D Elvidge and Ross S Lunetta, 1998, Survey of Multispectral Methods for Land Cover Change Analysis. *Remote Sensing Change Detection Environmental Monitoring Methods and Applications* **2**, pp. 22 - 23.

Dirmhirn I and Eaton F D, 1975, Some characteristics of the albedo of the snow, Journal of applied Meteorology, **14**, pp. 375-379

Dozier J, 1984, Snow reflectance from Landsat Thematic Mapper, *IEEE Trans. Geosci. Remote Sens*., **22(3)** pp. 323–328.

Dozier J, and Marks D, 1987, Snow mapping and classification from Landsat Thematic Mapper data, *Ann. Glaciol*., **9**, pp. 97-103.

Dozier J, Devis R E, Change ATC and Brown K,1988, The spectral Bi-directional Reflectance of Snow, proceedings of the 4th International Colloquium on spectral signatures of objects in Remote Sensing Aussois, France, 18-22 January, ESA-SP-287.

Dozier J, 1989, Spectral signature of alpine snow cover from the Landsat Thematic Mapper, Remote Sensing of Environment **28**, pp 9-22.

Duguay C R, Le Drew E F, 1991, Mapping surface albedo in the East slope of the Colorado front range, U.S.A., with Landsat Thematic Mapper; *Arct. Alps. Res*. **23(2)** 213–223.

Duguay C R, Le Drew E F, 1992, Estimating surface reflectance and albedo from Landsat-5 TM over rugged terrain; *Photogramm. Eng. Remote Sens.*, **58** pp. 551–558.

Duguay C R, 1993, Modelling the radiation budget of alpine snowfields with remotely sensed data: model formulation and validation; *Ann. Glaciol*. **17,** pp. 288–293.

Ekstrand S, 1996, Landsat-TM based forest damage assessment: Correction for topographic effects, Photogramm. Eng. Remote Sens. **62** pp. 151–161.

Estes J E (editor), 1983, Manual of Remote Sensing, 2nd edition, Vol. 2 (Falls Church, VA, The Sheridan Press).

Eyton R, 1989, Loe relief topographic enhancement in a Landsat snow cover scene, *Remote Sensing of Environment*, **27**, pp.105-118.

Foody G M, Campbell N A, Trodd N M and Wood T F, 1992, Derivation and applications of probabilistic measures of class membership from the maximum-likelihood classification, *Photogrammetric Engineering and Remote Sensing*, **58**, pp. 1335 – 1341.

Foody G M, and Arora M K, 1996, Incorporating mixed pixels in training, allocation and testing stages of supervised classification, *Pattern Recognition Letters*, **17(3),** pp. 1389-1398.

Foody G.M, and Arora M K, 1997, An evaluation of some factors affecting the accuracy of classification by an artificial neural network, *International Journal of Remote Sensing*, **18**, pp. 799-810.

Foppa N, Wunderle S, Hauser A, Oesch D and Kuchen F, 2004, Operational sub-pixel snow mapping over Alps with NOAA AVHRR data. *Annals of Glaciology*, **38**, pp-245-252.

Forster B C, 1984, Derivation of atmospheric correction procedures for Landsat MSS with particular reference to urban data, *International Journal of Remote Sensing*, **5**, pp. 799–817.

Forster D, Buhler Y, Kellenberger T W, 2009, Mapping urban and peri-urban agriculture using high spatial resolution data., *Journal of Applied Remote Sensing*, **3(1),** pp 1-12

Foster J L and Chang A T C, 1993, Snow cover, in atlas of satellite observations related to global change,

Friedl MA, Brodley CE, 1997, Decision tree classification of land cover from remotely sensed data, Remote *Sensing of Environment*, **61 (3),** pp. 399-409.

Furby S L, and N A Campbell, 2000, Calibrating images from different dates to 'like-value' digital counts, *Remote Sensing of Environment*, **77**, pp. 186–196.

Furby S L, and N A Campbell, 2001, Calibrating images from different dates to 'like-value' digital counts, *Remote Sensing of Environment*, **77**, pp. 186–196.

Ghose M K, Ratika Pradhan, Sucheta Sushan Ghose, 2010, Decision Tree Classification of Remotely Sensed Satellite Data using Spectral

Separability Matrix, *International Journal of Advanced Computer Science and Applications,* **5** pp 93-101

Goetz, A. F. H., & Srivastava, V. 1985, Mineralogical mapping in the Cuprite mining district, Nevada, Proceedings of the Airborne Imaging Spectrometer Data Analysis Workshop, pp. 22−31.

Goetz A F H, 2009, Three decades of hyperspectral remote sensing of the Earth: A personal view, *Remote Sensing of Environment* **113** pp. S5–S16.

Gong P, 1993, Change detection using principal component analysis and fuzzy set theory, Canadian Journal of Remote Sensing, **19(1),** pp. 22–29.

Gong P and Xu B (2003) Remote sensing of forests over time. In: Wulder M A and Franklin SE. (eds.) *Remote Sensing of Forest Environments*: Concepts and Case Studies, Kluwer.

Gopal S and Woodcock C, 1996, Remote Sensing of forest change using artificial neural network, IEEE Transaction on Geoscience Remote Sensing, **34**, pp. 398-404.

Gratton D J, Howarth P J, and Marceau D J, 1990, Combining DEM parameters with Landsat MSS and TM imagery in a GIS for mountain glacier characterization. *IEEE Transactions on Geoscience and Remote Sensing*, **28**, pp. 766–769.

Greuell W and De Ruyter Dewildt M, 1999, Anisotropic reflection by melting glacier ice: measurements and parameterizations in Landsat TM bands 2 and 4. *Remote Sensing of Environment*, **70**, pp. 265–277.

Groisman Pavel YA , Thomas R Karl, Richard W Knight, 1994, Changes of snow cover, temperature and radiative heat balance over the Northern Hemisphere, Journal of Climate, **7,** pp. 1633-1656.

Gu D and Gillespie A, 1998, Topographic normalization of Landsat TM images of forest based on subpixel sun-canopy-sensor geometry', *Remote Sensing of Environment*, **64**,166–175.

Haertel V F, Shimabukuro Y E, 2005, Spectral linear mixing model in low spatial resolution image data; *IEEE Trans. Geosci. Remote Sensing.* **43(11)** 2555–2562.

Hall D K, Chang A T C, Siddalingaiah H, 1988, Reflectances of glaciers as calculated using Landsat-5 Thematic Mapper data; *Remote Sens. Environ*. **25,** pp. 311–321.

Hall, F.G., D.E. Strebel, J.E. Nickeson, and S.J. Goetz, 1991. Radiometric rectification – Toward a common radiometric response among multidate, multisensor images, Remote Sensing of Environment, **35**,11–27.

Hall, D F and Foster J L, (1993), "Airborne bidirectional radiances of snow-covered surface in Montana, U S A" Annals of glaciology, **17**, pp. 35-40.

Hall D K, Riggs G A and Salomonson V V, 1995, Development of methods for mapping global snow cover using Moderate Resolution Imaging Spectroradiometer Data; Remote Sens. Environ. **54,** pp. 127–140.

Hall D K, Foster J L, Verbyla D L, Klein A G and Benson C S 1998 Assessment of snow-cover mapping accuracy in a variety of vegetation-cover densities in central Alaska; *Remote Sens. Environ.* **66** 129–137.

Hame, T, Heiler I and San Miguel-Ayanz J, 1998, An unsupervised change detection and recognition system for forestry, International Journal of Remote Sensing, **19(6),** pp. 1079-1099.

Hill J and Boris S, 1991, Radiometric correction of multi-temporal Thematic Mapper data for use in agricultural land-cover classification and vegetation monitoring, *International Journal of remote Sensing,* 12, 1471-1491.

Hinkler, J. , Pedersen, S. B. , Rasch, M. and Hansen, B. U.(2002), 'Automatic snow cover monitoring at high temporal and spatial resolution, using images taken by a standard digital camera', *International Journal of Remote Sensing*, 23: 21, 4669-4682.

Hodgson M E and Shelley B M, 1994, Removing the topographic effect in remotely sensed imagery, ERDAS Monitor, **6,** pp. 4-6

Holben B and Justice C, 1980, The topographic effect on spectral response from Nadir pointing sources, Photogramm. Eng. Remote Sens. **46** pp. 1191–1200.

Hongen, Z., and L. Suhong. 2004. Moderate fraction snow mapping in Tibetan Plateau. *Proceedings of IGARSS'04 6:* 3700-3701, DOI: 10.1109/IGARSS.2004.1369923.

Howarth P and Wickwarge M, 1981, Procedure for change detection using Landsat digital data. International Journal of Remote Sensing, **2**, pp. 277-291.

Irving W H, Pollack J B, 1968, Infrared optical properties of water and ice sphere, ICARUS

Jensen J R, Narumalani S and Weatherbee O , 1993b, Measurement of Seasonal and Yearly Cattail and Waterli changes using multidate SPOT Panchromatic data, *Photogrammetric Engineering & Remote Sensing*, **59(4),** pp. 519-525.

Jensen, J. R., 1996, Introductory Digital Image Processing, A Remote Sensing Perspective, *2nd edition (Upper Saddle River, New Jersey: Prentice Hall).*

Jensen J R, 2003, Remote Sensing of the environment, *An Earth Resourse Perspective, Second Edition, Pearson Education*

Jin Chen, Peng Gong, Chunyang He, Ruiliang Pu, and Peijun Shi, 2003, Land-Use/Land-Cover Change Detection Using Improved Change-Vector Analysis, *Photogrammetric Engineering and Remote Sensing*, **69(**4), pp. 369–379.

Johnson R D and Kasischke E S, 1998, Change vector analysis: A technique for the multispectral monitoring of land cover condition, Internaltional Journal of Remote Sensing, **19(3)** pp. 411-426.

Joseph G, 2003, Fundamentals of Remote Sensing, *1st Edition, University Press* Hydeabad

Kasetkasem T., M. K. Arora, P. K. Varshney and V. Areekul, 2011, Improving Sub-pixel Classification by Incorporating Prior Information in Linear Mixture Models, *IEEE Transactions on Geoscience and Remote Sensing*, 49, 1001-1013.

Kasten F (1962) Table of solar altitudes for geographical latitudes. *CRREL Special Report* 57 (Hanover, NH, USA: US Army Corps of Engineers).

Kaufman Y J, Kleidman G R, Hall D K. Martins J V, Barton J S, 2002, Remote Sensing of sub-pixel snow cover using 0.66 and 2.1m channels, *Geophysical Research Letters*, **29**, 16: pp. 28-1-28-4.

Kawata Y, Ueno S and Ohtani A, 1995, The surface albedo retrieval of mountainous forest area from satellite MSS data, *Appl. Math. Comput*. **69,** pp 41–59.

Kazama, S. and Sawamoto, M. 1995, Estimation of snow depth distribution and water resources volume using NOAA/AVHRR. Journal of Japan Society of Hydrology and Water Resources, 8, pp. 477-483.

Keshri A K, Shukla A, Gupta R P, 2009, Aster ratio indices for supraglacial terrain mapping ,*International Journal of Remote Sensing*, **30(2),** pp. 519-524(6)

Klein A G, Hall D K and Riggs G A 1998 Improving snow cover mapping in forests through the use of a canopy reflectance model; *Hydrol. Proc.* **12** 1723–1744.

Knap W H, Reijmer C H and Oerlemans J, 1999, Narrowband to broadband conversion of Landsat T M glaciers albedos, *International Journal of Remote Sensing*, **20(10),** pp2091-2110

Konig M, Winther J G and Isaksson E, 2001, Measuring snow and glacier properties from satellite; *Rev. Geophys.* **39** 1–27.

Kristopher Kuzera, John Rogan, Ronald Eastman J., 2005, Monitoring vegetation regeneration and deforestation using Change vector analysis, *ASPRS Annual Conference Baltimore, Maryland* – March 7-11, 2005

Kuhn M, 1974, Anisotropic reflection from sastrugi fields, *Antarct. J. U.S.*, **9**, pp.123-125

Kuhn, M., 1985, Bidirectional reflectance of polar and alpine snow surfaces, *Annals of Glaciology*, **6**, pp. 164-167

Kulkarni A V, 1986, A field study of the visible and nearinfrared spectral reflectance and attenuation of solar radiation by snow, M.Sc. thesis, *Department of Geography, McGill University, Montreal, Canada*, pp. 109.

Kulkarni A V and Dhanju M S, 1987, Measurements of spectral radiance of glacier snow and ice features in Himalaya, *Technical note no. ISRO/SAC.*

Kulkarni A V, Srinivasulu J, Manjul S S, Mathur P, 2002a , Field based spectral reflectance to develop NDSI method for the snow cover; *J. Indian Soc. Remote Sens.* **30(1&2)** pp.73–80.

Kulkarni A V, Mathur P, Rathore B P, Suja Alex, Thakur N K and Kumar M, 2002b Effect of global warming on snow ablation pattern in the Himalayas; *Curr. Sci.* **83(2)** 120–123.

Kulkarni A V, Rathore B P, Mahajan S and Mathur P 2005 Alarming retreat of Parbati glacier, Beas basin, Himachal Pradesh; *Curr. Sci*. **88(11),** pp. 1844–1850.

Kulkarni, A. V., Bahuguna, I. M., Rathore, B. P., Singh, S. K., Randhawa, S. S., Sood, R. K., and Dhar, S. (2007). Glacier retreat in Himalayas using Indian Remote Sensing satellite data. *Current Science*, *92*(1), pp. 69–74.

Kumar K, Dumka R K, Miral M S, Satyal G S and Pant M 2008 Estimation of retreat rate of Gangotri glacier using rapid static and kinematic GPS survey; *Curr. Sci.* 94(2) 258–262.

Kyle H I, Curran R J, Barnes W L, and Escoe D, 1978, A cloud physics radiometer, *Third Conference on Atmospheric Radiation, American Meteorological Society*, 28-30 June 1978, Davis, Calif., pp. 107.

Law K H and Nichol J, 2004, Topographic correction for differential illumination effects on IKONOS satellite imagery; *Proceeding of XXth ISPRS symposium.*

Law K H, 2005, Correction of Terrain effects on satellite image radiance. *M.Phil* dissertation, Department of Land Surveying and Geoinformatics. *The Hong Kong Polytechnic University.*

Leroux, C., Lenoble, J., Brogniez, G., Hovenier, J.W. and DeHaan, J.F. (1999). "A model for the bidirectional polarized reflectance of snow" *Journal of quantitative spectroscopy and radiative transfer*, **61 (3),** pp. 273-285.

Leprieur C, Durand J M and Peyron J L, 1988, Influence of topography on forest reflectance using Landsat Thematic Mapper and digital terrain data; *Photogrammetry Engineering and Remote sensing.* **54,** pp .491-496

Leshkevich G A, Deering D W, ECK T F and Ahmad S P, 1990, Diurnal patterns of the bi-directional reflectance of fresh water ice, *Annals of Glaciology*, **14**, pp. 153-157

Liang S, 2004, *Quantitative Remote Sensing of Land Surfaces*, New York: John Wiley and Sons, Inc.

Li X, and Yeh AGO , 1998, Principal component analysis of stacked multi- temporal images for the monitoring of rapid urban expansion in the Pearl River Delta, *International Journal of Remote Sensing*, **19(8**), pp. 1501–1518.

Lillesand T M and Kiefer R W, 1999, *Remote Sensing and image Interpretation, New York*, John Wiley & Sons, Inc.

Lu D , Mausel P, Brondizio E and Moran E (2004) Change detection techniques. *Int. J. Remote Sens.* 25(12) pp 2365-2407.

Malila W (1980) Change vector analysis : an approach for detecting forest changes with Landsat. *Proceeding of the 6th Annual Symposium on Machine Processing of Remotely Sensed Data*. West Lafayette IN 3-76 June 1980 (West Lafayette, IN Purdue University Press) pp 326-335

Markham B L and Barker J L, 1986, Landsat MSS and TM post caliberation Dynamic ranges exoatmospheric reflectances and at-satellite temperature, *EOSAT Technical Notes*, **1**, pp. 3-8.

Markham B L and BarkerJ L, 1987, Thematic Mapper band pass solar exoatmospheric irradiances, *International Journal of Remote Sensing* **8(3)** pp. 517-523

Mas J F, 1999, Monitoring land-cover changes: a comparison of change detection techniques, *International Journal of remote sensing*, **(20,1)** pp.139- 152.

Matson M, Roeplewski C F and Varnadore M S, 1986, An Atlas of Satellite erived Northern Hemisphere Snoe Cover Frequency. *National Weather Service, Washington DC*, 75.

Matson M, 1991, NOAA satellite snow cover data, *Palaeogeog. And Paleoecol*, **90**, pp. 213-218.

McCluney W R ,1994, Introduction to Radiometery and Photometery, *Artech House Inc.,Norwood,* MA,USA

Merril K R and Jiajun L, 1998, A comparison of four algorithms for change detection in an urban environment, Remote sensing of Environment, **63**, pp. 95-100.

Meyer P, Itten K I, Kellenbenberger, Sandmeier S and Sandmeier R, 1993, Radiometric corrections of topographically induced effects on Landsat TM data in an alpine environment, ISPRS *Journal of Photogrammetry and Remote Sensing,* **48**, pp. 17-28.

Michalek J L, Wagner T W, Luczkovich J J and Stoffle R W (1993) Multispectral change vector analysis for monitoring coastal marine environments. Photogramm. Eng. Remote Sens. 59 pp.381-384.

Min Xu, P. Watanachaturaporn, P. K. Varshney and M. K. Arora, 2005, Decision Tree Regression for Soft Classification of Remote Sensing Data, *Remote Sensing of Environment*, 97, 322-336.

Milton, E.J., 1994. Teaching atmospheric correction using a spreadsheet, Photogrammetric Engineering & Remote Sensing, **60(6**), 751–754

Minneart M, 1941, The reciprocity principle in lunar photometry; *Astrophysics Journal* **93** 403-410.

Mishchenko M I, Dlugach J M, Yanovitskij E G, Zakharova N T, 1999, Bidirectional reflectance of flat, optically thick particulate layers: an efficient radiative transfer solution and applications to snow and soil surfaces, J Quant. Spec. Rad. Trans., 63, pp 409-432

Mishra V D, Negi H S, Rawat A K, Chaturvedi A, Singh R P, 2009a, Retreival of sub-pixel snow cover information in the Himalayan region using medium and coarse resolution remote sensing data; *International Journal of Remote Sensing*, **30,** pp. 3407-4731.

Mishra V D, Sharma J K, Singh K K , Thakur N K, Kumar M, 2009b, Assessment of different topographic corrections in AWiFS satellite imagery of Himalaya terrain, 2009, J Earth Syst. Sci. **118** (1) pp. 11-26.

Mishra V D, Sharma J K, Khanna R, "Review of topographic analysis methods for the western Himalaya using AWiFS and MODIS satellite imagery" *Annals of Glaciology*, Volume 51, Number **54**, May 2010 , pp. 153-160

Moran M S, Jackson D, Slate P N and Teillet P M, 1992, Evaluation of simplified procedure for retrieval of land surface factors from satellite sensor output, Remote Sensing of Environment, **41**, pp. 169-184

Motoya K ,2003, Spectral characteristic based vegetation and snow indices on various surfaces in the Airborne Multispectral Scanner (AMSS) two altitude observations in 2001, Journal of Japan Society of Hydrology and Water Resources, 16, pp. 408-419

Mukkoth V N, 2004, Snow melt runoff modelling using MODIS in Elaho River Basin, British Columbia; *Environmental Information Archives* **2** pp**.** 526–530.

Nainwal H C, Negi B D S, Chaudhary M, Sajwan K S and Gaurav A, 2008, Temporal changes in rate of recession: Evidences from Satopanth and Bhagirath Kharak glaciers, Uttarakhand, using Total Station Survey; *Curr. Sci.* **94(5**) 653–660

Navalgund R R, Jayaraman V and Roy P S, 2007, Remote sensing applications: an overview, Current Science, 93(12), pp 1747-1766

Negi H S, Mishra V D and Mathur P, 2005, Change Detection Study for Snow Cover Mountains using Remote Sensing and Ground based Measurements, *Journal of Indian Society of Remote Sensing*, **33(2),** pp. 245-251

Nelson R F, 1983, Detecting forest canopy change due to insect activity using Landsat MSS. Photogrammetric Engineering and Remote Sensing, **49**, 1303-1 3 14

Nichol J, Hang L K and Sing W M, 2006, Empirical correction of low sun angle images in steeply sloping terrain : a slope matching technique; *Int. J. Remote Sens*. **27(3-4)** pp 629-635.

Nolin A W, Dozier J and Mertes L A K, 1993, Mapping alpine snowcover using a spectral mixture modelling technique, *Annals of Glaciology*, **17**, pp. 121 – 124.

Nolin, A.W. and Dozier, J. (1993). "Estimating snow grain-size using AVIRIS data" Remote sensing of environment, **44 (2-3),** pp. 231-238.

Nolin A W and Liang S, 2000, Progress in bi-directional reflectance modelling and applications for surface particulate media: snow and soils, Remote Sens. Rev. **18**, pp 307-342

O'Brian H W, Munis H, 1975, Red and NIR spectral reflectance of snow, USA CRREL Research report, **332**, 18p

Ouaidrari H, Vermote E, 1999, Operational atmospheric correction of Landsat TM data. *Remote Sensing of Environment*, **70**, pp. 4-15.

Painter T H, Roberts D A, Green O R and Dozier J, 1998. The effect of grain size on spectral mixture modelling of snow-covered area from AVIRIS data. *Remote Sensing of Environment*, **65**, pp. 320-332.

Painter T H, Dozier J, Roberts D A, Davi R F and GreenR O, 2003. Retrieval of sub-pixel snow covered area and grain size from imaging spectrometer data, *Remote Sensing of Environment*, **85**, pp. 64-77

Palluconi F, Hoover C, Alley R, Jentoft-Nilsen M and Thompson T, 1996, "An atmospheric correction method for ASTER thermal radiometry over land", *ASTER Standard Data Product*, AST09.

Pandya M R, Singh R P, Murali K R, Babu P N, Kirankumar A S and Dadhwal V K, (2002), Bandpass solar exoatmospheric irradiance and Rayleigh optical thickness of sensors on board Indian remote sensing satellites-1B, -1C, -1D, and P4, *IEEE Trans. Geosci. Remote Sens*., **40(3),** pp.714–718.

Peter Romanov, Garik Gutman, Ivan Csiszar, 2000, Automated Monitoring of Snow Cover over North America with Multispectral atellite Data, *Journal of Applied Meterology American Meteorological Society* **39,** pp. 1866-1880.

Pouch G W and Campagna D (1990) Hyperspherical direction cosine transformation for separation of spectral and illumination information in digital scanner data. *Photogramm. Engineering and Remote Sens*. **56**, pp 475-479

Price K P, Pyke D A and Mendes L, 1992, Shrub Dieback in a Semiarid Ecosystem: The integration of Remote Sensing and GIS for detection vegetation change, *Photogrammetric Engineering &Remote Sensing*, **58(4),** pp. 455-463

Ramamoorthi A S , Haefner H ,1991, Runoff modelling and forecasting of river basins, and Himalayan snow cover information system, *Proceedings of the Vienna Symposium*, **201**, pp. 347-355.

Rencz A N and Ryerson R A,1999, Manual of Remote Sensing- Remote Sensing for Earth Science, 3 rd Edition, John Wiley & Sons Inc.

Riano D, Chuvieco E, Salas J and Aguado I 2003 Assessment of different topographic corrections in Landsat-TM data for mapping vegetation types; *IEEE Trans. Geosci. Remote Sens*. **41(5),** pp. 1056–1061.

Richter R, 1985, Some aspects of the atmospheric radiance model of LOWTRAN6, *International Journal of Remote Sensing*, **6**, pp. 1773-1777.

Ritcher R, 2004, Atmospheric / Topographic corrections for Satellite Imagery (ATCOR-2/3) User Guide, Ver. 6.0 DLR *German Aerospace Center*, Germany

Rittger, K., Painter, T. H., & Dozier, J. (2012). Assessment of methods for mapping snow cover from MODIS. Advances in Water Resources. http://dx.doi.org/10.1016/ j.advwatres.2012.03.002.

Robinson D A and Kukla G, 1985, Maximum surface albedo of seasonally snow covered lands in the northern Hemisphere; *J. Climate and Applied Meteorology*, **24,** pp**.** 402–411.

Romanov P, Gutman G and Csiszar I, 2000, Automated monitoring of snow cover over North America with multispectral satellite data. *Journal of Applied Meteorology* **39**, pp. 1866–1880.

Romanov P, Tarpley D, Gutman G and Carroll, 2003, Mapping and monitoring snow-cover fraction over North America; *J. Geophys. Res*. **108,** 8619.

Romanov P and Tarpley D, 2004, Automated monitoring of snow cover over South America using GOES imager data, *International Journal of Remote Sensing*, **24(5),** pp. 1119-1125

Rosenthal W and Dozier J, 1996, Automated mapping of montane snow cover at subpixel resolution from the Landsat Thematic Mapper, *Water resources Research*, **322**, pp. 115-130.

Russell P B, Livingston J M, Dutton E G, Pueschel R F, Reagan J A, Defoor T E, Box M A, Allen D, Pilewskie P, Herman B M, Kinne S A and Hoffman D J, 1993,
Pinatubo and pre-Pinatubo optical depth spectra: Mauna Loa measurements, compositions, inferred particle distribution, radiative effects, and relationship to Lidar data. *Journal of Geophysical Research* 98 pp 22969–22985

Saito A, Yamazaki T, 1999, Characteristics of spectral reflectance for vegetation ground surfaces will snowcover: Vegetation indices and snow indices; *J. Japan Soc. Hydrol. Water Res.* **12** pp. 28–38.

Salomonson V V and Appel I , 2004, Estimating fractional snow cover from MODIS using the normalized difference snow index, *Remote Sensing of Environment*, **89**, pp. 351 – 360.

Salomonson V V and Appel I , 2006, Development of the Aqu MODIS NDSI fractional snow algorithms and validation results, *IEEE Transactions On Geoscience and Remote Sensing*, **44(7),** pp. 1747-1756.

Salomonson V V and Marlatt D C, 1968, Anistropic solar reflectance over white sand, snow and stratus clouds, J Applied Meteorology, **7**, pp 475-483

Sandmeier S, Sandmeier W, Itten K I, Schaepman M E, and Kellenberger TW, 1995, The Swiss field-goniometer system. *Proceedings of IGARSS '95, IEEE International Geoscience and Remote Sensing Symposium* (July), pp. 2078–2080.

Schott J R, C Salvaggio and W J Volchok, 1988, Radiometric scene normalization using pseudoinvariant features, *Remote Sensing of Environment*, **26**, 1–16.

Sharma S S, Ganju 2000, Complexities of avalanche forecasting in Western Himalaya-an overview, Cold Regions Science and Technology 31 (2000), pp. 95-102

Shimamura Y, Izumi T and Matsuyama H, 2006, Evaluation of useful method to identify snow covered areas under vegetation – comparisons among a newly proposed snow index, normalized difference snow index, and visible reflectance, *International Journal of remote Sensing*, **27**, pp. 4867 – 4884.

Simpson J J, McIntire T J, 2001, A recurrent neural network classifier for improved retrievals of areal extent of snow cover. IEEE *Transactions on Geoscience and Remote Sensing*, **39,** pp.2135- 2147

Singh A, 1986, Change detection in the tropical forest environment of northeastern India using Landsat. *Remote Sensing and Tropical Land Management*, edited by M. J. Eden and J. T. Parry (London: John Wiley & Sons), pp. 237-254.

Singh A, 1989, Digital change detection techniques using remotely – sensed data, *International Journal of Remote Sensing*, **10(6),** pp. 989-1003.

Singh P, Kumar N and Arora M, 2000, Degree day factors for snow and ice for Dokriani Glacier Garhwal Himalayas, *J. Hydrol.* **235(1–2)** pp. 1–11.

Simpson J J, and McIntire T J, 2001, A recurrent neural network classifier for improved retrievals of areal extent of snow cover. IEEE Transactions on Geoscience and Remote Sensing, **39(10),** pp. 2135-2147.

Sirguey, P., Mathieu, R., Arnaud, Y., 2009. Subpixel monitoring of the seasonal snow cover with MODIS at 250 m spatial resolution in the Southern Alps of New Zealand: Methodology and accuracy assessment. *Remote Sensing of Environment*, **113**, pp. 160-181.

Smith J A, Lin T L and Ranson K J, 1980, The Lambertian Assumption and Landsat Data; *Photogrammetric Engineering and Remote Sensing*, **46 (9),** pp.1183-1189.

Soenen S A, Peddle D R and Coburn C A, 2005, SCS + C: a modified sun-canopy-sensortopographic correction in forested terrain, *IEEE Transactions on Geoscience and Remote Sensing*, **43**, 2148–2159.

Solberg R, 2000, A new method for sub-pixel snow-cover mapping using hyperspectral imagery– first results. *Proceedings of EARSeL-SIG-Workshop Land Ice and Snow, Dresden, Germany*, June 16–17, 2000.

Song J, Gao W, 1999, An improved method to derive surface albedo from narrowband AVHRR satellite data: narrowband to broadband conversion; *J. Applied Meteorology*. **38** pp. 239–249.

Song C, Woodcock C E, Seto K C, Lenney M P and Macomber S A, 2001, Classification and change detection using Landsat TM data: when and how to correct atmospheric effects, *Remote Sens. Environment*, **75(2)**, pp. 230–244.

Srinivasulu J and Kulkarni A V, 2004, Estimation of spectral reflectance of snow from IRS 1D LISS-III sensor over the Himalayan terrain, *Proc. Indian Acad. Of Sci. (Earth Planet Sci.)* **113(1),** pp. 117-128.

Steffen K, 1987, Bidirectional reflectance of snow: Large scale effects of seasonal snow cover, *Proceedings of the IAHS Symposium* held in Vancouver on 19-22 August 1987, pp 415-425

Steffen K, 1996, Effect of solar zenith angle on snow anisotropic reflectance, *In IRS 96, Current Problems in Atmospheric radiation*, pp. 41-44

Tanre D, Deroo C, Duhalt P, Herman M, Morcreote J J, Perbos J and Deschomps PY, 1990, Technical note: description of a computer code to simulate the satellite signal in the solar spectrum: the 5S code. *Canadian Journal of Remote Sensing*, **8**, 84-106.

Tanré D, Kaufman Y J, Herman M and Mattoo S, 1997, Remote sensing of aerosol properties over oceans using the MODIS/EOS spectral radiances. *J. Geophys. Res*., **102(**D14**),** 16971-16988.

Teillet P M, Guindon B and Goodenough D G, 1982, On the slope aspect correction of multispectral scanner data; *Canadian J. Remote Sensing*, **8,** pp 84-106.
Teillet, P.M., 1986, Image correction for radiometric effects in remote sensing, *International Journal of Remote Sensing*, **7**, pp. 1637–1651.

Thome K, Markham B. Barker J, Slater P and Biggar S, 1997, Radiometric calibration of Landsat, *Photogrammetric Engineering and Remote Sensing*, **63**, pp. 835-858.

Tiwari R S , Arora M K. and Kailash T., 1999, Soft classification for sub-pixel land cover extraction, *Journal of Indian Society of Remote Sensing*, **27(4),** pp. 225-234.

Tokola T, Sarkeala J and Vander Linden M, 2001, Use of topographic correction in Landsat TM-based forest interpretation in Nepal; *International Journal of Remote Sensing*. **22, pp.** 551-563.

Treichler D S, Bühler Y, Hueni A, Kneubühler M, Itten K I, 2009. Spectral discrimination of avalanche deposits, *6th EARSeL Imaging Spectroscopy SIG workshop: proceedings , Tel Aviv, Israel*.

Upadhyay D S, 1995, Snow melt processes; *Cold Climate Hydrometeorology*. New Age Int. Pvt. Ltd. Publ., pp 213–230.

Valovcirn F R, 1976, Snow cloud discrimination, AFGL-TR-76- 0174, ADA 032385. Air Force Geophysics Laboratory Hanscom, Massachusetts, 16

Valovcin F R, 1978, Spectral radiance of snow and clouds in the near infrared spectral region, AFGL-TR-78-0289, ADA 063761. Air Force Geophysics Laboratory Hanscom, Massachusetts

Van Der Meer F, 1996, Spectral mixture modeling and spectral stratigraphy in carbonate lithofacies mapping. *ISPRS Journal of Photogramm. and Remote Sens.* **51** pp 150–162

Vermote, E. F., D. Tanre, J. L. Deuze, M. Herman, and J. J. Morcrette, 1997, Second simulation of the satellite signal in the solar spectrum: An overview, IEEE Trans.Geosci. RemoteSensing

Vikhamar D, Solberg R, 2002, Subpixel mapping of snow cover in forests by optical remote sensing, *Remote Sensing of Environment*, **84**, pp. 69 – 82.

Vikhamar D, Solberg R, 2003, Snow cover mapping in forests by constrained linear spectral unmixing of MODIS data, *Remote Sensing of Environment*, **88**, pp. 309-323.

Wang F, 1990, Improving remote sensing image analysis through fuzzy information representation, *Photogrammetric Engineering and Remote Sensing*, **56**, pp. 1163 – 1168.

Wang J, 1993, LINDA- a system for automated linear feature detection and analysis. *Canadian Journal of Remote Sensing*, **19**, pp. 9–21.

Wang J and W Li, 2003, Comparison of methods of snow cover mapping by analyzing the solar spectrum of satellite remote sensing data in China. *International Journal of Remote Sensing*, **24(21),** pp. 4129-4136.

Warren S G, 1982, Optical properties of Snow, *Review of Geophysics and Space Physics*, **20(1),** pp 67-89.

Warren S G, Brandt R E and Hinton P O, 1998, Effect of surface roughness on bidirectional reflectance of Antarctic snow. *Journal of geophysical research-Planets*, **103 (E11),** 25789-25807.

Warner T, (2005), Hyperspherical direction cosine change vector analysis. *Int. J. Remote Sens.* **26(6)** pp. 1201-1215

Weismiller A, Kristofs J, Scholzd K, Anutap E, and Momens A, 1977, Change detection in coastal zone environments, Photogrammetric Engineering and Remote Sensing, **43**, pp.1533-1539.

Winther J G, 1992, Landsat Thematic Mapper ((TM)) derived reflectance from a mountainous watershed during the snow melt season, Nord. Hydro, **23** pp. 273-290

Winther J G, 1993, Landsat TM derived and in-situ summer reflectance of glaciers in Svalbard, *Polar Research*, **12(1)** pp**.** 37–55.

Winther J G, 1994, Spectral bi-directional reflectance of snow and glacier ice measured in Dronning Maud Land, Antartica, *Ann. of glacial*, **20**, pp. 1-5

Winther J G, Gerland S, Orbaek J B, Ivanov B, Blanco A and Boike J, 1999, Spectral reflectance of melting snow in a high Arctic watershed on Svalbard: some implications for optical satellite remote sensing studies, *Hydrological processes*, **13 (12-13),** pp. 2033-2049.

Wiscomb W J, Warren S G,1980, A model for the spectral albedo of snow, II, snow containing atmospheric aerosols, Journal of Atmospheric Science, 37 (12) pp. 2734-2745

Wulder M A and Franklin S E, 2003, Remote sensing of forest environments : Concepts and Case Studies. *Kluwer Academic Publishers*. Norwell, Massachusetts

Xiao X, Shen Z and Qin X 2001 Assessing the potential of VEGETATION sensor data for mapping snow and ice cover: A normalized difference snow and ice index; *Int. J. Remote Sens.* **22** 2479–2487.

Xin Li, Koike, Toshio, Guodong, Cheng, 2002, Retrieval of snow reflectance from Landsat data in rugged terrain; *Annals of Glaciology*, **34**, pp. 31-37.

Yang X.J and C P Lo, 2000. Relative radiometric normalization performance for change detection from multi-date satellite images, *Photogrammetric Engineering & Remote Sensing*, **66(8) ,** pp**.** 967–980.

Yuan D and C D Elvidge, 1996, Comparison of relative radiometric normalization techniques, *ISPRS Journal of Photogrammetry and Remote Sensing*, **51**, pp. 117–126.

Appendix 'A'

ABOUT THE AUTHOR

Jagjit Kumar Sharma was born on 15 September 1947 in a village in Ropar (Punjab). He had joined the Corps of Electronics and Mechanical Engineering (Army) in 1972 as commissioned officer. He received his engineering degree from MCEME, Secunderabad in 1977. Later he did M-Tech in 'Microwaves and Optical Communication Engineering' from IIT Kharagpur in 1982.

He was deputed to Defence Electronics Application Laboratory, Dehradun (DRDO) in 1997, where he specialised in the area of Remote Sensing and Satellite Imaging. He had executed two projects of national importance on 'Real Time Acquisition and Dissemination of Satellite Imagery'. He was awarded DRDO Technology Day Commendation for the development of Change Detection Software in 2003.

He has been Professor and Head ECE Department in Rayat Institute of Engineering and Technology for 5 years and is currently principal Rayat Polytechnic College. He is Fellow of IETE, Member of Indian Society of Remote Sensing and Life member of Indian Society of Remote Sensing. He has contributed more than twenty research publications in various Journals and Conferences.

Communication Address

J K Sharma
House No 138
Sector 4
Panchkula
Haryana - 134112